LBNL-43186

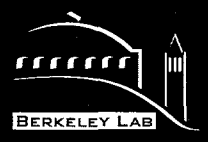

ERNEST ORLANDO LAWRENCE
BERKELEY NATIONAL LABORATORY

Ultrafast Dynamics of Electrons at Interfaces

Jason D. McNeill

Chemical Sciences Division

May 1999

Ph.D. Thesis

LBNL-43186

Ultrafast Dynamics of Electrons at Interfaces

by

Jason Douglas McNeill
Ph.D. Thesis

Department of Chemistry
University of California, Berkeley

and

Chemical Sciences Division
Lawrence Berkeley National Laboratory
University of California
Berkeley, California 94720

May 1999

This work was supported by the Director, Office of Energy Research, Office of Basic Energy Sciences, Chemical Sciences Division, of the U.S. Department of Energy under Contract No. DE-AC03-76SF00098.

Ultrafast Dynamics of Electrons at Interfaces

by

Jason Douglas McNeill

Abstract

Ultrafast Dynamics of Electrons at Interfaces

by

Jason Douglas McNeill

Doctor of Philosophy in Chemistry

University of California at Berkeley

Professor Charles B. Harris, Chair

Electronic states of a thin layer of material on a surface possess unique physical and chemical properties. Some of these properties arise from the reduced dimensionality of the thin layer with respect to the bulk or the properties of the electric field where two materials of differing dielectric constants meet at an interface. Other properties are related to the nature of the surface chemical bond. Here, the properties of excess electrons in thin layers of Xenon, Krypton, and alkali metals are investigated, and the bound state energies and effective masses of the excess electrons are determined using two-photon photoemission. For Xenon, the dependence of bound state energy, effective mass, and lifetime on layer thickness from one to nine layers is examined. Not all quantities were measured at each coverage.

The two photon photoemission spectra of thin layers of Xenon on a Ag(111) substrate exhibit a number of sharp, well-defined peaks. The binding energy of the excess electronic states of Xenon layers exhibited a pronounced dependence on coverage. A discrete energy shift was observed for each additional atomic layer. At low coverage, a series of states resembling a Rydberg series is observed. This series is similar to the image state series observed on clean metal surfaces. Deviations from image state energies can be described in terms of the dielectric constant of the overlayer material and its effect on the image potential.

For thicker layers of Xe (beyond the first few atomic layers), the coverage dependence of the features begins to resemble that of quantum well states. Quantum

well states are related to bulk band states. However, the finite thickness of the layer restricts the perpendicular wavevector to a discrete set of values. Therefore, the spectrum of quantum well states contains a series of peaks which correspond to the various allowed values of the perpendicular wavevector. Analysis of the quantum well spectrum yields electronic band structure information. In this case, the quantum well states examined are derived from the Xenon conduction band. Measurements of the energies as a function of coverage yield the dispersion along the axis perpendicular to the surface while angle-resolved two-photon photoemission measurements yield information about dispersion along the surface parallel.

The relative importance of the image potential and the overlayer band structure also depends on the quantum number and energy of the state. Some members of the image series may have an energy which is in an energy gap of the layer material, therefore such states may tend to remain physically outside the layer and retain much of their image character even at higher coverages. This is the case for the $n = 1$ image state of the Xe/Ag(111) system. The energies of image states which are excluded from the layer have a complex dependence on the thickness of the layer and its dielectric constant.

The population decay kinetics of excited electronic states of the layer were also determined. Lifetimes are reported for the first three excited states for 1–6 atomic layers of Xe on Ag(111). As the image states evolve into quantum well states with increasing coverage, the lifetimes undergo an oscillation which marks a change in the spatial extent of the state. For example, the $n = 2$ quantum well state decreases substantially at 3–5 layers as the electron probability density in the layer increases. The lifetime data are modeled by extending the two-band nearly-free-electron approximation to account for the insulating Xe layer.

To my dear wife, Carolina, our wonderful son, Andrés, and Mom and Dad

Contents

List of Figures

List of Tables

Acknowledgements

Several people have contributed immensely to the work described in this thesis. Professor Charles B. Harris helped lead me towards interesting problems and provided an environment where I felt free to follow my scientific instincts. Chung Wong, Nien-Hui Ge, and Robert Lingle worked with me over the course of several years to add femtosecond time resolution to the experiment and apply the technique to several adsorbate systems. Chung has been a good listener and source of good ideas in many, many discussions, and is a good friend. Robert Jordan taught me almost everything I needed to know in order to perform two-photon photoemission experiments and he introduced me to the arcane arts of laser alignment and vacuum technology. Walter Merry designed and constructed the vacuum chamber used in these experiments. Without his detailed drawings and diagrams it would have been difficult to modify and maintain the experiment. Kelly Gaffney has shared many good ideas and provided valuable input.

I have also had the opportunity to interact with and enjoy the company of other members of the Harris research group. Haw Yang provided valuable perspective and comments. Matt Asplund and Steve Bromberg provided useful insights and were helpful in taking charge of improving shared resources and group infrastructure. Other members are actively and enthusiastically pursuing questions which were raised by this work. Vijaya Narasimhan has been helpful in putting all the pieces together to solve a problem or fill a research need. There are many other people who have touched my life or helped me during my time at Berkeley and I would like to take the opportunity to thank them all.

I would also like to thank my family for their support throughout my graduate career. My parents Kent and Sarah have always encouraged me in all my pursuits and have always been loving and supporting. I have always valued my close relationship with my brother, John. I especially would like to thank my wife Carolina and our son Andrés for their love, support, and patience.

This work was supported by the Director, Office of Energy Research, Office of Basic Energy Sciences, Chemical Sciences Division of the U.S. Department of Energy,

under Contract No. DE-AC03-76SF00098. I would also like to acknowledge National Science Foundation support for specialized equipment used in some experiments.

Chapter 1

Introduction

The interactions of electrons with interfaces are of considerable importance in many fields of study. The energy levels, dynamical processes, and transport properties of electrons at surfaces and interfaces have a direct influence on the surface chemistry, electrochemistry, electronic device properties, and optical properties of interfaces. The unique electronic properties of the surface are involved in the surface chemical bond. The breaking of a surface chemical bond and the generation of reactive species at the surface may in some cases involve electron transfer from the substrate to the adsorbate. The field of surface science is largely concerned with the interaction of electrons at surfaces and interfaces. Most of the tools of surface spectroscopy, for example, electron energy loss, Auger emission, and photoemission, involve the interactions of electrons with the surface. The scanning tunneling microscope and the atomic force microscope, which have increased our knowledge of surfaces immensely in recent years, involve electronic interactions between the surface and the probe tip.

The present work is concerned with electronic states which are present at a surface or interface. Of primary interest is the class of states whose spatial extent is largely coincident with that of the adsorbate layer, here referred to as the interfacial quantum well states. The primary system of interest in the present work consists of a metal substrate covered with a thin layer of electrically insulating material. In addition, thin metal layers on a metal substrate have been investigated. The be-

havior of electrons at the metal/insulator interface have been investigated for *films* ranging in thickness from one to several molecular layers. The chief aim has been to develop a more complete picture of electronic structure at interfaces. A central question which has emerged concerns the roles the molecular properties (through the quantum mechanical energy levels of the isolated adsorbate molecule and molecular polarizabilities), bulk electrical properties (energy bands, dielectric constants), and surface or interface properties play in determining the electronic structure of the composite interface. One strategy has been to build up a microscopic understanding of electronic structure of an interface by comparing measurements of electronic structure over a wide range of layer thicknesses. Presumably, effects which involve electronic interactions between the substrate material and the first molecular layer of adsorbate should be more prominent for very thin layers than for very thick layers. Similarly, bulk properties should be manifested as the layer thickness increases beyond that of a single molecular layer.

Another question which emerged during the course of these investigations concerns the spatial extent of interfacial electronic bands. Factors which are likely to influence the spatial extent of the interface bands include the nature of the electronic potential in the region near the junction between the two materials and the bulk and molecular electronic properties of the two materials comprising the interface. Yet another important question concerns the nature and associated time scales of the relaxation processes of interfacial electronic bands. Many scientifically important systems are in a metastable state in which physical interactions between parts of the system result in a loss of energy to the surroundings. Information about the dynamics of electrons at interfaces is of value because it offers a window into range of processes through which an electron can transfer energy, change quantum number, and change position. Given sufficient experimental evidence, a complete picture of the various processes, intermediates, timescales, and likely sequences of events involving electrons at interfaces can be obtained. The kind of experimental evidence required to develop such a picture is time-resolved spectroscopic characterization of the quantum-mechanical energy levels of electrons at interfaces. The characteristic time scale of a given physical process is often roughly dependent on the size of the

system. The slow dance of the planets is measured in days, years, and centuries. In contrast, the characteristic time scale of electronic interactions in atoms and small molecules is generally between a few femtoseconds and hundreds of picoseconds.

The experimental technique employed for these studies is time-resolved two-photon photoemission. Time-resolved two-photon photoemission is a relatively new technique, and its application to the study of complex interfaces is even more recent. This technique is uniquely suited to the study of the electronic structure of interfaces. The advantages include good energy resolution (comparable or better than that of other electron spectroscopies), ultrafast (femtosecond or 1×10^{-15} s) time resolution, and access to the energy window of primary importance to the chemical and electrical properties of interfaces. In the language of solid state physics, the energy range of two photon photoemission is the region containing the valence and conduction bands, the region most important to the the electrical properties of materials. In the language of chemistry, it is the energy region containing the HOMO (highest occupied molecular orbital) and LUMO (lowest unoccupied molecular orbital), the region generally associated with absorption in the ultraviolet and visible regions of the electromagnetic spectrum, bond formation, bond cleavage and electron transfer. The technique is also quite simple and elegant, conceptually. A photon from a laser pulse strikes a surface, imparting its energy to an electron, which is elevated to an excited energy level of the interface. Some time later, a photon from a second laser pulse strikes the surface, imparting enough energy to detach the electron from the surface. The free electron then travels a fixed distance in vacuum before striking a detector which records its energy and the direction of emission. The population of a given electronic energy level at a given time can be determined by setting the time delay between laser pulses.

The present work involved a combination of several experimental techniques and the development of several theoretical models for excited interfacial states. The experiments included standard surface preparation and characterization techniques of surface science, ultrafast laser spectroscopy, and photoelectron spectroscopy. Surfaces and interfaces are by their nature fragile, difficult to prepare, and prone to contamination. In addition, the data obtained by some of the experimental techniques

is often difficult to analyze, somewhat ambiguous and prone to misinterpretation. Every attempt was made to ensure that the substrate and overlayers were relatively clean, well-ordered, and free of contamination in an ultra high vacuum environment. Spectra were obtained in a thorough and systematic fashion. Multiple experimental runs were used to verify the reproducibility of results. Significant efforts were made to calibrate and verify the functioning of the TPPE spectrometer. Efforts were also made to ensure that the model for excited interfacial states were derived from simple models which have proven successful in similar systems.

Chapter 2

Background

2.1 History of Surface States

The study of the interaction of light with electrons at surfaces dates to the work of a German experimenter, Philip Lenard, who studied the absorption of visible and ultraviolet light by metals. He found that enough light energy is transferred to the electrons in the metal so that some of them are ejected from the metal surface. He also found that the energy of the ejected electrons did not increase with light intensity, as predicted by classical theory. Rather, the energy of the electrons depended on the wavelength of light while the current depended on the intensity. This work led Einstein to develop his theory of the photoelectric effect, an important confirmation of the quantum hypothesis [1, 2].

A more detailed understanding of the electronic structure of metals was obtained by the application of quantum mechanics to the electronic energy levels of solids. In the theory of the electronic structure of metals as first developed it is assumed that electrons move about freely in a constant potential throughout the interior of the crystal. A better approximation is to consider the potential inside the crystal to be periodic with the periodicity of the lattice. The principal effect of the periodic potential is the presence of band gaps when the electron momentum is close to that of a multiple of a reciprocal lattice vector, where it can be said that the electron is Bragg-reflected by the periodic potential [3].

Early theories which included lattice periodicity assumed infinite periodic crystals. An infinite crystal possesses an infinite number of states. For a finite crystal containing N electrons the continuous bands are replaced by N discrete electronic states often called quantum well states. Another important consequence of the finite crystal is that the presence of the surface can give rise to additional energy levels called surface states or surface bands. These surface states may reside in forbidden energy gaps of the bulk and are localized in a region near the surface. These two factors differentiate surface states from bulk states or discretized bulk (quantum well) states. Tamm [4] was the first to demonstrate the existence of surface states using the Kronig-Penney potential to approximate the crystal. The crux of his approach was the application of wave function matching conditions to join solutions in the crystal and the vacuum. Maue [5] and Goodwin [6] applied the wave function matching approach to the approximation of nearly-free electrons. Goodwin also developed a description of surface states within the tight-binding approximation (TBA) [7].

2.1.1 The Image Potential State

In addition to the loss of periodicity at the surface, there is an abrupt change in the electron density and the polarizability. The polarizability of the surface gives rise to a potential well near the surface known as the image potential. The image potential has long been recognized as a fundamentally important aspect of surface electrostatics. As such, it is an important factor in the electronic energy levels of adsorbed species, it affects the kinetic energy of photoemitted electrons, and it is the dominant force in molecular physisorption[1].

An electron in the vacuum near the surface is attracted to the polarization it induces in the surface. This problem is often solved in elementary electrostatics by the method of images [8, 9], in which the electron at a distance z from a surface interacts with a fictitious image charge of opposite sign located at $-z$. In the widely

[1]In the literature it is often assumed that the dominant force involved in physisorption of non-polar species is the interaction between the surface spill-out dipole and the polarizable adsorbate. However, the surface dipole potential is short ranged and the exchange-correlation potential (which can be described as a many-body description of the image potential) dominates.

used jellium model for surface electronic structure, the image potential is described as a many-body effect: The image potential is the real part of the exchange-correlation potential near a surface [10, 11]. When the substrate has a band gap in the vicinity of the vacuum level, the resulting potential well can support a Rydberg-like series of states converging to the vacuum level (Figure 2.1). This class of surface state is called the image state or image potential state.

Image states were first observed on the surface of liquid helium, where transitions were detected by microwave absorption [12]. The first evidence for image potential states on bare metals was obtained by inverse photoemission [13–15]. Giesen and coworkers were the first to study this class of surface states by two-photon photoemission (TPPE), using nanosecond pulsed lasers [16]. This and subsequent two photon photoemission work led to confirmation and refinement of the multiple reflection theory for image state binding energies on different single-crystal metal faces [17–19].

In recent years, studies have extended into the more complex and interesting systems where one or more molecular layers is adsorbed on a surface (see reviews by Fauster [20] and Harris and coworkers [21]). The study of adsorbate layers is substantially more challenging than the study of the clean surface. Experimentally, these studies are complicated by the various classes of surface bonding and growth modes for the adsorbed layers. The adsorption phase diagram can be quite complicated, including commensurate and incommensurate phases, 2-D liquid and 2-D gas phases, amorphous phases, coexisting phases, and structural phase transitions. It is also difficult to determine the origin of a given spectral feature which may be attributed to electrons in the substrate, the overlayer, the vacuum, or a combination of all three regions (mixed states). Development of an accurate model is confounded by many effects, including the complicated electrostatics of a heterostructure containing regions of differing dielectric constant, the transfer of charge between the overlayer and substrate, adsorbate-adsorbate interactions (polarization and orbital overlap), bonding between overlayer and substrate, energy band mismatch, adsorption-induced workfunction shifts, and the effects of crystal and layer steps and defects. Chemisorption and its complex and interesting relationship to surface and adsorbate electronic structure is discussed in a paper by Lang and Williams [22] and in a review by Muscat

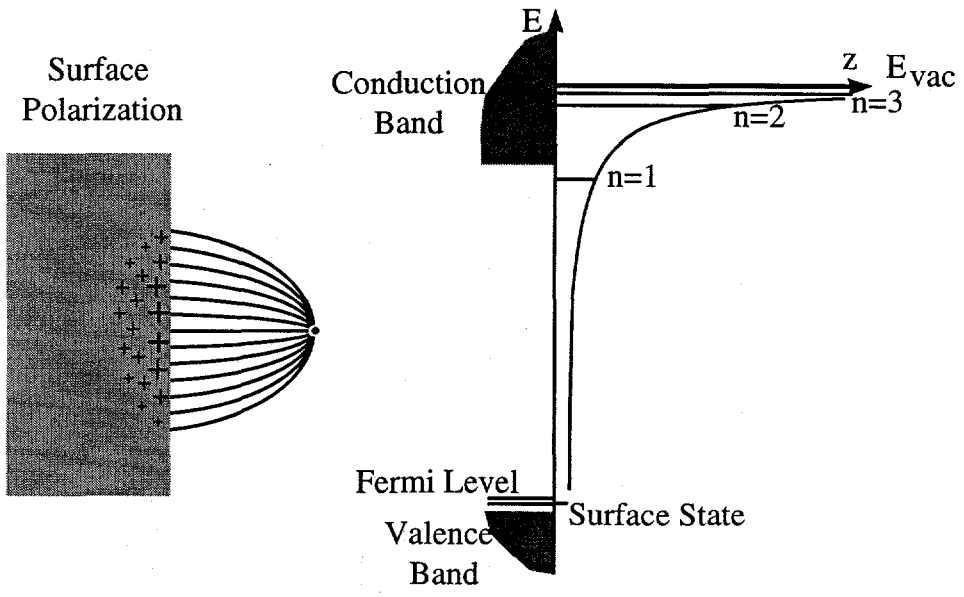

Figure 2.1: An electron near a surface is bound by an image potential which the electron induces by polarizing the material. Image states form a Rydberg series of states that converge to the vacuum level. The surface-projected Ag(111) band gap is shown here. Technically, the $n = 2$ and higher image states are resonances, since they are degenerate with the conduction band.

and Newns [23].

Despite these complications, the spectroscopy of image states has been shown to be an important tool in the study of interfaces. Steinmann, Fauster, and coworkers used the fact that image state binding energies are pinned to the local work function [24] to observe the growth modes of Ag, Au and Co on Cu(111) and Pd(111) [25–27] and have studied the evolution of metallic quantum wells for Au/Pd(111) [26]. These studies examine the formation of occupied valence band quantum well states of one free-electron metal on another and were recently reviewed [20].

2.2 Spectroscopy of Surface Electronic States

In order for a technique to be a candidate for surface electronic state spectroscopy, it should meet several suitability criteria. It should, first and foremost, be sensitive primarily to the surface. The resolution should, ideally, be better than the linewidth of surface state spectral features, which are on the order of a few meV in some cases, much narrower than bulk features. The technique must provide a method for populating and probing excited electronic states. The ability to resolve parallel momentum and to determine the dynamics of excited states is of substantial benefit: the additional experimental degrees of freedom help to sort out the various factors which contribute to the spectra of complex surface systems.

Techniques which have been used to study surface states include low energy electron energy loss spectroscopy (EELS), ultraviolet photoemission spectroscopy (UPS), X-ray photoemission spectroscopy (XPS), inverse photoemission (IPE), scanning tunneling microscopy (STM), and two photon photoemission (TPPE). XPS is useful in identifying the species, oxidation state, and bonding of chemisorbed and physisorbed layers as well as serving as a powerful tool for band structure spectroscopy. UPS is well-suited to characterizing the valence and conduction band structure of the substrate as well as occupied surface states. Here we shall only cover TPPE in detail because of the relevance to the current work. Also, much of the relevant recent experimental data relating to surface states was acquired using TPPE. There have recently been many advances to the technique of TPPE including improved resolu-

tion in time and energy and the development of additional applications for TPPE such as hot electron dynamics, coherent phase-locked TPPE and TPPE of quantum beat signals arising from closely spaced levels.

2.2.1 Photoemission Spectroscopy

Photoemission spectroscopy is a technique which is uniquely suited to the study of the electronic structure of interfaces. Electronic states of solids and surfaces have been studied extensively using photoemission measurements [28]. The process involves the absorption of a photon of known energy $h\nu$ near the surface of a solid, photoemitting an electron of initial energy E_i yielding an electron with the kinetic energy E_{kin}. By measuring the energy of the photoemitted electron, the energy of the initial state with respect to the vacuum energy can be determined. If the work function is known, then the energy of the state with respect to the Fermi level E_F can be obtained. The energy distribution curve of photoemitted electrons provides a picture of the initial density of states, provided the final states form a smooth continuum and the transition probability is homogeneous. With monocrystalline samples and clean, well ordered surfaces it is possible to determine the band structure at high symmetry points and lines of the Brillouin zone. Angle-resolved measurements yield additional information about the 3-D band structure. Photoemission is limited to the study of occupied initial states below E_F and unoccupied final states above the vacuum level. Final state results are scarce due to experimental considerations and the difficulty of interpreting final state photoemission results. Inverse photoemission spectroscopy and two photon photoemission spectroscopy provide access to surface and adsorbate states between the Fermi level and the vacuum level.

2.2.2 Inverse Photoemission

Inverse photoemission (IPE) refers to the class of experimental techniques in which a monochromatic electron beam is directed at the sample surface. A number of the electrons decay radiatively into unoccupied states. The photon energy for a given spectral feature is equal to the difference between the electron beam energy

and the final state energy. The resolution of IPE is limited by spectral width of the e-beam and the energy resolution of the photon detector and is typically on the order of several hundred meV. Inverse photoemission is so named because the technique is analogous to "time-reversed" photoemission. However, while photoemission yields the energies of occupied electronic states, IPE yields the energy of unoccupied electronic states. Recent developments in the field of IPE have been covered in several review articles [29–31]. Here we shall restrict ourselves to a discussion of the main features of IPE and a comparison to TPPE.

IPE is similar to TPPE in that both techniques are complementary to traditional photoemission spectroscopy, yielding the energies of states above the Fermi level. Parallel momentum is conserved in the IPE process. The IPE spectrum can be obtained as a function of parallel momentum by varying the angle of the incident electron beam with respect to the sample. Because of the relatively high energy of the electron beam (on the order of 10 to 20 eV), IPE is typically capable of sampling a larger range of $k_{||}$ than TPPE. Inverse photoemission may also be more well-suited to the spectroscopy of states above the vacuum level, though, in principle, TPPE may also be applied to the study of states in this energy range.

It is difficult to make a direct comparison between the signal levels for IPE and TPPE since the TPPE response depends on the peak laser power. According to first-order perturbation theory, the ratio of the cross-section for IPE versus the cross-section for photoemission is given by [28]

$$R = \left(\frac{\lambda_e}{\lambda_{\hbar\omega}}\right)^2 . \tag{2.1}$$

Qualitatively, this reflects the available phase space for the final state particles. Typically, R is on the order of 10^{-5}, which explains the low signal/noise ratio typically observed in IPE spectra.

An important difference between inverse photoemission and traditional photoemission or TPPE is that the IPE process does not involve the generation of an electron vacancy or hole. This is generally not an issue in TPPE spectroscopy of metals where the hole is rapidly and effectively screened owing to the high density of carriers. For semiconductors and insulators, where screening is less effective because

of the lower number of carriers, there may be a notable difference between TPPE and IPE measurements related to imperfect screening of holes.

2.2.3 Two Photon Photoemission Spectroscopy

Time-resolved two photon photoemission is a relatively new technique which is uniquely suited to the study of the electronic structure and dynamical processes at interfaces and offers several advantages over PE and IPE. The advantages include applicability to the energy range between E_F and E_{vac}, good energy resolution (comparable or better than that of other electron spectroscopies), ultrafast (femtosecond) time resolution, surface sensitivity, and low background. The technique is quite simple and elegant, conceptually. A photon of energy $h\nu_1$ from a laser pulse is absorbed at a surface, imparting its energy to an electron at or below the Fermi energy level in the solid and elevating it to an excited intermediate state of the interface. Some time later, a photon of energy $h\nu_2$ from a second laser pulse is absorbed, imparting enough energy to eject the electron from the surface. The free electron then travels to a detector which records its energy and direction.

The TPPE spectrum is a distribution of electron kinetic energies. The energies of the intermediate states can be determined by subtracting the energy of the second photon $h\nu_2$. The angle of the photoemitted electrons can be used to determine the energy as a function of the parallel momentum of the intermediate electronic state, referred to as the dispersion of the state. In addition, the population dynamics of intermediate states can be determined by varying the time delay between pump and probe laser pulses.

Surface two photon photoemission was first developed and applied to the study of surface states by Giesen and coworkers [16] in 1985. This work constituted the first high-resolution spectroscopy results for the image states of Ag(111), Cu(111), and Ni(111) surfaces. Much of the early work concentrated on the energies of image states and surface states for a variety of transition metal crystal faces. Two review articles cover much of the results and development of the technique [32, 33] during the first few years.

Later, the application of angle-resolved TPPE yielded measurements of the dispersion of image states. The dispersion of image states, $E(k_{||})$, is determined by obtaining TPPE spectra at a series of angles. Dispersion measurements have been obtained for a wide number of crystal faces of transition metals [18, 24, 32, 34, 35]. The results of dispersion measurements are often described in terms of a quasiparticle effective mass. Initial theory for image state dispersion predicted an effective mass of near unity for all crystal faces, except for measurements at high $k_{||}$ where the two band model is not accurate.

In the last few years the initial promise of ultrafast laser techniques coupled with TPPE has been largely realized, and even more important results and advances in the technique are sure to follow. Importantly, TPPE is no longer merely a tool for the study of image potential states. Increased signal levels, improved time resolution, and a wider wavelength range have extended the reach of TPPE to an ever wider range of processes and systems including hot electron dynamics and transient molecular anions. Still, many important dynamical processes involving electrons which are known or thought to take place on surfaces have yet to be characterized.

The team of Knoesel, Hertel, Wolf, and Ertl applied femtosecond time-resolved TPPE to the study of CO on Cu(111) [36,37]. Later they applied the same technique to the optical response of hot electrons for the same crystal face [38]. According to their analysis of the data, the results yielded a qualitative agreement with Fermi liquid theory. These results were later disputed by Petek and coworkers [39] who determined that the lifetimes deviated substantially from the $(E - E_F)^{-2}$ functional form predicted by the standard Fermi liquid theory. A qualitative agreement with the theory was reached when the band structure of Cu was taken into account, though the calculated lifetimes were a six times faster than the measured lifetimes. The failure of the free electron model in predicting the energy dependence and magnitude of the scattering times is attributed in part to d band electrons, which can participate in both scattering and screening of hot electrons.

Time-resolved TPPE was also used to compare the dynamics of image states on clean Cu(111) to the dynamics of the image state for a monolayer of Xe on the same surface [40]. Qualitative agreement was reached with the results of a penetration

model assuming the primary effect of the Xe layer was the lowering of the work function. However, the near degeneracy of the Cu(111) conduction band with the image state invalidates the results of the penetration model, since the model requires that the state be in the band gap of the substrate. Since small changes in the model parameters yield wildly different results, agreement between the model and the experiment may be assumed to be due to a fortuitous choice of model parameters and not a strong indication of the correctness of the model. A more important contribution of this paper was the treatment of coherence dephasing using the optical Bloch equations [41] for a single resonant transition between two levels. Later work has shown that a two step Bloch model does not adequately describe two photon photoemission [42]. Interestingly, the more complex three step model yields results for lifetime (T_1) which are similar to those obtained by use of the rate equations (which do not include dephasing).

In a later paper [43], hot electron results are interpreted in terms of simple rate equations rather than the optical Bloch equations which were employed earlier [40]. It was determined that most of the photon energy is absorbed by d band electrons. It was also determined that d band hole states possess roughly twice the lifetime of sp band electronic states, probably due to the highly localized nature of the d band hole state, since localization most likely reduces the probability of scattering events. The authors also found that approximately half of the excited electron distribution is removed from the surface region by ballistic electron transport within 20 fs of the initial excitation.

Aeschlimann and coworkers have used ultrafast time-resolved TPPE to study a variety of complex systems of broad interest, including magnetic thin films [44–47], alkali layers [48, 49], chemisorbed oxygen [50], and hot electron dynamics. In a recent paper in which the spin-resolved hot electron dynamics were determined for the Co(001) surface, it was found that the lifetime of excited electrons of the majority spin is twice as long as that of the minority spin carrier. Importantly, the results demonstrate the feasibility of studying spin-dependent electron dynamics in ferromagnetic solids directly in the time domain (as opposed to static bulk transport measurements), providing a unique and detailed perspective on electron transport in

ferromagnetic solids and films.

Petek and coworkers have concentrated their efforts on the study of hot electron dynamics [39] and the fundamental aspects of the interaction of short laser pulses with electronic states at or near the surface [42]. They extended the technique of ultrafast two photon photoemission by using phase-locked laser pulses, and were thus able to obtain time and phase-resolved information on the laser-induced polarization at the surface. It was found that, in addition to the initial oscillations at the laser frequency ω, there is an oscillation at a frequency of 2ω corresponding to the second harmonic. It was determined that the appearance of the second harmonic is not instantaneous. In their work on hot electron dynamics, Ogawa and coworkers find a dependence on the crystal face. Petek and Ogawa have written a review [51] on recent findings in the field of ultrafast laser spectroscopy of electrons in metals. Recently, the ultrafast kinetics of desorption precipitated by the transfer of an electron from the metal substrate to an adsorbed alkali atom were measured [52]. This work will likely lead to additional application of the TPPE technique to the spectroscopy of transition states on surfaces.

2.2.4 Angle resolved Two Photon Photoemission

Angle resolved two-photon photoemission (ARTPPE) and angle resolved inverse photoemission experiments can be used to measure the dispersion of image states. The dispersion is the relation between energy and parallel momentum ($E(k_{||})$) for a given band. A related technique, angle resolved photoemission spectroscopy, has proven to be a useful extension of photoemission spectroscopy. The additional experimental parameter greatly increases the amount of information obtainable by photoemission experiments, providing detailed information about the three-dimensional band structure. Similarly, angle resolved two-photon photoemission yields additional information about excited surface bands.

The angle between the detector axis and the surface normal can be related to the parallel momentum $k_{||}$ associated with a given spectral feature using the relation

$$k_{||} = \hbar^{-1}\sqrt{2mE}\sin\theta, \tag{2.2}$$

where θ is the angle of the detector with respect to the surface normal. Often, the dispersion can be described by an effective mass parameter. The effective mass of image states is discussed in detail in a later section.

2.3 Theoretical Models of Surface States

There are essentially two broad classes of approaches to the modeling of surface states: *ab-initio* and empirical. The *ab-initio* approach more or less completely simulates the system of interest, solving the complete Schrödinger equation for a sufficiently large slab. Such calculations are often computationally expensive, and often possess limited explanatory power in terms of physical properties or trends. Experimentalists attempting to establish trends and determine physical properties often rely on approximate solutions and empirical models which employ physical properties obtained by experiment in order to predict physical properties, spectral features, and trends. These models are typically based on a simplified hypothetical system which treats a small subset (hopefully the most important subset) of the processes and interactions encompassed by a more complete treatment of the system.

Multiple Reflection Theory (MRT), proposed by Echenique and Pendry [17], and its variants, constitute a useful, empirical approach to the problem of image states. The power of the multiple reflection approach rests in its simplicity and its ability to account for differences in image state binding energies on various crystal faces, as well as its reliance on the well-known two band nearly-free-electron theory and such physical parameters such as the positions and widths of the substrate bands. Multiple reflection theory is a piecewise approach to the image state problem: appropriate wavefunction solutions in the substrate and vacuum are joined at the surface where eigenenergies are determined by solving the resulting boundary value problem. The following subsections illustrate approximate potentials and wavefunction solutions in the vacuum and in the substrate and are followed by a discussion of the multiple reflection method for determining bound states.

2.3.1 The Image Potential or Surface Barrier

Consider the case of an electron at a distance z outside a perfect conductor. From elementary electrostatics it is known that the electric field must vanish at the conductor surface. This boundary condition defines the electric field. A solution can be obtained by applying the method of images: an imaginary positive charge at an equal distance $-z$ from the conductor surface (an image charge) cancels the field at the surface satisfying the requirement that the field vanish at the surface. Since the interaction of the electron with its image is Coulombic, the resulting image potential takes the form of a Coulomb potential [17]:

$$V = -\frac{Z}{z}, \tag{2.3}$$

where z is the distance from the conductor surface and Z is a coupling constant related to the static dielectric constant ϵ:

$$Z = \frac{1}{4}\frac{\epsilon - 1}{\epsilon + 1}. \tag{2.4}$$

For a perfect conductor $\epsilon = \infty$ and $Z = 1/4$. If the potential approaches $V \to -\infty$ as $z \to 0$, the energy levels[2] with respect to the vacuum level are given by:

$$E_b = \frac{-Z^2}{2n^2} = \frac{-13.6 \text{ eV}}{16n^2} \tag{2.5}$$

For an electron outside an insulating material with a low dielectric constant, Z is smaller resulting in a lower binding energy.

The image potential at a realistic metal surface, while exactly Coulombic for large z, differs substantially from the Coulomb form within an Ångstrom or so of the surface: At metal surfaces electron density profile in the surface region tapers off smoothly from the bulk electron density some distance inside the metal to essentially zero a short distance outside the metal. The electron density is said to "spill out" from the surface. The resulting charge distribution gives rise to the surface dipole

[2]Elsewhere it is stated that Equation 2.5 only holds for an infinite potential barrier ($V = +\infty$) at $z = 0$. According to the properties of the confluent hypergeometric functions solutions for the Coulomb potential, the divergence of the potential in the region near $z = 0$ is more important than the potential at a single point. The infinite barrier at $z = 0$ merely serves as a way to emphatically remove from discussion any contribution from substrate electronic structure.

(spillout dipole) which contributes to the work function. As a negative test charge approaches the surface, electron-electron repulsion with the electron density outside the surface replaces the singularity near $z = 0$ present in the classical image potential with a smooth function which joins to the potential of the crystal interior. The connection with the interior crystal potential is responsible for the substrate-induced deviations from hydrogenic binding energies. A thorough discussion of a realistic quantum mechanical form of the image potential from a density functional point of view is available in a review article [19] and has been refined recently [53]. In the density functional treatment of surfaces, the image potential is the tail of the exchange-correlation potential outside the surface[3].

In the multiple reflection theory for image states and some related theories, the image potential is approximated by a Coulomb potential with a flat cutoff potential in the region closest to the surface. The wavefunction solution to the time-independent Schrödinger equation for the image potential region which matches the solution in the cutoff region and properly vanishes at infinity is a confluent hypergeometric function known as the irregular Whittaker function [54,55], $W_{\lambda,\mu}(\rho)$, where $\mu = 1/2$, $\lambda = Z/\sqrt{2E}$, $\rho = 2z\sqrt{2E}$, and $Z = 1/4$ for a metal image potential, and E and z are the energy and distance in atomic units.

2.3.2 The Two Band Nearly-Free-Electron Model

The two band nearly-free-electron (NFE) model describes an electron in a weak periodic potential [3]. It is a simple model which describes the electronic structure of ordered materials in terms of energy bands and is discussed in solid state physics textbooks [56, 57]. It is often invoked to describe the conductivity of simple metals and insulators in terms of a forbidden energy gap. The two band nearly free electron model is also the basis for many models surface and image states [58–60]. For an

[3]In some approximate forms of density functional theory, most notably the local density approximation (LDA), the exchange-correlation potential does not possess the correct asymptotic $1/z$ form but rather decays exponentially for large z. This is a consequence of neglecting nonlocal effects; LDA assumes the electron and its exchange hole are attached. When LDA methods are used in calculating image potentials, a correction must be applied [53].

infinite, perfectly crystalline solid, the crystal potential is periodic:

$$V(\mathbf{r}) = V(\mathbf{r} + \mathbf{a}), \tag{2.6}$$

where $\mathbf{a}$ is a primitive translation vector of the lattice. According to the well-known Bloch-Floquet theorem, the wavefunction solutions for a single electron in this potential are also periodic and are given by

$$\psi(\mathbf{r}) = u_{\mathbf{k}}(\mathbf{r})e^{i\mathbf{k}\cdot\mathbf{r}}, \tag{2.7}$$

where $u_{\mathbf{k}}(\mathbf{r})$ is periodic with the lattice. States of this form are said to be Bloch states.

In the following theoretical discussion, a one dimensional approximation of the two band model is used. In applying this approximation to a 3-D crystal, it is assumed that the Hamiltonian for the system is approximately separable into perpendicular and parallel components. Generally, it is assumed that $k_{||} = 0$ and the contribution of $\mathcal{H}_{||}$ to the total energy is assumed to be a constant.

Here only the major features of the two band model will be outlined. The notation is adapted from Smith [61]. In the two band NFE approximation the 1-D crystal potential is written as a Fourier expansion in multiples of the reciprocal lattice vector $g = 2\pi/a$:

$$V(z) = \sum_n V_{ng} e^{ingz}. \tag{2.8}$$

The potential fluctuations are assumed to be weak, so only the first two terms, V_g, V_{-g} are kept and the higher order terms are ignored. For crystals with inversion symmetry $V_g = V_{-g}$. Electron energies ε with respect to the zero of energy (here taken to be the band energy at zone center) for the two-band NFE model are given by solving the secular equation

$$\begin{vmatrix} (\hbar^2/2m^*)k^2 - \varepsilon & V_g \\ V_g & (\hbar^2/2m^*)(k-g)^2 - \varepsilon \end{vmatrix} = 0. \tag{2.9}$$

At the zone boundary located at $k = g/2$ (in momentum or reciprocal space) there is an energy gap of width $2|V_g|$. Figure 2.2 illustrates the roots of Equation 2.9 and how the parameters of the two band NFE model are related to the position

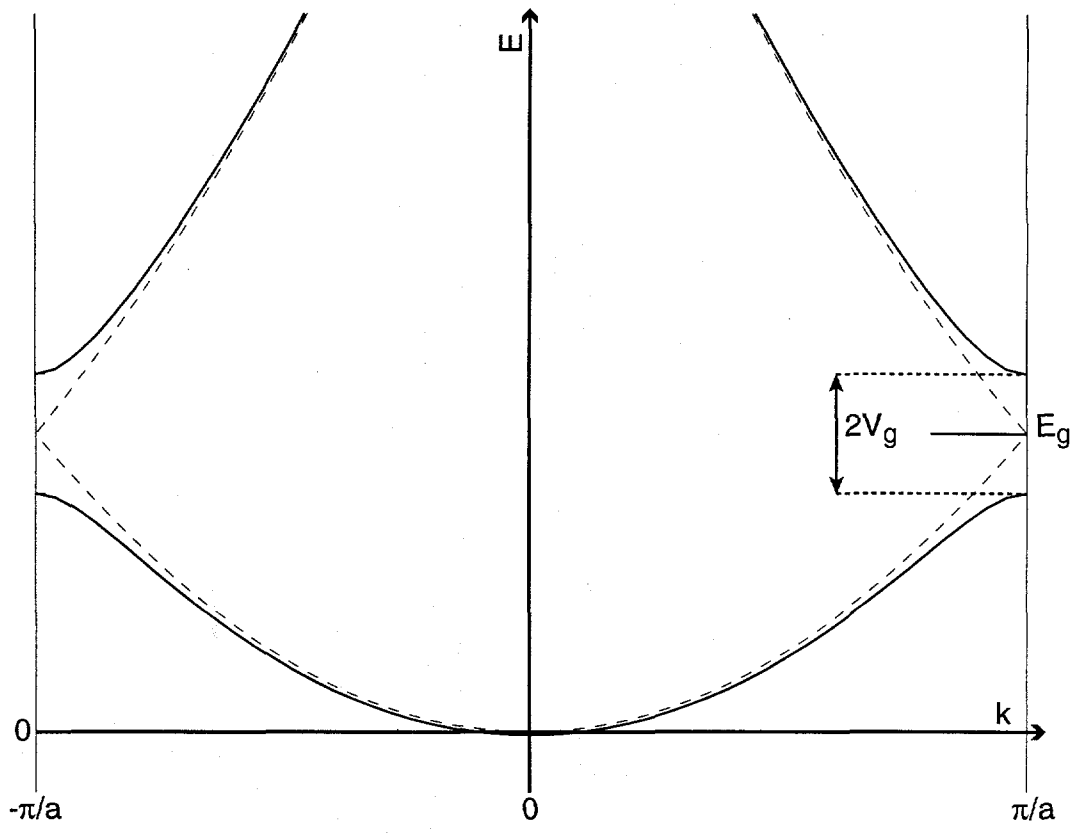

Figure 2.2: The main features of the two band nearly-free-electron model are the gap energy E_g and gap half width V_g at the $g/2 = \pi/a$ zone boundary. The upper and lower solid curves are the roots of Equation 2.9 as a function of k. The dashed curve is the solution for $V_g = 0$, which corresponds to the case of a perfectly free electron.

and widths of the valence and conduction bands. Within the gap solutions exist for complex k, which correspond to an evanescent wave decaying into the metal. The wave vector can be represented as a sum of real and imaginary components, $k = p + iq$.

For the 1-D case corresponding to solutions along the surface normal Equation 2.9 yields the standard results

$$p = g/2, \tag{2.10}$$

$$(\hbar^2/2m^*)q^2 = (4\varepsilon E_g + V_g^2)^{1/2} - (\varepsilon + E_g), \tag{2.11}$$

$$E_g = (\hbar^2/2m^*)p^2, \tag{2.12}$$

$$\sin(2\delta) = -(\hbar^2/2m^*)(2pq/V_g), \tag{2.13}$$

where E_g is the midgap energy, m^* is the effective mass, $g = 2\pi/d$ where d is the interplanar spacing, and δ is a wave-function phase[4]. The wave function in the crystal is given by

$$\psi = e^{qz}\cos(pz + \delta). \tag{2.14}$$

For energies within the valence or conduction bands, the imaginary part of the wavevector, denoted by q is zero. Within the gap $q > 0$ which causes the wavefunction of Equation 2.14 to exponentially decay away from the surface. The maximum value of q is given by

$$\frac{\hbar^2}{2m^*} g q_{max} = |V_g|. \tag{2.15}$$

The energy corresponding to q_{max} is given by

$$\varepsilon(q_{max}) = \frac{4E_g^2 - V_g^2}{4E_g}. \tag{2.16}$$

The sign of V_g depends on the symmetry of the wave function at the top and bottom of the gap. For Ag(111) the band gap is *sp* inverted: solutions are *s*-like at the top of the gap and *p*-like at the bottom. This case corresponds to $V_g > 0$.

[4]For *sp* inverted band gaps, the correct branch of the arcsin required to solve for δ in Equation 2.13 can be determined by requiring that $\delta = 0$ at the bottom of the gap, $\delta = \pi/4$ at the middle of the gap where $|q|$ is at a maximum and $\delta = \pi/2$ at the top of the gap.

By itself, the two band model possesses limited predictive value for a given system. However, the values of E_g, V_g, which are the energy (with respect to the energy zero at zone center) and half width, respectively, of the band gap, can be taken from experimental results or state of the art band structure calculations, yielding a parameterized model which has proven useful in describing the electronic structure of the substrate in models of surface states and quantum well states. The two band NFE model has proved useful in describing the effects of the energy gap and electron occupancy on the conductivity of simple metals and insulators. The details of the multiple reflection model, which uses the two band NFE approximation, are discussed below.

2.3.3 Multiple Reflection Theory

Multiple reflection theory, also referred to as the phase shift model for surface states, is a method for solving the internal boundary value problem where two band nearly-free-electron wavefunction solutions for the metal connect to (Whittaker function) solutions for the image potential at the surface. The model is based on the reflective properties of the potential barriers presented by the substrate lattice and the image potential. A plane wave is constructed in the (infinitesimal) region between the metal and the image barrier. If a wave ψ^- carries a unit of flux towards the crystal, a portion of the wave will be reflected. The reflected wave will have the form

$$r_C e^{i\phi_C}\psi^+, \tag{2.17}$$

where r_C and ϕ_C are the modulus and phase of the crystal reflectivity and ψ^+ is a wave which carries a unit of flux away from the crystal. When this wave is reflected from the surface (image) barrier where r_B and ϕ_B are the modulus and phase of the barrier reflectivity, the resulting wave is

$$r_B e^{i\phi_B} r_C e^{i\phi_C}\psi^-. \tag{2.18}$$

Upon repeated scatterings, the total amplitude for ψ^- is given by the geometric sum

$$\frac{1}{1 - r_B r_C e^{i(\phi_B+\phi_C)}}. \tag{2.19}$$

A pole in Equation 2.19 denotes a bound state of the surface. Assuming unity reflection coefficients the bound state condition is

$$\phi_C + \phi_B = 2\pi n. \tag{2.20}$$

Expressions for ϕ_C and ϕ_B are derived from solutions in the crystal substrate and in the vacuum.

The phase shift ϕ_B for the image barrier is defined by matching the wavefunction for the image barrier to a plane wave of the form

$$\psi = e^{ikz} + r_B e^{i\phi_B} e^{-ikz}. \tag{2.21}$$

In the present context, wavefunction matching is performed by determining the logarithmic derivatives[5] of both the plane wave and the wavefunction solution in the vacuum (Equation 2.14), setting them equal, and solving for ϕ_B. As stated earlier, the wavefunction solution in the vacuum region is the irregular Whittaker function $W_{\lambda,\mu}(\rho)$ where $\mu = 1/2$, $\lambda = Z/\sqrt{2E}$, $\rho = 2z\sqrt{2E}$, and $Z = 1/4$ for the case of an image potential, and the energy E and the coordinate z are in atomic units. The resulting expression for the phase shift of a unit of flux traveling from the origin towards the Coulomb barrier is

$$\phi_B = 2k_c z_0 + 2\tan^{-1}\left(\frac{2\sqrt{2E}}{k_c}\frac{W'_{\lambda,\mu}(\rho_0)}{W_{\lambda,\mu}(\rho_0)}\right), \tag{2.22}$$

where $W'_{\lambda,\mu}(\rho_0)$ is the derivative with respect to ρ, k_c is the wave vector in the cutoff region [54], $\rho_0 = 2z_0\sqrt{2E}$, and z_0 is the cutoff distance[6]. The value of ϕ_B increases rapidly as E approaches zero, causing the total phase shift to increase rapidly which therefore sweeps though the bound state condition more frequently. This is consistent with the Rydberg-like series of states converging on the vacuum indicated in Equation 2.5.

A useful approximation to ϕ_B has been derived that reproduces the hydrogenic limit (Equation 2.5) and illustrates the dependence of ϕ_B on energy [19],

$$\phi_B(E) = \left(\frac{2Z}{\sqrt{-2E}} - 1\right)\pi. \tag{2.23}$$

[5]The logarithmic derivative of ψ with respect to x is defined as $d/dx(\ln\psi)$ or equivalently ψ'/ψ.

[6]A cutoff is used to approximate the flattening of the image potential arising from electron-electron repulsion of the image electron with the electron gas near the metal surface.

This result is referred to as the interpolation formula for the barrier phase shift ϕ_B and is reliable for determining trends in binding energies of image states. A comparison of the phase shift as a function of energy for the the interpolation formula and the quantum-mechanical expression reveals that the quantum-mechanical phase shift oscillates about the interpolation formula phase shift.

The crystal phase shift ϕ_C is determined by matching the plane wave of the form

$$\psi = e^{-ikz} + r_C e^{i\phi_C} e^{ikz} \tag{2.24}$$

to the Bloch wave in the bulk given by Equation 2.14. The resulting expression for ϕ_C is given by

$$k \tan\left(\frac{\phi_C}{2}\right) = p \tan(pa/2 + \delta) - q. \tag{2.25}$$

assuming the metal terminates at a distance equal to half the interlayer spacing outside the last layer of cores (half layer termination).

For *sp* inverted band gaps[7], the crystal phase shift varies from $\phi_C = 0$ at the bottom of the gap to $\phi_C = \pi$ at the top of the gap. Considering the value of ϕ_C at the bottom and the top of the gap, the bound state condition of Equation 2.20 can be satisfied near the bottom of the gap when

$$\phi_C = -\phi_B. \tag{2.26}$$

This yields the surface state, which derives its name from the observation that the maximum in probability density is near the surface. Near the top of the gap the phase shift is approximately π in which case the bound state condition is approximately

$$n = 0, 1, 2, ..., \tag{2.27}$$

$$\phi_B = (2n + 1)\pi, \tag{2.28}$$

which yields the results of the hydrogenic approximation.

[7]A band gap is said to be *sp* inverted when Bloch states of *s* orbital symmetry (where the wave function amplitude is largest at the atom cores) are higher in energy than Bloch states of *p* orbital symmetry (where the wave function amplitude is largest between neighboring atoms in the lattice). The inversion is attributed to the contribution of *d* orbitals to the hybridized band, the effect of which is to lower the energy of the *p* band states with respect to the *s* band states.

It should be noted that the use of logarithmic derivatives to determine the phase shifts in Equations 2.22 and 2.25, together with the bound state condition $\phi_C + \phi_B = 2\pi n$ (Equation 2.20) ensure that the total wavefunction is continuous in slope and value. In fact, it can be easily shown that the phase shift requirement is only met when the logarithmic derivatives of the solutions in the bulk and in the vacuum are equal at $z = 0$.

In order to illustrate the use of multiple reflection theory to describe image and surface states, the results of calculations of the $n = 0$ surface state and the $n = 1$ and $n = 2$ image states on the Ag(111) surface are shown here. The parameters used in the calculation are listed in Table 2.1 along with experimental and calculated energies for the image and surface states. The interplanar spacing a along the (111) direction for Ag is 2.36 Å. The parameters E_g, V_g, and E_F are taken[8] from a review article by Fauster and Steinmann [62] and the experimental numbers were obtained from the apparatus described later. The calculated probability densities $\psi^*\psi$ are shown in Figure 2.3. The $n = 1$ image state is similar to the hydrogenic $n = 1$ state, with a node near the metal surface and a relatively small probability density in the metal. The $n = 2$ state also has a node near the metal surface, but is degenerate with the conduction band, hence it does not decay exponentially into the metal as the $n = 1$ state; the $n = 2$ wavefunction extends infinitely into the metal. The $n = 0$ state is often referred to as the surface state, as it possesses a maximum (instead of a node) near the surface plane and does not belong to the hydrogenic image series. The $n = 0$ state is present in the model only when the valence band is of s orbital symmetry.

Multiple reflection theory successfully accounts for the existence of image and surface states within a single formalism and has been useful in attributing differences in the positions of image and surface states on different crystal faces to differences in positions of the vacuum level and the band gap. For more complicated systems,

[8]The review [62] actually lists a value of 2.15 for V_g. In their approach, the work function Φ is treated as an adjustable parameter and the interpolation formula (Equation 2.23) is used to evaluate ϕ_B which yields results which differ from those obtained from the Whittaker functions. The value of 2.075 is taken from Merry [63] who determined the value for V_g by subtracting experimental values for the conduction [32] and valence [64] bands.

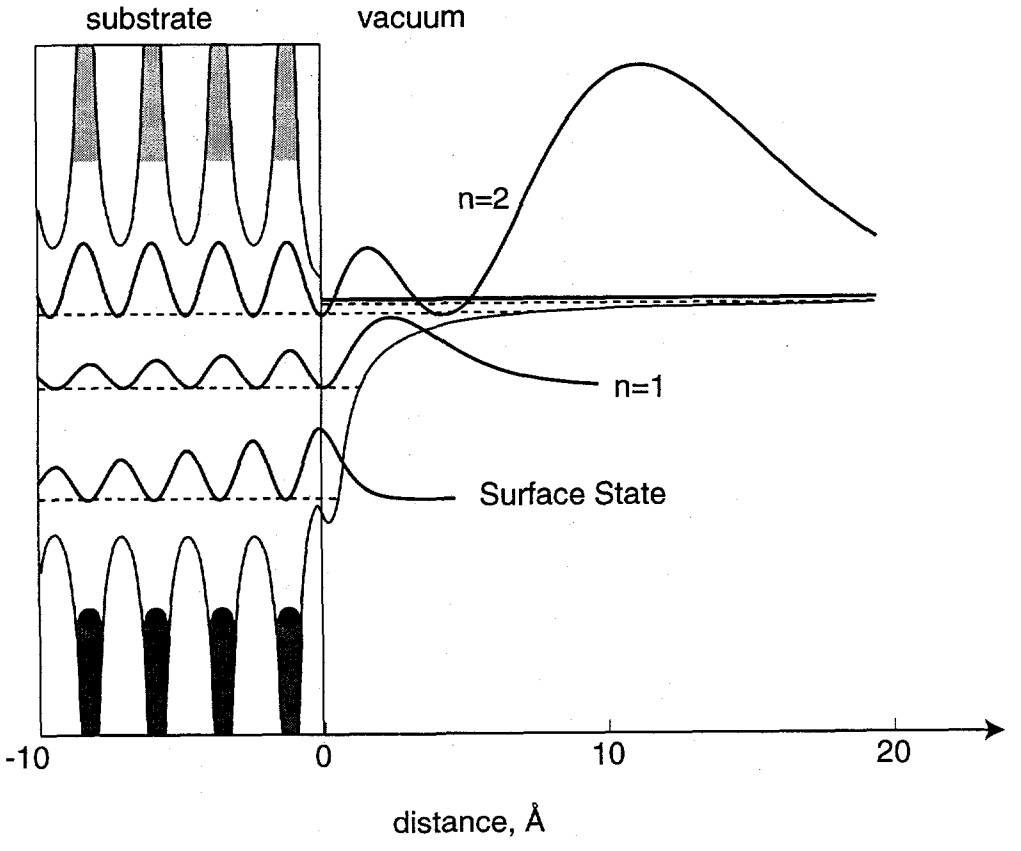

Figure 2.3: Probability densities for the $n = 0$ surface state and the $n = 1, 2$ image states for Ag(111). The potentials are for illustrative purposes only and do not represent a realistic crystal potential.

Sample	V_g	E_g	E_f	Φ	State	E Theo.	E Exp.	z_0
Ag(111)	2.075	9.64	7.865	4.56	n=0	-4.65	-4.61	.6
					n=1	-.76	-.77	.1
					n=2	-.21	-.21	.1

Table 2.1: Multiple Reflection Theory parameters and resulting binding energies for $n = 0, 1, 2$ for Ag(111). The energy values are in eV. V_g is the gap half width, E_g is the position of the gap with respect to zone center (the Γ point), E_f is the Fermi level with respect to Γ, and Φ is the work function. The cutoff distance z_0 in the image potential is in units of Ångstroms. The energies of $n = 0, 1, 2$ are with respect to the vacuum level.

simple expressions for ϕ_C or ϕ_B are not available, which limits the utility of the phase shift approach. In such cases, it is more straightforward to employ numerical integration to determine the wave function for potential regions for which simple analytical forms of the solution are not available.

2.3.4 Effective Mass of Image States

As mentioned earlier, the result of a series of angle-resolved two photon photoemission measurements of a given spectroscopic feature is the relation between energy and momentum in the surface plane $E(k_{||})$ called a dispersion curve. Often the dispersion curve may be conveniently described by an effective mass parameter. The effective mass m^* associated with a given spectral feature is defined by the expression,

$$E = E_0 + \frac{\hbar^2 k_{||}^2}{2m^* m_e}, \tag{2.29}$$

where m^* is expressed as a fraction of the mass of a free electron. Qualitatively, the effective mass or dispersion of image and surface state electrons is a measure of the influence of the substrate bands. For quantum well states, the parallel dispersion is related to the 3-D band structure.

It has been shown [32] that the effective mass or dispersion of image and surface states of several crystal surfaces can be explained in terms of the properties of the surface projected bulk band structure, shown in Figure 2.4 for Ag(111) along with

the dispersions of the $n = 0$ and $n = 1$ bands. The effective mass of the surface projected conduction band in Figure 2.4 is 1.6 m_e according to the literature [32]. The aptly named surface projected bulk band structure is the 3-D bulk band structure projected onto a given surface plane. The presence of a band at a given energy E and parallel momentum $k_{||}$ indicates the existence within the full 3-D band structure of one or more band states at that energy with a momentum whose projection onto the surface plane[9] is $k_{||}$. The presence of a gap in the surface projected bulk band structure indicates an absence of states over the range of energy and surface projected momentum which describes the gap.

The work of Giesen, and coworkers [32] describes the effective mass of surface and image states in terms of the reflective properties of the associated surface projected band gap. As shown in Figure 2.4, the upper and lower gap edges each possess a different dispersion in the surface plane and may cross, closing the gap at some value of $k_{||}$. For *sp* inverted bands like the valence and conduction bands of Ag(111) the phase shift ϕ_C of the conduction (or upper) band edge is π and the phase shift of the lower band edge is zero. At a given energy, the crystal phase shift as a function of $k_{||}$ does not remain constant but rather decreases since the distance from the upper band edge increases (assuming an upwardly dispersing band as in Figure 2.4).

The effect of this variation in crystal phase shift on the effective mass can be estimated using a geometric construction [32]. A hypothetical hydrogenic $n = 1$ image state on a perfectly reflecting substrate possesses a binding energy of $-\mathrm{R}yd./16$ or $-.85$ eV and an effective mass of unity. Assuming that the effective mass of the upper bulk band edge is larger than that of the electron (as is the case for Ag(111)), the hydrogenic image state will cross the upper band edge at some value of $k_{||}$. At the point where the hydrogenic image state crosses the band edge, the phase shift is π. Therefore, at this point the energies of the hydrogenic image state and the real image state should be equal. This point and the measured binding energy at $k_{||} = 0$ define the dispersion parabola of the image state and thus its effective mass.

[9]The state or states of the crystal which correspond to a point in a surface-projected band may also possess a nonzero $k_\perp$ in the range of zero to $\mathbf{g}/2$. For example, the state corresponding to the valence band edge at $k_{||} = 0$ possesses a $k_\perp$ of π/a.

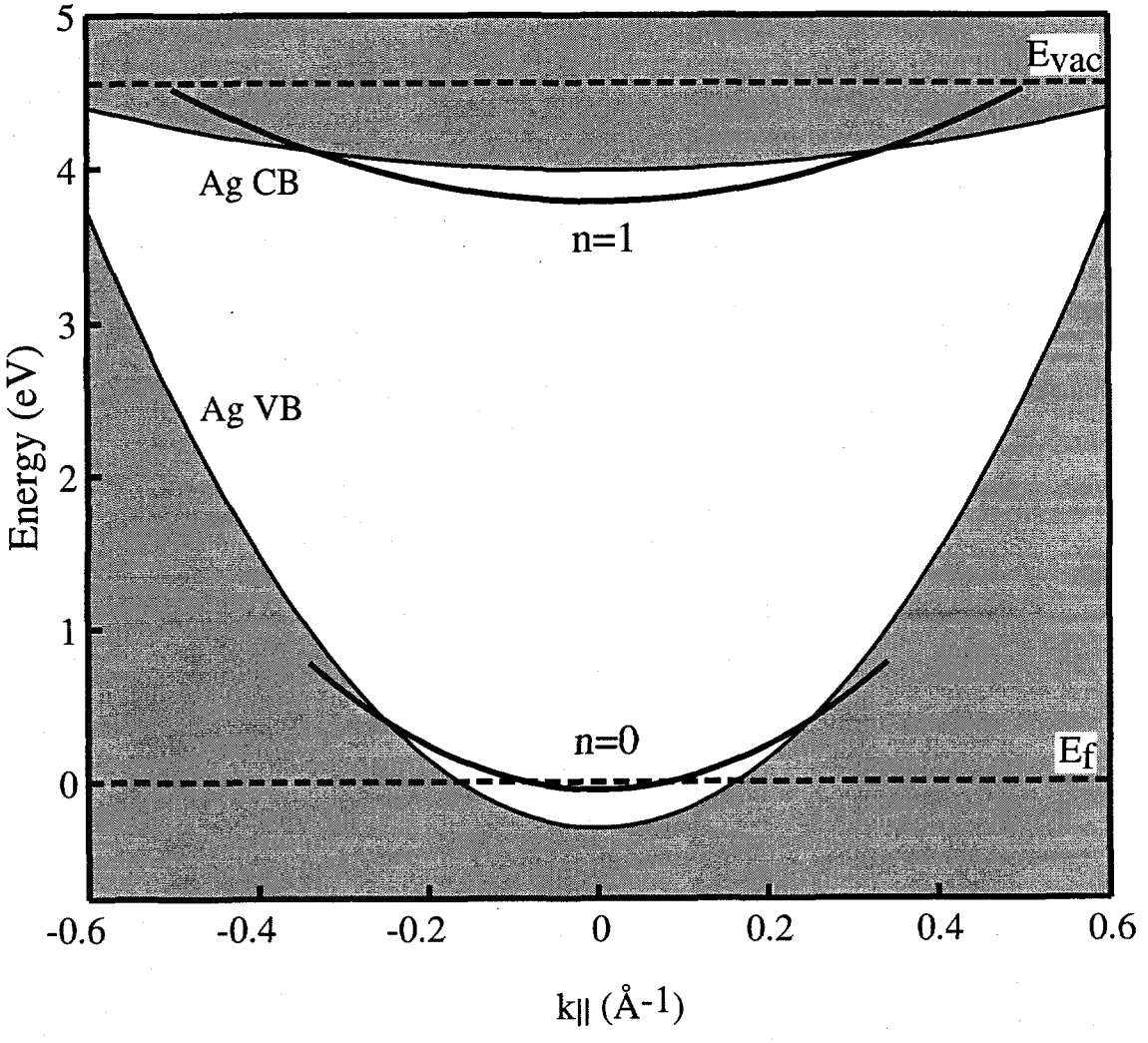

Figure 2.4: The surface projected bulk band structure of Ag(111). The dispersions of the $n = 0$ surface state and the $n = 1$ image state are also shown. The surface projected valence and conduction bands are indicated by the lower and upper shaded areas, respectively. The surface projected band gap is the region between the surface projected valence and conduction bands.

A diagram of this construction for the $n = 1$ state on Ag(111) is shown in Figure 2.5.

If the point where the hypothetical hydrogenic free electron crosses the upper band edge is labelled E_C, $E_H = -.85$ eV is the energy of the hydrogenic image state, and E_{IS} is the energy of the real image state at $k_{||} = 0$, the effective mass is given by the expression

$$\frac{m^*}{m_e} = \frac{E_C - E_H}{E_C - E_{IS}}, \tag{2.30}$$

which is derived from the geometric construction. This result agrees with the experimental observation that the effective mass of image bands is larger than unity when the image state is relatively near a surface projected bulk band which has a large effective mass, while the effective mass of image bands is less than unity when the image state is relatively near a surface projected bulk band which has a low effective mass. Qualitatively, it can be said that the image band is partially repelled by nearby bulk bands.

Prior to the development of this model for effective mass based on the crystal reflectivity, the excess effective mass of image states ($m^*/m_e = 1.3$ for $n = 1$, Ag(111)) was attributed to a variety of physical mechanisms, including surface corrugation [65], coupling with electron-hole pairs [66, 67], and coupling with surface plasmons [68]. However, none of these mechanisms could account for the wide variation in effective mass observed for the various crystal faces of Ag and Cu. The simpler approach based on the reflective properties of the surface projected band structure succeeds because most of the physics relevant to image state dispersion (including some of the effects mentioned above) is represented in the surface projected band structure. The geometric model of the effective mass is only applicable to the clean surface and does not adequately explain the effective mass of surface or quantum well states in the presence of an adsorbate layer. An attempt to develop a method for treating the effect of the overlayer in the effective mass approximation is detailed in Chapter 4.

2.3.5 Lifetime of Image States

The lifetime of image states has been the subject of theoretical and experimental investigation since the existence of image states was proposed [17]. Early qualitative

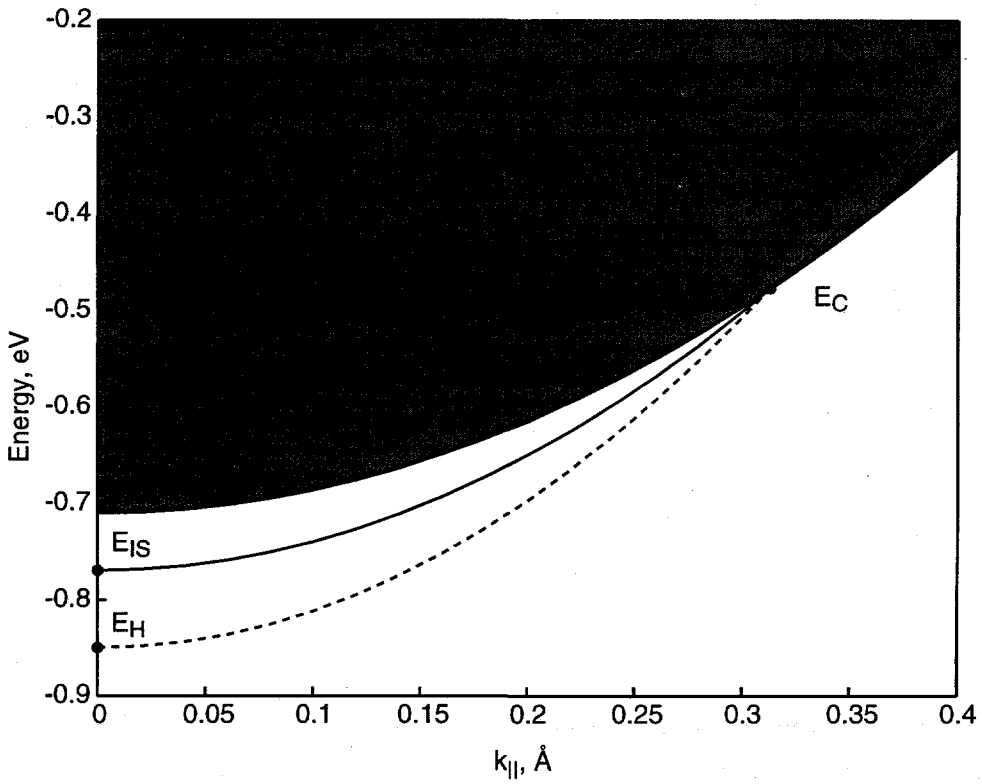

Figure 2.5: Graphical determination of the effective mass of the $n = 1$ image state on Ag(111). The shaded area is the surface projected conduction band. E_H is the Energy of a fictitious hydrogenic image state. E_{IS} is the energy of the image state. E_C is the point where both the image state and the fictitious hydrogenic state cross the conduction band edge.

arguments about the lifetimes of image states were based on the properties of the orbit of an electron in an image potential well. The round-trip time of an electron of quantum number n in a Coulomb well increases as n^3. Assuming that decay is via tunneling into the metal, the lifetime depends on the attempt rate or round trip time. Multiple derivations yielding $\tau \propto n^3$ are provided in a review article [19]. The first quantitative theoretical calculations for the lifetime of image state electrons were provided by Echenique and coworkers [69]. The calculations employed the self-energy formalism in which the lifetime is related to the imaginary portion of the complex self-energy. Schoenlein and coworkers [70] provided the first direct measurements of the lifetimes of image states on metal surfaces using transient two photon photoemission spectroscopy with femtosecond pulses. Their results were in agreement with the earlier predictions. Schuppler and coworkers [71] used high-resolution two-photon photoemission spectroscopy to determine the linewidths of image states which may in some cases be related to the lifetimes.

An empirical approach to calculating image state lifetimes has developed in which the lifetime is related to the penetration of the image state wavefunction into the substrate. The penetration p is defined as the probability density in the bulk [69, 72–74],

$$p = \int_{-\infty}^{0} \psi^* \psi dz. \tag{2.31}$$

The lifetime broadening Γ of the image state is related to the linewidth of the bulk crystal conduction band $\Gamma_b(E)$ by

$$p \cdot \Gamma_b(E). \tag{2.32}$$

The value of Γ_b is approximated by the expression

$$\Gamma_b(E) = a(E - E_F), \tag{2.33}$$

where a depends on the material [75]. The expression in Equation 2.33 has been shown to hold for the range of 5 to 50 eV for several transition metals, based on photoemission and inverse photoemission linewidth data. For Ni, Cu, and Ag a fit to the inverse photoemission data yields $a = 0.13$.

The various decay paths for image state electrons involve excitations of quasiparticles or quasiparticle pairs in the substrate. For most metals, the primary decay pathway for image state electrons is via Auger processes in which the image state electron transfers its energy to an electron in the bulk, generating an electron-hole pair [69]. Additionally, energy can be transferred to surface plasmons and phonons.

In addition to decay channels in which the final state is a bulk state, relaxation can occur in which either intermediate states or final states are image or surface states. Image electrons of nonzero parallel momentum may decay into image states of lower parallel momentum, a process called momentum relaxation or intraband relaxation. Image electrons may also decay to image and surface states of lower quantum number. It has been estimated that 90% of the linewidth of $n = 2$ states is from decay into $n = 1$ states [76]. Approximately 30% of the linewidth of the $n = 1$ state for Ag(111) is attributable to decay via the $n = 0$ surface state [77].

The rate of decay of image states at metal surfaces in which the decay is via the exchange of energy with quasiparticles can be modeled using the self-energy formalism. In the self-energy formalism, the real part of the complex self-energy corresponds to the energy of the state whereas the imaginary portion corresponds to the lifetime. An advantage of the self-energy formalism is its ability to take into account interactions with various quasiparticles to arbitrary order. The effects of other image states on the lifetime of a given state may be taken into account. Generally, lower order terms which correspond to Auger processes dominate the calculated lifetime.

In the first time-resolved two-photon photoemission measurements of image state lifetimes performed by Schoenlein and Fujimoto [70], a simple exponential decay of image state population was assumed. Recent experiments [38, 42] have explored the possible role of coherence dephasing, in which the kinetics are not described by a simple exponential. Rather, the kinetics are described by a set of coupled differential equations known as the optical Bloch equations [41]. These effects will be discussed in Chapter 4.

2.4 Quantum Well States

Quantum well electronic states are a feature of thin film systems. When an infinite solid is truncated, the continuum of bulk states is replaced with a finite number of discrete electronic states. The spacing and number of quantum well states depend on the number of atomic or molecular layers in the slab. For a very thick layer, the number of states is very large and the energy spacing between states is very small; the electronic properties are essentially indistinguishable from those of an infinite solid. However, for a very thin layer, consisting of 1–20 atomic layers, the number of states decreases and the energy spacing between levels is relatively large. This often results in carrier transport properties (for example, energy gap, mean free path, and carrier lifetime) which differ substantially from those of the bulk. Low temperature electron tunneling experiments on thin metal films were performed in the early 1970's [78–80] in which oscillations in the tunneling current as a function of film thickness and sample bias were observed. The oscillations were attributed to the existence of discrete energy levels in the thin film.

Loly and Pendry [81] proposed the study of thin films as a method to improve band structure determination by photoemission. Peaks in photoemission spectra correspond to a vertical transition between two energy bands. In principle, by measuring the energy of the photoemitted electron for a range of photon energies, the band structure along the surface normal can be mapped out. This ideal is not reached due to fundamental limitations of the photoemission technique. The ability to relate a given feature in a photoemission spectrum to a given point in the Brillouin zone, the momentum of the initial and final state must be well defined. It is well known that while the wave vector along the surface plane $k_{||}$ is conserved during the photoemission process, the perpendicular wave vector $k_{\perp}$ is only partially conserved. As the electron crosses the surface on its way out of the solid, $k_{\perp}$ is not conserved as the electron scatters from the surface barrier. This results in blurring of photoemission features and limits the accuracy of photoemission measurements to approximately 25% of the distance to the Brillouin zone boundary. In practice, this greatly limits the resolution of photoemission except near band edges where the dispersion is flat.

Other final state effects also add to the uncertainty in photoemission measurements. Firstly, the finite lifetime of the hole left behind by the photoemitted electron results in the blurring of the band energies. For hole states near the Fermi level in free-electron-like materials, the lifetime broadening is relatively small compared to the other contributions to the final state linewidth. Also, $k_\perp$ for the electron in the solid is uncertain because of the extinction length of around 5–10 Å. Clearly, it would be advantageous to develop a technique which is not sensitive to the uncertainty in $k_\perp$ in the final state.

The picture changes when one assumes a sample N layers thick. The wavefunction of the film along the surface normal can be written in terms of Bloch waves:

$$\psi(z) = u(z)e^{ikz}. \tag{2.34}$$

Assuming the wavefunction must vanish at the layer boundaries $(0, N)$, the resulting wavefunction along the perpendicular direction is a standing wave of the form $\psi = u(z)\sin k_{jz}z$ where j is a quantum number. In order to vanish at $z = Na$, k_z must satisfy

$$k_{jz} = j\pi/Na. \tag{2.35}$$

The quantum numbers in the plane k_x, k_y remain continuous and reveal the bulk dispersion along the surface parallel. An angle-resolved photoemission experiment on this system will reveal a series of spikes in the spectrum. The uncertainty in k_z no longer affects the spectrum since k_z of the initial state is fixed by the boundary conditions of the thin layer quantum well. Thus the final state limitations are effectively removed, the resolution of the technique is limited in principle only by the hole lifetime. The energies of discrete quantum well states can be related to the bulk band structure: the energies are taken from the spectra and a value of k_{jz} is determined from the thickness Na using Equation 2.35, yielding the dispersion $E(\mathbf{k})$.

Loly and Pendry verified that this technique should work on a real system consisting of overlayers on a substrate by modeling the system using the PEOVER photoemission program, which includes multiple scattering processes, surface effects, and hole lifetime.

This technique was later applied successfully to actual photoemission experiments on metal layers including Ag/Si(111) [82], Pb/Si(111) [83], and Ag/Cu(111) [84]. The technique was also applied to an insulator, Xe [85, 86]. In these systems, thin layers (3–40 Å) were studied. For such thin layers the boundary conditions complicate the simplified picture of Loly and Pendry. The imperfect boundary conditions were taken into account by introducing a quantum defect parameter δ. The resulting expression for k_z is:

$$k_{jz} = (j + \delta)\pi/Na. \tag{2.36}$$

It was advantageous to acquire spectra at a range of coverages in order to have enough data points to simultaneously determine δ and tight binding parameters.

Later, the method was applied to the conduction band using the technique of two photon photoemission. Fischer and Fauster [26] investigated the Au/Pd(111) system. It was possible to observe QW states for this system since the Au conduction band edge is well below the vacuum level, while the Pd(111) substrate gap extends well above the vacuum level. Smith and coworkers [87] derived a formula which yields the wavefunctions and binding energies of both the valence and conduction bands for the case of an NFE overlayer.

2.5 The Photoemission Process

It is useful to discuss briefly some of the fundamental aspects of the interaction of light with metal surfaces. These aspects are relevant to the surface depth of the spectroscopy, selection rules, overall photoyield, and their relation to experimental parameters such as light polarization and the azimuthal angle of the light impinging on the surface. Detailed treatments of the photoemission process are given by Inglesfield [88] and Feder [89]. A treatment of single photon photoemission provides an appropriate basis for the understanding of the two-photon photoemission process since the initial and final states are essentially the same. TPPE differs from PE in that an intermediate state is also involved, and that the photon energies are generally smaller.

Feder divides the photoemission process into five basic steps. The first step is the penetration of the radiation through the surface. The second step is the propagation of the radiation inside the solid. The third step is the excitation of the electron. The fourth step is the propagation of the electron towards the surface. The fifth step is the penetration of the surface into the vacuum. Steps 3 through five comprise the well-known three step model for photoemission [90]. In the fully quantum-mechanical one step model, all of the aspects of the three step model are represented as one concerted step.

Steps one and two primarily relate to the optical properties of metals and how they affect the dependence of the cross-section on the angle and polarization of the incoming light. In a simplified view, the metal can be considered to be a material with a dielectric constant of greater than unity. Some of the light is reflected and some is refracted into the material. In general, s polarized light is more likely to be reflected while p polarized light is more likely to be refracted and later absorbed. If the incoming light is circularly polarized, the refracted beam will contain unequal components of s and p polarized polarization and will thus be elliptically polarized, except when the light is incident normal to the surface. This fact must be taken into account in experiments involving circularly polarized light. The preferred geometry for such experiments is near normal incidence. The reflectance of s polarized light incident on a metal surface is a function which decreases monotonically as the angle with respect to the sample normal increases. For p polarized light incident on a metal surface, the reflectance has a minimum at an angle referred to as the principal angle of incidence [91]. For Ag and a wavelength of 590 nm, the principal angle is approximately 78 degrees. Except at surface normal and grazing incidence, p polarized light is more efficiently absorbed than s polarized light. Assuming that photoyield is proportional to the number of photons absorbed, p polarized light should yield a higher number of photoelectrons than s polarized light. The optimum angle for the incident light is between the principal angles for the wavelengths used.

Steps 4 and 5 of the photoemission process, propagation through the bulk and penetration of the surface barrier, are not very important for surface states, since much of the probability amplitude is outside the substrate. These steps are im-

portant for photoemission, and are responsible for the lack of conservation of $k_\perp$ in photoemission from bulk states.

The absorption of the photon results in the excitation of electrons in the bulk or at the surface. Several detailed descriptions of the excitation process are available [28, 89]. Assuming the variation of the electric field due to the incoming radiation is small compared to the length scale of the atoms in the crystal lattice, the matrix element for excitation is proportional to

$$\langle E_f|\nabla V|E_i\rangle, \tag{2.37}$$

where ∇V is the gradient of the potential and $|E_i\rangle$ and $|E_f\rangle$ are the initial and final electronic states. The nature of the potential gradient ∇V at and near the surface results in two rather different excitation mechanisms. For a hypothetical perfect conductor, no electric fields are allowed inside the metal; ∇V is strictly zero. Even in the electron gas (jellium) picture, the potential inside the metal is constant (except very near the surface) and therefore ∇V is zero. Near the surface, there is a discontinuity in the field in the case of a classical perfect conductor and a smooth variation for the case of a quantum-mechanical electron gas. For these two idealized systems, surface photoemission is the only allowed photoemission process. For the more realistic case of a muffin-tin-like potential inside the metal, ∇V in the bulk is non-vanishing, and excitation within the bulk of the solid may occur. The relative magnitude of the bulk and surface contributions of ∇V depends on many factors, including the wavelength of the incident light, the polarization of the incoming light, the plasmon frequency of the solid, and the symmetry of states $|E\rangle$ and $|E_i\rangle$. It should be noted that when nonlocal effects are considered, the distinction between surface and bulk photoemission is somewhat blurred. The polarization of incident light can be varied to help distinguish between surface and bulk photoemission. Surface photoemission is often enhanced by p polarized light.

Since image states are located a distance away from the metal where there is little electron density, momentum is required to displace an electron from the bulk to the image state. This momentum is largely provided by the surface field ∇V_s, so surface photoexcitation is considered to be the dominant mechanism. However, for

direct excitation involving two bulk energy levels, the bulk field usually dominates the excitation process.

Chapter 3

Experimental

The experiments were performed using a custom ultrafast laser two-photon photoemission spectrometer. Briefly, the spectrometer may be described as follows. An ultrafast laser is used to generate short light pulses. The laser light source is a commercial titanium-sapphire oscillator and regenerative amplifier. Tunability of the laser in the visible wavelength region is achieved by the use of an optical parametric amplifier (OPA). An ultraviolet pulse is produced by second harmonic generation using a BBO crystal. The UV pulse serves as the excitation (pump) pulse in the present experiments. The residual fundamental (visible) pulse is used as the probe pulse. The two pulses are separated using a dichroic mirror. The probe pulse is reflected by a pair of mirrors on a stepper motor-driven translation stage. The position of the stage determines the time delay between pump and probe pulses. The two pulses are recombined using a second dichroic mirror and are focussed collinearly onto the sample. The sample is a Ag(111) crystal mounted in an ultra high vacuum chamber. The pump pulse generates an excited electronic distribution on the surface. The probe pulse photoejects the excited electrons. The energy of the photoejected electrons is determined by time-of-flight.

The experimental apparatus can be roughly divided into three main systems: the ultra-high vacuum chamber and associated hardware and diagnostic equipment, the laser system and associated optics, and the data acquisition electronics, which includes the detection electronics, the computer interface, the control program, and

the mechanical translation stage. The apparatus was constructed for the study of electronic states at interfaces by two photon photoemission. Each component must address its portion of the requirements of a TPPE system, as well as the additional requirements imposed by other parts of the system.

The ultra-high vacuum chamber must provide an environment in which a sample interface can be prepared, characterized, and maintained relatively free of contaminants for the duration of the experiment. The laser system must provide light which is tunable in the energy region required to populate the electronic states of interest. Ideally, the laser should produce pulses of a duration on the order of the lifetime of the excited states of interest or shorter. In the case of image states on clean metal surfaces, the lifetimes are on the order of 10-100 fs. An additional constraint is placed on the pulse width by the relatively short path length of the time-of-flight electron spectrometer, which requires that pulses be shorter than 1 nanosecond for optimal energy resolution. The spectral width of the laser pulses should be on the order of 50 meV or less, in order to resolve the first few members of the image series. The pulse energy should be low to avoid the production of too many electrons per pulse, which leads to broadening and distortion of the electron energy profile. Since single electron counting detection is employed, the number of electrons which reach the detector for a given laser pulse should be one or fewer. A general rule of thumb is that one electron count for every 10 or 20 laser shots yields a relatively accurate spectrum.

The data acquisition system should maximize signal throughput and minimize artifacts and distortion of the spectrum due to limitations of the data acquisition scheme, especially any effects which could affect the linearity of the energy measurement or the amplitude of spectral features. The data acquisition system and methods should also address such problems as long term drift in signal due to fluctuations in laser power. Also, standard procedures and baseline measurements are required to maintain the overall health of the system, rapidly identify and repair faulty components, and ensure repeatability and validity of results. Measurements of laser power (at several critical points in the laser system), pulse profile, spectrum, and shot-to-shot noise are required. The quality of the vacuum in the vacuum chamber, substrate

crystal order and cleanliness, and the purity of sample material introduced into the chamber should be measured. The accuracy and linearity of the time-of-flight spectrometer must be determined for a wide range of operating conditions (sample bias, count rate, number of low energy electrons). This chapter is a description of the features of the apparatus which satisfy the requirements of the experiment, as well as the efforts which have been undertaken to ensure the reliability of the results. Experimental results and interpretation are given in the following chapter.

3.1 The Ultra-High Vacuum Chamber

The ultra-high vacuum (UHV) chamber was built specifically for the purpose of angle-resolved two-photon photoemission. A detailed description along with diagrams of several key components can be found in the dissertation of W. Merry [63]. The bell jar is constructed of type 501 stainless steel, which is resistant to oxidation, is relatively free of materials which outgas, and is bakeable to 150 C. Also, type 501 stainless has a magnetic permeability near unity, which makes it suitable for electron spectroscopy. Type 505 stainless steel bell jars are also available which have the advantage of higher baking temperature, strength, and a magnetic permeability closer to unity. Recently, high magnetic permeability nickel alloy chambers have been developed specifically for applications which require very low magnetic fields. All chamber materials were chosen to be UHV compatible and bakeable to 100-150 C, all breakable seals are conflat type with OFHC (oxygen free, high conductivity) copper gaskets.

The vacuum chamber consists of several subsystems: vacuum pumps, sample manipulator, sample characterization (LEED, Auger, UPS), the time-of-flight spectrometer, gas leak valve, effusion cells, pressure gauges, and a quadrupole mass spectrometer.

3.1.1 Sample Manipulator

The sample manipulator fulfills a variety of functions necessary for the operation of the experiment. It securely holds the sample in place and allows the user to precisely control its position. The manipulator linearly translates the sample along three orthogonal axes. The manipulator may also be rotated to direct the sample to the various ports on the UHV chamber for sample deposition, sputtering, LEED and Auger spectroscopy, and time-of-flight photoelectron spectroscopy. The sample is mounted on a goniometer sector which allows the sample to be rotated with respect to the detector axis of the time-of-flight spectrometer. The goniometer sector allows for rotation of the sample between approximately $-4°$ and $20°$. A useful feature of the goniometer sector is the dial which facilitates the determination of the sample angle. The Ag(111) sample is held by molybdenum clips to the sample holder. A thermocouple is in contact the sample in order to measure sample temperature. The sample holder is a piece of molybdenum which contains tungsten filaments for resistive heating of the sample. The current to the heater is controlled by a Eurotherm temperature controller. The bottom of the sample holder is attached to a flexible copper braid connected to a liquid He cold tip. This arrangement allows the sample to be cooled to approximately 45 K.

3.1.2 Vacuum Pumping System

The ultra high vacuum chamber requires a number of pumps to maintain high vacuum in the range of 1×10^{-11} torr. The most important pump is the ion pump (Perkin-Elmer model TNB-X), which maintains vacuum when the vacuum system is not loaded with sample gas. The pumping capacity of the ion pump is augmented by titanium sublimation pump. When the system is under load, *i.e.*, when a sample gas is introduced into the chamber, the gate valve over the ion pump is closed and the gas is removed using a turbomolecular pump (Edwards model EXT250) which is more efficient than the ion pump for removing large volumes of gas at moderately high vacuum. The turbomolecular pump requires a backing pump for operation. A rotary pump is used as a backing pump. Maintenance of the system includes checking

and changing the oil in the backing pump and periodic replacement or refurbishing of the turbomolecular pump.

3.1.3 LEED and Auger Spectrometer

Low Energy Electron Diffraction (LEED) is useful for determining the structure of the sample surface and adsorbed species. An electron gun is directed at an ordered sample. The elastically diffracted electrons pass though a retarding field grid and onto a phosphor screen where diffraction spots may be viewed. Analysis of the electron diffraction spots can yield the two-dimensional unit cell of the surface or adsorbate layer. LEED spot size can be used as a rough measure of the disorder of a surface or layer.

Auger Electron Spectroscopy is a technique for identifying the chemical species on or near a surface. High energy electrons are directed at the sample. Some of the electrons exchange energy with tightly bound electrons on atoms of the substrate, ejecting the electrons from the parent atoms. One of the remaining electrons drops to the empty low-lying state. The remaining excess energy is taken up by ejecting an additional (secondary) electron. This exchange of energy between electrons is referred to as the Auger effect. The energy spectrum of the secondary or Auger electrons is indicative of the atomic number of the parent atoms.

The low energy electron diffraction apparatus and Auger electron spectrometer are combined in a single unit (a SPECTALEED NG from Omicron Vakuumphysik GmbH). The operation in both modes is controllable by computer. The LEED pattern is viewable through a port window (rear view configuration), which greatly improves the viewable area over forward view LEED, especially in the case of a bulky sample manipulator such as the one currently in use.

3.2 Laser System and Optics

The laser system consists of a self-mode-locked titanium-sapphire oscillator, a titanium-sapphire regenerative amplifier, and an optical parametric amplifier. Both

the oscillator and the regenerative amplifier are optically pumped using a single 22 W CW argon ion laser (Coherent Innova 400). A beam splitter divides the 22 W output into a beam of approximately 8 W which is used to pump the oscillator and a beam of approximately 14 W which is used to pump the regenerative amplifier. The laser system is illustrated in Figure 3.1.

The oscillator (a Coherent model Mira 950-F) is a modelocked ultrafast laser that uses titanium:sapphire as its gain medium. The laser cavity consists of a coaxially pumped titanium-sapphire crystal at the focal point of a pair of concave mirrors, a pair of Brewster prisms for dispersion compensation, a birefringent filter which allows limited tunability of the laser, a variable width slit which helps to improve the stability of the mode-locked pulse train, and an output coupler (a partially reflective mirror). The output of the Mira oscillator is a 76 MHz pulse train of pulses with a width of approximately 200 fs. At the center wavelength of 800 nm, the spectral width of the laser pulse is approximately 9 nm. As configured, the oscillator is tunable from 790 nm to 910 nm. The output power is approximately 1.9 W in CW mode and 1.2 W in modelocked mode. After the beamsplitter the modelocked power is approximately 380 mW.

The amplifier (a Coherent model RegA 9000) is a CW pumped Q-switched titanium-sapphire laser. Prior to the injection of a pulse from the oscillator, an acousto-optic Q-switch interrupts lasing in the cavity for a period, allowing energy to build in the lasing medium. Shortly before injection, the Q switch is turned off. Pulses from the Mira oscillator are directed into the RegA. The input beam passes through a cube polarizer and a Faraday isolator. A single laser pulse is injected into the cavity through an SiO_2 acousto-optic cavity dumper. Both the cavity dumper and Q switch are powered by several watts of radio frequency power provided by a control unit. The timing and phase of the RF pulses are determined by feedback from photodiodes monitoring the injected and ejected pulses. The pulse takes approximately 20-30 round trips in the cavity. The resulting pulse is stretched to approximately 20 ps by the group velocity dispersion of the TeO_2 Q-switch and titanium-sapphire crystal. The cavity dumper then extracts the pulse which returns through the Faraday isolator and is separated from the input beam by a polarizer. The stretched,

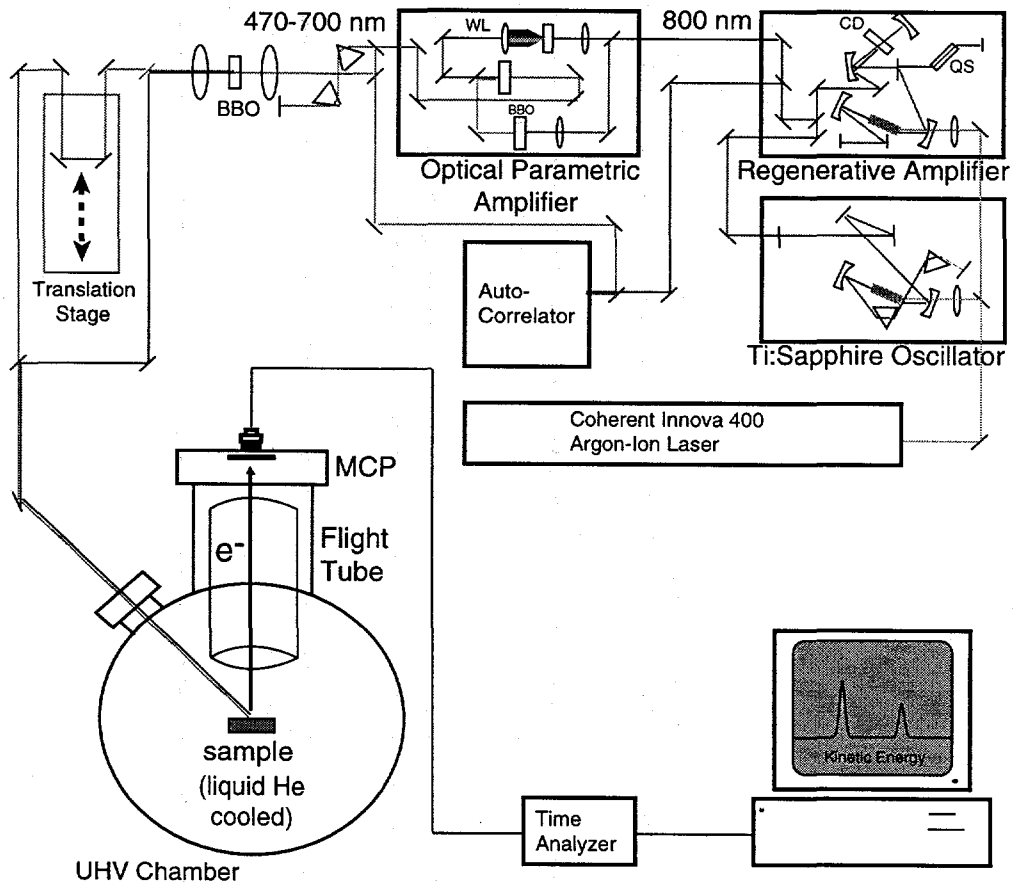

Figure 3.1: Diagram of the major components of the ultrafast laser two photon photoemission spectrometer. The picosecond timing electronics used to determine electron energies are omitted from the figure.

amplified pulse is then compressed using four passes of a single gold-coated holographic grating. The output power is approximately 730 mW (3.7 μJ). The output pulse width is approximately 260 fs.

The tunability of the Mira/RegA combination is not sufficient for the current experiments, which often require light wavelengths between 550 and 750 nm. To add tunability into the visible spectrum, an optical parametric amplifier is used (Coherent model OPA 9400). The output of the RegA 9000 is sent through a 50% beamsplitter. Half of the RegA beam is focussed into a sapphire disc to generate white light continuum. The other half is focussed into a BBO crystal to generate second harmonic. The white light and the second harmonic are focussed collinearly in another BBO crystal where a portion of the continuum is amplified by a non-linear optical process known as parametric amplification. The wavelength of the amplified light is determined by the angle of the BBO crystal. A second pass through the BBO is taken, further amplifying the portion of the continuum amplified in the first pass. The amplified continuum is tunable from approximately 520 nm to 730 nm. At a wavelength of 600 nm, the output power is approximately 30 mW (150 nJ). The chirped output of the OPA is compressed using a prism pair. The resulting pulse width is approximately 80 fs.

In the present experiments, a UV pulse is used as the excite or pump pulse. The UV is generated by focusing the OPA output into a BBO crystal. The UV and residual fundamental are separated using a dichroic mirror. The fundamental takes a single round trip on a mechanical translation stage with a 1 μm step size, corresponding to a precision of 6.6 fs. The fundamental and second harmonic are recombined on a second dichroic mirror and are focussed collinearly on the sample.

3.3 Data Acquisition System

Previously, the experiment used a picosecond laser and the apparatus was used only for measurements of state energies and effective masses. The addition of the femtosecond laser enabled measurements of the dynamics of the electronic states at the metal surface, as lifetimes of such states are on the order of 10-100 fs. The

acquisition of time-resolved TPPE spectra required the addition of a stepper-driven mechanical translation stage and a computer program to scan the stage and acquire spectra at each stage position. The data acquisition electronics and software are central to the experiment and an often overlooked or misunderstood area. Errors in this area are difficult to detect and may render results useless. An understanding of the data acquisition system is required in order to use the system properly and to tune and calibrate the system for optimum accuracy, linearity, and signal rate. Also, future changes to the experiment may require a more complete understanding of the current setup and its limitations. Therefore, the data acquisition system is described in some detail.

The data acquisition system consists of the time-resolved single-electron-counting electronics, the mechanical stepper motor driven stage, the stage controller, and the program which controls the electron-counting electronics and the stage controller.

3.3.1 Amplification, Discrimination, and Timing

The amount of time required for an electron generated in this experiment to traverse the 13 cm flight tube is typically a few hundred nanoseconds. For the desired energy resolution of about 5 to 10 meV, a time resolution of a fraction of a nanosecond is required. To obtain this level of time resolution, care must be taken in the design of the detector, and special electronics are required. The electron detector is a microchannel plate detector (Galileo Electro-Optics model FTD-2003, with 2.5 cm diameter plates). The microchannel plates act as an electron multiplier. A bias of +200 V between the flight tube and the first channel plate accelerates the electrons in the direction of the channel plates. A bias of +2000 V is placed across the channel plates which accelerates the electrons through the channels in the microchannel plates. As the electrons strike the walls of the channels, an electron cascade results which amplifies the signal. Upon exiting the second channel plate, the electron cascade is accelerated by an additional +200 V bias towards the 50 Ω impedance detector anode. At the top of the anode is a copper layer on top of a .5 mm ceramic plate which is connected to a conical aluminum stalk. The conical

form of the anode helps prevent reflections of the signal which lead to ringing in the pulse shape. The ceramic plate decouples the anode from the voltage bias of the copper layer: the anode is A.C. coupled. The anode terminates in a 50 Ω BNC connector which is attached to an ultra high vacuum compatible BNC feedthrough mounted on a conflat type flange.

The amplified pulse has a positive-going hump with a rise time of a fraction of a nanosecond followed by a negative hump followed by some ringing. The pulse height varies substantially from pulse to pulse (the amount of amplification provided by the channel plates varies from point to point on the plate), but the overall pulse shape is reproducible. The pulse is amplified by a factor of 10 by a high bandwidth (1 GHz) amplifier (Philips Scientific model 6954B-10) located near the chamber. The output of the amplifier is connected to a Tennelec model TC454 Quad Constant Fraction Discriminator. The role of the Constant-Fraction Discriminator (CFD) is to turn the complicated pulse from the microchannel plates into a reliable timing pulse with a jitter of less than 100 ps. A threshold discriminator (as opposed to a constant fraction discriminator) generates a timing pulse whenever the input pulse reaches a certain voltage threshold. However, since the input pulses have a variable peak height, some timing jitter would result from threshold discrimination. Also, a threshold discriminator may not be able to differentiate between the fast MCP pulses and slow line noise. A CFD possesses additional circuitry to circumvent these shortcomings. A CFD splits off a fraction of the incoming pulse, inverts it, delays it, and adds it to the original pulse. This eliminates slow pulses, since only a pulse with a rise time on the order of the fixed time delay between fractions will have appreciable amplitude. The resulting pulse is then sent to the threshold discriminator portion of the CFD. The threshold discriminator triggers a zero-crossing detector. When the pulse crosses zero, a timing out pulse is generated. The timing out pulse relies primarily on the rise characteristics of the incoming pulse, and not the amplitude. The threshold and zero crossing voltages can be set with trimmer potentiometers and measured with a voltmeter. The constant fraction delay is specified by a short length of cable. In general, for best linear response, the discriminator levels should be readjusted whenever it is suspected that changes in the timing characteristics or

amplitudes of MCP pulses have occurred, for example, when replacing the amplifier, replacing the channel plates, changing the MCP bias, and periodically as the channel plates age. Improper adjustment of the CFD can lead to occasional triggering from the ring instead of the main pulse (this can give rise to slightly twinned, broadened peaks), low count rate (if the threshold is set too high), a high number of dark counts (if the threshold is set too low), biasing towards two electron pile up events, and poor time resolution. One way to test of the adjustment of the discrimination electronics is to increase the channel plate voltage by 100 volts or so in order to change the mean amplitude of the electron pulses and measure the change in count rate. If the discrimination electronics are properly adjusted and the channel plates are in working order, there should be a minimal impact on the count rate and no impact on the spectrum.

Currently, there are improved constant fraction discriminators on the market. The latest discriminators allow for more flexibility in the adjustment of the size of the fraction and the fraction delay. The other timing pulse is the photodiode output. Since the photodiode output has a much lower variation in amplitude (typically 5 percent), a threshold discriminator is used. The photodiode output acts as the "start" pulse and the processed output of the MCP is provides a "stop" pulse. The time between pulses is (approximately) the flight time of the photoemitted electron.

3.3.2 Time to Digital Conversion

Both timing pulses are sent to the TAC, Time to Amplitude Converter (Canberra Model 2043 Time Analyzer). The TAC generates a pulse whose voltage is proportional to the time between start (photodiode) and stop (MCP) pulses. The TAC voltage is digitized by the MultiChannel Buffer (MCB), which is an EG&G Ortec Model 918 ADCAM. The MCB uses an efficient buffering scheme. Instead of passing each digitized value along to the computer, it simply adds a count to an address in the internal buffer memory corresponding to the digitized value. The result is a histogram of electron energies. Since the MCB has a 13-bit ADC (Analog to Digital Converter), the buffer memory has 2^{13} or 8192 addresses, or "bins". Each bin has

a capacity of 31 bits or $2^{31} \simeq 2 \times 10^9$ counts. An extra bit is reserved for marking regions of interest. After a scan with a duration of 15 s to several minutes, the resulting histogram is read using a dual port memory interface card in the the PC. This buffering scheme avoids a potential bottleneck in the data acquisition process and frees the PC to perform other tasks while the MCB is collecting and buffering the data. A typical data rate is 10 kHz. Each time conversion takes approximately 12 μs, which results in a "dead time" during which subsequent events are ignored. Since laser pulses arrive every 5 μs, two potential electron counting events are ignored, resulting in an effective dead time of 10 μs per recorded event. For a 10 kHz acquisition rate, the dead time comprises approximately 10% of the total acquisition time. The model 918 MCB keeps track of dead time by adding 12 μs to a dead time counter for each data acquisition event. Unfortunately, this results in a 20% overestimation of the dead time. This error is corrected in the data analysis software. It should be noted that newer ADC devices have a reset time of less than 5 μs, which for the current experiment would eliminate dead time in the digitization step. There are also picosecond time analyzers that can handle multiple stop pulses per start pulse, which increases the usable data rate. Newer time analyzers often have built-in ADC units, so a separate ADC is not necessary.

3.3.3 Linearity, Count Rate, and Noise

Since this is a single-electron-counting system, the signal is only linear with count rate when there are one or fewer electrons per laser shot. Non-linearity caused by high count rates can be easily observed in the current system. This non-linearity can make it difficult to compare peak heights (either between two neighboring peaks at a given femtosecond time delay or for one peak at different time delays). Also it can flatten the top of very tall, narrow peaks, making measurements of lineshape difficult. It can also cause asymmetry in a measured peak. In addition, high count rates can often be a sign that space charge broadening is occurring, i.e., that the electron flux is high enough that a measurable broadening and shifting of electron peaks occurs through electron-electron repulsion in the free space of the flight tube.

Space charge broadening should not be confused with *dielectric charging*, which is the accumulation of charge on dielectric components near the sample or flight tube. The effect of dielectric charging is less predictable than that of space charge broadening.

For a laser repetition rate of 200 kHz, one would assume that a count rate of 10 kHz would mean that the probability of any one laser shot producing an electron would be 1/20 or 5%. The chance of two electrons being emitted would be 1/400 or 0.25%. Thus 5% of the signal (not 0.25%) would be lost due to two electrons being emitted per laser shot. However, this assumes a constant probability of emitting an electron per laser shot. In reality, there is an appreciable amount of noise in the laser, approximately 5 or 10%. Assuming that the probability of emitting an electron is proportional to the laser power to the third power, this means that for pulses that have 10% more energy, the probability of emitting an electron is 33% larger than that of a pulse of average energy. Thus, pulse-to-pulse fluctuations in the laser pulse energy can significantly increase the probability of more than one electron reaching the detector per shot, reducing the usable count rate. It should not be assumed that the linearity of the detection electronics remains the same day-to-day. The linearity of the detection electronics should be verified on a regular basis, by comparing spectra and decay traces for a range of count rates (for example, by using a neutral density filter to attenuate the laser beam).

In addition to the shot-to-shot noise referred to in the previous paragraph, the laser power can drift over the course of a few minutes or a few hours. This laser drift can have a devastating effect on the accuracy of kinetics traces. To minimize the effect of the laser drift, scan times should be as short as possible. This can be achieved either by reducing the number of points (stage positions) in a scan, or by reducing the amount of time a spectrum is acquired at a given stage position. A lower limit is placed on the number of stage positions by the fact that a large number of points along the decay trace are required in order to gain good statistics on the time constants extracted from the data. A lower limit on the data acquisition time per stage position is placed by the fact that it takes a few seconds to set up acquisition at each stage position. The bottleneck in this case is the amount of time required to transfer buffered data from the MCB and to clear the MCB memory in preparation

for a new scan. Currently, the spectrum is acquired for approximately 15 seconds at each stage position, and the number of steps in a scan is between 40 and 200. Generally, six complete scans are taken for a given set of experimental conditions. The overall amplitudes of each scan in a set are compared in order to check for the effects of laser power drift.

3.3.4 The Data Acquisition Program

The data acquisition program is responsible for controlling the electron counting electronics and the stepper motor-driven translation stage as well as generating a data file. The data acquisition program is actually a MATLAB script called `TRTPPE.M` running in DOS. MATLAB was chosen because the system's users were familiar with MATLAB syntax, the syntax is terse and readable, and the MATLAB interpreter environment is ideal for rapid code development and testing.

The initialization of the data acquisition script involves essentially three steps:

1. Define the number and spacing of steps in the scan.
2. Query the user for number of scans and scan direction.
3. Move the stage to the start position.

The main loop contains three essential steps:

1. Calculate the stage position and move the stage.
2. Clear the MCB and start acquiring a spectrum, wait.
3. Read the contents of the MCB, store to a file.

Since the version of MATLAB in use has no facility for interfacing with data acquisition hardware, the script makes use of three DOS programs written in C to control the stage, control the MCB, and write the contents of the MCB to a file. These three programs are called `STAGE`, `MCBACQ`, and `MCBMAT`, respectively. MATLAB provides a mechanism for executing small DOS programs from within a MATLAB script. The source code for the MATLAB script and the C programs is in Appendix A.

The stage controller is a Klinger Scientific model CC1.1. It drives a mechanical translation stage with a step size of 1 μm driven by a stepper motor. The round trip time difference for the laser pulse for a single step is 6.7 fs. The stage controller is interfaced to the computer using the IEEE-488 (GPIB) interface bus and a National Instruments AT-GPIB interface card. The GPIB bus is a medium bandwidth (approximately 100 kilobyte/sec) bus capable of controlling 15 instruments. The stage is controlled by issuing simple text commands across the GPIB bus. In the software, the commands are arguments to GPIB functions in a function library which is supplied with the interface card. The `STAGE` program performs the communication with the stage controller. The program accepts two arguments, a direction and a position. The appropriate arguments are generated by the `TRTPPE.M` script.

The `MCBACQ` program issues commands to the Ortec model 918 ADCAM multichannel buffer. The connection to the model 918 to the computer is through a special purpose interface card. The card possesses a mailbox I/O interface through which commands are issued to the 918 by writing to a specific I/O address. C functions for the low-level I/O were provided by EG&G Ortec. The example programs in the manual are incorrect. The `MCBACQ` program clears the buffer memory and acquires a spectrum for a fixed amount of time, typically 15 s.

The `MCBMAT` program is used to save the contents of the 918 buffer memory. The memory is accessible through the interface card using a dual-port memory interface. The contents of the 918 data buffer are accessible on the PC in the `0xD000` memory page.

A full spectrum is generated at each stage position. Depending on the number of points along the time axis required for a given experiment, between 40 and 200 spectra are generated for a given scan. Along with each scan, a file is saved which contains information about the number and spacing of points along the time axis as well as a text comment. The data are saved in platform-independent MATLAB format. The MATLAB format is readable by a number of programs including Octave, a freely-redistributable MATLAB clone. Information on the file format is available in the MATLAB documentation.

Chapter 4

Results and Discussion

In this section the results of a systematic series of experiments and theoretical investigations designed to identify and characterize the important physics relating to electronic states and dynamics at molecular adsorbate interfaces are presented. Two photon photoemission is employed to determine the energies and population kinetics of excited electronic states at molecular adsorbate interfaces. The adsorbate materials studied theoretically and experimentally include alkali metals, alkanes and rare gases. Theoretical models were implemented in an attempt to relate experimental results to well-known physical parameters and in order to test assumptions about the role of the substrate and overlayer electronic structure and the polarizability of the interface and in order to develop and refine a coherent physical picture of the systems of interest.

Because of the complexity of the electronic structure of overlayer systems, it is difficult to separate the relative contributions of the substrate and overlayer and the physical parameters which describe them. This is the motivation for studying a series of similar, but slightly different materials, such as alkanes and rare gases. The alkane data is contained in other theses, so only the rare gas and alkali metal work are presented here. In addition to varying the material under study, the coverage is also varied, in an attempt to determine the impact of layer thickness on quantum confinement and in order to monitor the development of 3D band structure.

4.1 Surface and Image States of an Alkali Layer on Cu(111)

In this section a theoretical model is developed and an analytic solution is derived for the case of an ultrathin alkali metal layer (specifically, Na) on a metal substrate. Portions of this work were adapted from a paper by McNeill and Harris [92]. The author performed a series of experiments on K/Ag(111) in order to further test the model and improve our understanding of image and surface states in the presence of alkali metal layers. However, problems with the TPPE spectrometer cast doubt on the validity of the results, and it was decided not to include them in this thesis. The model described in this section was developed in an attempt to address several important issues relating to the electronic structure of excited electronic states at interfaces. These issues include the delocalization and resulting dispersion or effective mass of interface states or bands, the interplay between effects induced by the image barrier, interface potential, and substrate band structure, and the applicability of multiple reflection theory [17] to adsorbate systems. A single atomic layer of alkali metal on a metal substrate was chosen for these calculations since it is more straightforward to model than other cases, such as insulator overlayers, as the metal overlayer does not affect the image potential in the vacuum and the electronic structure of the overlayer itself is simple (free-electron-like).

The fundamental effects of adsorbates on the electronic structure of surfaces have been identified by experiment and theory. The presence of adsorbates on a metal surface has been shown experimentally to shift the binding energy of image states [93–96], give rise to adsorbate-derived states [97–99], or change the dispersion of the image states [95, 100, 101]. More recently, laser-induced desorption of alkali metal atoms from metal surfaces was observed and monitored on the femtosecond timescale [52]. An approximate phase shift model for image and surface states for the case of an alkali metal layer deposited on a noble metal substrate was developed by Lindgren and Walldén [102]. Their model agreed with image state binding energies determined by inverse photoemission. However, the results of later

studies of Na/Cu(111) and K/Cu(111) using high-resolution two-photon photoemission [101, 103] conflict with the predictions of that model. The approximate nature of that model and the development of experimental methods with resolution sufficient to provide a good test of theory warrants the re-investigation of the phase shift model for the case of alkali overlayers.

4.1.1 Multiple Reflection Theory for a Metal Adlayer

An extension of the phase shift approach to multiple reflection theory was proposed by Lindgren and Walldén [102] for the case of alkali metal layers adsorbed on a noble metal substrate. In their approach, the overlayer is represented as an additional phase shift of $2\phi_d$, where $\phi_d = d\sqrt{2m_e(E-U)/\hbar^2}$ and E is the energy of the electron, U is the potential in the overlayer, and d is the thickness of the overlayer. The bound state condition is then $\phi_c + \phi_b + 2\phi_d = 2\pi n$. However, a careful inspection of the underlying wavefunction solution reveals that wavefunction matching is not preserved for the above bound state condition. While this expression constitutes an approximate solution to the problem, it is possible to solve the problem exactly for a more general potential (potential illustrated in Figure 4.1). In the present approach, the effect of an alkali overlayer is explicitly incorporated into the expression for ϕ_c by applying the appropriate matching conditions at the boundaries between the substrate and overlayer regions, thus ensuring that the bound state energy given by multiple reflection theory corresponds to a continuous wave function. The results of the model are then compared to the binding energy and dispersion results of Fischer [101, 103].

The present phase shift model is a variant on the well-known particle in a 1-D box model. In this case, the flat box potential represents the layer. On one side, the box is bounded by a periodic potential representing the substrate, while on the other side the box is bounded by the metal image potential. Bound states are determined by applying matching conditions at the edges of the box. The two-band nearly- free-electron model [5,61] is used to describe the electronic wave function of the substrate. According to the model, the wave function for an electron in the band gap is of the

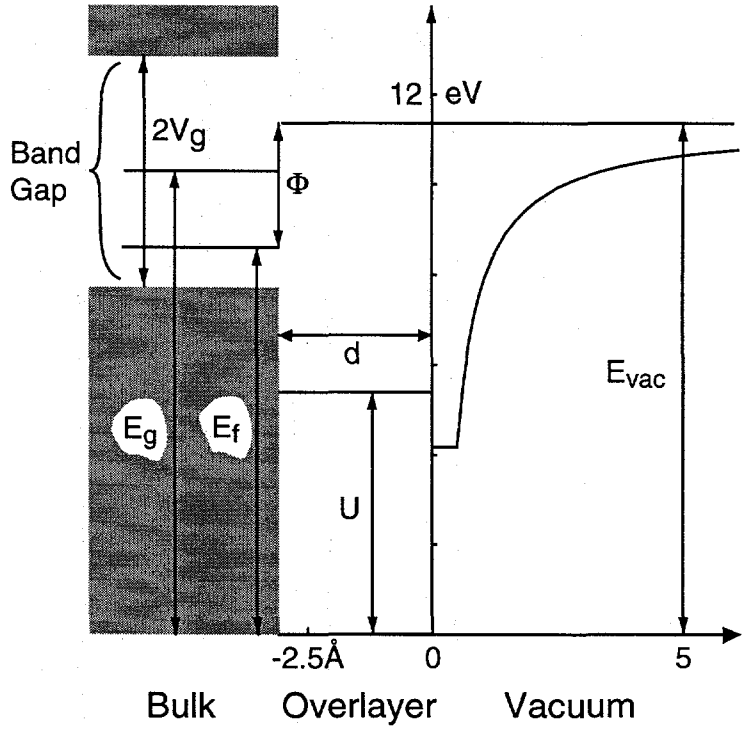

Figure 4.1: The model involves a metal substrate with a work function Φ, band gap parameters E_g, V_g, and wavevector g, an overlayer represented by a flat potential barrier of height U and thickness d, and a Coulomb potential in the vacuum.

form

$$\psi_c = Ke^{qz}\cos(pz+\delta), \tag{4.1}$$

where p the real part of the electron's wave vector, q the imaginary part of the wave vector, and δ the phase parameter are related to the reciprocal lattice vector g and the band gap parameters E_g and V_g which correspond to the position and width of the gap, respectively.

In the overlayer region, the potential is approximated by a square well. Solutions in this region are in general a linear combination of incoming and outgoing plane waves:

$$\psi_l = Ae^{ik_l z} + Be^{-ik_l z}, \tag{4.2}$$

where $k_l = \sqrt{2m(E-U)/\hbar^2}$, E is the energy of the electronic state, U is the potential of the overlayer, and m is the effective mass for the overlayer band. The origin of the z axis is set to the adlayer/vacuum boundary in this derivation. The wave function in the adlayer at $z=-d$, where d is the thickness of the overlayer, is then matched to solutions in the bulk crystal at half the inter atomic spacing outside the bulk crystal along the z direction (half-layer termination [61] is assumed). The matching condition is satisfied by setting the logarithmic derivatives of the wavefunction solutions on either side of $z=-d$ to be equal, thus determining the coefficients A and B. The application of wavefunction matching results in a single expression which treats the crystal and adlayer as a unit for the purpose of calculating phase shifts. In order to determine the phase shift, the solution in the adlayer is matched at the adlayer/vacuum boundary ($z=0$) to a plane wave of the form

$$\psi = e^{-i\kappa z} + r_c e^{i\phi_c} e^{i\kappa z}, \tag{4.3}$$

where $\kappa = \sqrt{2mE/\hbar^2}$. The two sets of matching conditions give rise to a system of equations which can be simplified to yield an expression for the total phase shift in the crystal and overlayer regions:

$$\tan\frac{\phi_c}{2} = \frac{k_l}{\kappa}\tan\left(k_l d + \tan^{-1}\left(\frac{-q}{k_l} + \frac{p}{k_l}\tan(pa/2+\delta)\right)\right). \tag{4.4}$$

As in previous calculations of image state binding energies for clean metal surfaces [19], the potential in the vacuum region is approximated by a Coulomb potential

with a cutoff. The solutions to the time-independent Schrödinger equation for the Coulomb potential are confluent hypergeometric functions [55]. The solution in the vacuum region which matches the solution in the cutoff region and vanishes at infinity is the irregular Whittaker function [54], $W_{\lambda,\mu}(\rho)$, where $\mu = 1/2$, $\lambda = Z\sqrt{2E}$, $\rho = 2z\sqrt{2E}$, and $Z = 1/4$ for the case of a conducting substrate, and E and z are in atomic units. The phase shift for a unit of flux traveling from the origin towards the Coulomb barrier is

$$\phi_b = 2k_c z_0 + 2\tan^{-1}\left(\frac{2\sqrt{2E}}{k_c}\frac{W'_{\lambda,\mu}(\rho_0)}{W_{\lambda,\mu}(\rho_0)}\right), \tag{4.5}$$

where $W'_{\lambda,\mu}(\rho_0)$ is the derivative with respect to ρ evaluated at ρ_0 , k_c is the wave vector in the cutoff region, $\rho_0 = 2z_0\sqrt{2E}$, and z_0 is the cutoff distance. The values of $W_{\lambda,\mu}(\rho_0)$ were calculated using the generalized hypergeometric function `HyperGeometricU` in *Mathematica* [104]. As in the case of multiple reflection theory, bound states occur where the round trip phase shift is an integer multiple of 2π. The zero of energy in the matching was set set such that $k_c = \kappa$. This simplifies the expression for ϕ_b but does not affect calculated binding energies. Since the expression for the phase shift is derived using the proper matching conditions, the wave functions derived where the bound state condition is met are continuous, as shown in Figure 4.2. Since the bound state condition does not uniquely define the quantum number n, we define n according to the behavior of the wave function in the vacuum region, i.e., a wave function with an exponential tail in the vacuum is an $n = 0$ state, a wave function similar to a hydrogenic $n = 1$ state in the vacuum is an $n = 1$ state, etc.

Whereas Fischer and coworkers [101] concluded that no set of parameters in the expression of Lindgren and Walldén [102] fit the observed binding energies, the present model fit the observed binding energies to nearly within experimental error. The best fit resulted when the Na potential was set to 4.25 eV below vacuum and the thickness of the layer was set to 4 Å. The values of E_g, V_g, and the cutoff distance in the vacuum z_{im} were taken from Echenique and Pendry [19]. The work function of Na/Cu(111), 2.69 eV, was taken from Lindgren and Walldén [102]. The effective mass for the overlayer was set to that of a free electron (the results could perhaps be

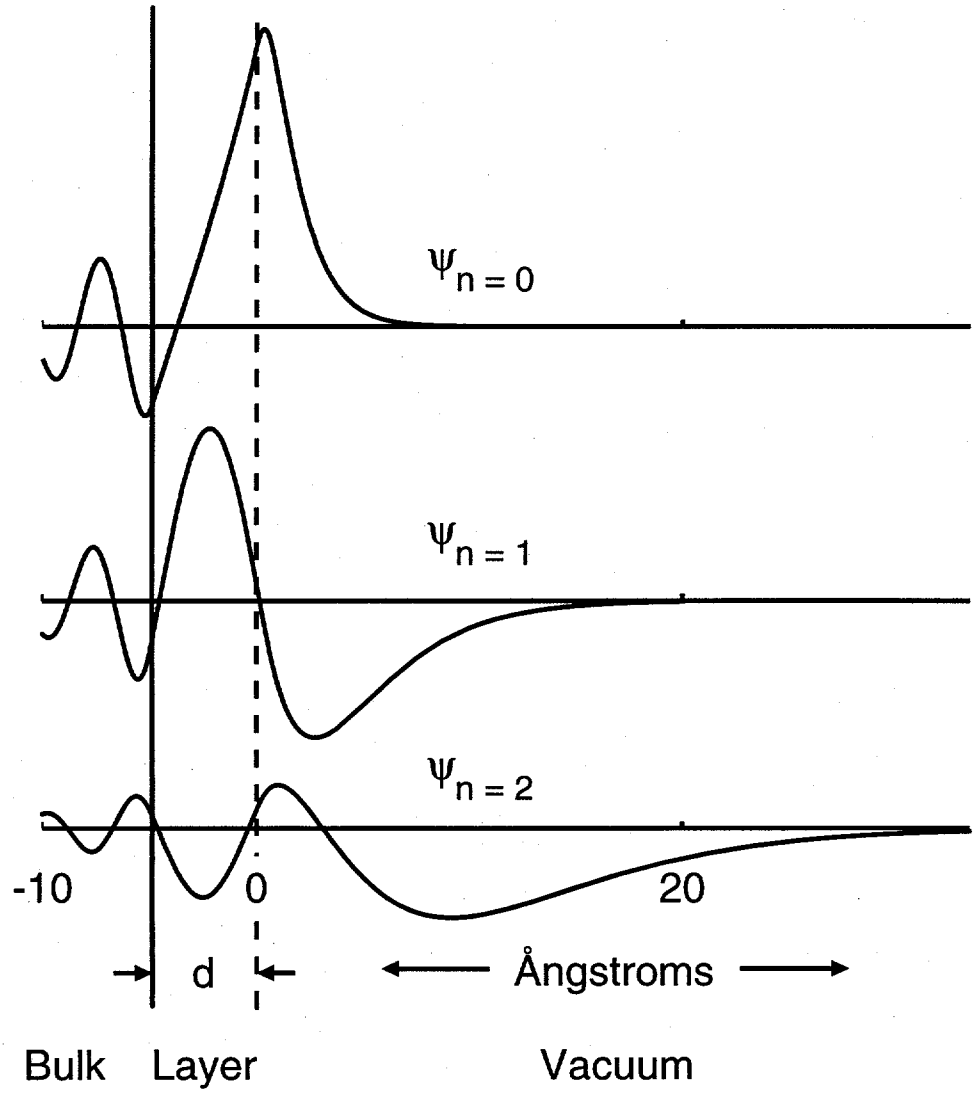

Figure 4.2: Wave functions for the surface state ($n = 0$) and first two image states ($n = 1, 2$) for a model potential for Na/Cu(111).

improved by employing the effective mass of the appropriate band of bulk Na). The best fit parameters give binding energies of 3.0 and .72 eV for the $n = 0$ and $n = 1$ states, respectively. These values compare well with the experimental values of 2.88 and 0.72 eV.

One difference between the present model and previous attempts is that the phase shift for the overlayer is calculated using a solution which is properly matched at the layer/substrate boundary, as opposed to assuming an additive phase shift $\phi_l = k_l d$. It is easy to illustrate that in some cases the assumption of an additive phase shift will yield results which are clearly incorrect. If one assumes a high potential barrier in the layer, the electron is excluded from the layer, the phase shift at the layer is π, and the result is a hydrogenic image series. However, if one assumes the phase shift of the substrate is additive and is, for example, $\pi/2$, the model will predict that the substrate will result in a substantial deviation from hydrogenic behavior. This result doesn't make sense given the fact that the electron is effectively excluded from the substrate and therefore the substrate shouldn't affect the binding energies. The application of matching conditions at the substrate/layer boundary as in the present model removes this apparent contradiction. The expression of Equation 4.4 possesses the correct behavior ($\phi_c = \pi$) for the limiting case of an infinite potential barrier in the layer.

Another important difference between the two models is the use of a cutoff parameter z_{im} for the image potential in the vacuum in the present model instead of extending the overlayer potential to the point where it intersects with the image potential as in the previous model. The presence of the cutoff implies that in most cases, the deepest part of the potential well is in the vacuum region outside the layer instead of inside the layer. In other words, there is a small potential barrier for an electron impinging on the layer. This barrier affects the energies of low-lying states which possess a maximum in the probability amplitude near the layer/vacuum interface. It is worth noting that the present model potential may also be extended to the case of thin insulator layers, as is shown later. The previous model fails for insulator layers where the layer potential is above the vacuum level, since the layer potential may not intersect the image potential as required by the model.

4.1.2 Effective Mass

The method of Giesen et al. [32] for estimating the effective mass of image state and surface state electrons within the multiple reflection theory formalism has been successful in accounting for the observed effective mass of image and surface states on clean surfaces but not for adsorbate covered surfaces. This method was described in Section 2.3.4. The method relies on the value of the phase shift at a bulk band edge, either π (top of gap, for the case of a Shockley-inverted band gap) or zero (bottom of the gap for a Shockley-inverted band gap).

A straightforward way to apply this model to the case of an adsorbate layer is to assume that the primary effect of the adsorbate layer on the surface electronic structure is the adsorption-induced work function change. For the case of Na/Cu(111), the work function lowering induced by the adsorbate places the image state near the middle of the gap. Assuming this to be the only effect of the adsorbate layer, the model predicts an effective mass of $m^* \approx 1m_e$ for the $n = 1$ image state. The measured effective mass is 1.3 m_e [101], which indicates that work function lowering alone does not explain the Na/Cu(111) effective mass.

It is apparent that, as well as causing a work function change, the adlayer has an additional effect on the dispersion of the image state electron. Therefore a method which explicitly incorporates adlayer effects into effective mass calculations is required. In this section, the theory of the previous section for binding energies of a simple overlayer is extended to determine a theoretical effective mass.

An approximate way to calculate effective mass using the 1-D model potential is by including the momentum dependence in the parameters which describe the band gap. If m^*_{ube} is the reduced effective mass of the upper band edge and m^*_{lbe} is the reduced effective mass of the lower band edge, then since E_g corresponds to the average of the upper and lower bend edges, its dependence on $k_{||}$ is given by

$$E_g(k_{||}) = E_g(0) + \frac{\hbar^2 k_{||}^2}{2m_e} \frac{1}{m^*_{ave}}, \tag{4.6}$$

where m^*_{ave} is the average of the masses of the upper and lower band edges. Since $2V_g$ is the difference between the upper and lower band edges, its dependence on $k_{||}$

is given by

$$V_g(k_{||}) = V_g(0) + \frac{\hbar^2 k_{||}^2}{4m_e}\left(\frac{1}{m^*_{ube}} - \frac{1}{m^*_{lbe}}\right). \tag{4.7}$$

The dispersion in the overlayer can be approximated by adding an effective mass term to the expression for the perpendicular component of kinetic energy in the overlayer,

$$\text{K.E.} = E - U_0 - \hbar^2 k_{||}^2 / 2m_l^*, \tag{4.8}$$

where m_l^* is the effective mass in the overlayer and U_0 is the overlayer potential.

For the clean surface, the curve corresponding to $\phi_c = \pi$ is the upper band edge. The addition of an overlayer will change the position and dispersion of the curve corresponding to $\phi_c = \pi$. The new position and dispersion of the $\phi_c = \pi$ band can be found by inserting a value for $k_{||}$ in equations (7) and (8) to determine the local values of E_g and V_g, which are in turn used to determine the parameters p, q, and δ, related to the crystal phase shift by Equation 4.4. The curve is finally determined by fitting a parabola between points corresponding to $\phi_c = \pi$ for several values of $k_{||}$. Figure 4.3 compares the upper band edge of Cu(111) and the curve corresponding to a crystal phase shift of π in the presence of an overlayer of Na. Dispersion of the overlayer band was not taken into account–a flat dispersion in the overlayer was assumed. Note that there is a shift of almost 2 eV and a flatter dispersion in the $\phi_c = \pi$ curve. The effective mass of the image state is determined by the geometric construction of Giesen et al.

An important question is how to treat the dispersion in the overlayer. One could assume a flat dispersion in the overlayer which implies that the kinetic energy in the overlayer would be independent of $k_{||}$. For the case of Na/Cu(111) this assumption leads to a result of $m^*/m_e = 1.8$ for the $n = 1$ state. If one assumes a free-electron dispersion in the overlayer, the resulting effective mass for the $n = 1$ state is $m^* = 1.1m_e$. A comparison of these results to the experimental value [101] of $m^*/m_e = 1.3$ suggests that the effective mass m_l^* associated with the Na layer is somewhat greater than that of a free electron. A quantitative analysis of the relative influence of the effective mass of the overlayer material and the substrate material on the image state effective mass within the assumptions of this model was not performed but would be

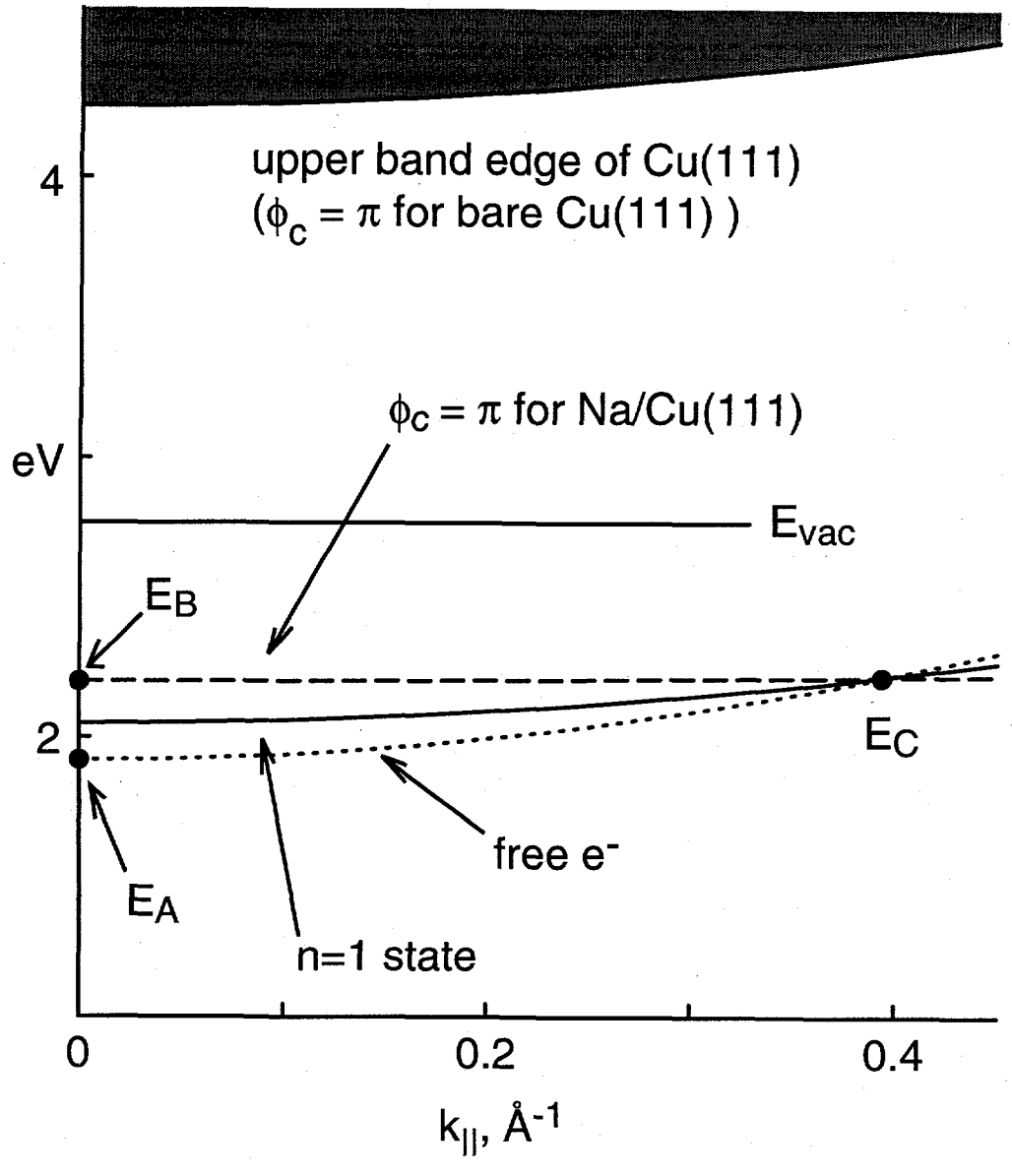

Figure 4.3: The effective mass associated with an image state is determined by forcing the image state parabola to cross the $\phi_c = \pi$ curve at the same point (E_C) where the free electron band crosses the $\phi_c = \pi$ band. For the case of a bare metal surface, the upper band edge and the $\phi_c = \pi$ band are one and the same. The presence of an adlayer changes the position and curvature of the $\phi_c = \pi$ band.

useful for future studies of similar systems.

4.1.3 Conclusions

Within the assumptions of the two-band nearly-free-electron model, a flat adlayer potential, and a Coulomb potential with cutoff, an exact analytic solution to the problem of image states on alkali metal-covered surfaces was derived within the framework of multiple reflection theory. The expression for the total phase shift yields binding energies in good agreement with experimental binding energies of image and surface states on Na/Cu(111). A simple theory which accounts for the effective mass values of image and surface states was modified for the case of a metal overlayer. Effective mass calculations for Na/Cu(111) suggest that the electron in the overlayer is somewhat heavier than that of a free electron and qualitatively account for the discrepancy between experimental results and those obtained from simple work function lowering arguments. The principal difference between this model and previous models is the addition of a cutoff parameter which implies a potential jump at the layer side of the layer/vacuum interface. It can be concluded that the presence of this barrier is important in determining the energies of low-lying electronic states. The approach taken here, matching the wave functions in the overlayer to wave functions in the bulk and in the vacuum, is general in principle and may be applied to more complicated cases, such as dielectric layers, which are discussed later in this chapter.

4.2 Ultrafast Kinetics of Image States on Clean Ag(111)

This section illustrates the analysis an interpretation of ultrafast kinetics data presented in later sections. The ultrafast kinetics for the $n = 1$ image state on the Ag(111) surface were determined using the vacuum chamber and Titanium:Sapphire laser described in Chapter 3. The time delay between pump and probe pulses is determined by the position of the mechanical translation stage. The time-of-flight

electron energy analyzer records a complete spectrum for each stage position. The result is a three dimensional data set where the axes are time, energy, and electron counts. Typical results for the $n = 0$ and $n = 1$ states on clean Ag(111) at laser wavelengths of 295 nm for the pump and 590 nm for the probe are shown in Figure 4.4. The $n = 0$ state feature is due to a non-resonant two photon excitation through a virtual intermediate state.

Kinetics traces are generated for a given feature by plotting the signal as a function of time delay. The signal in this case is the number of electron counts associated with a given spectral feature. In the case where the functional form of the line shape of the spectral feature is known, the signal may be determined by numerical fitting. For other cases, it is more practical to approximate the integrated signal by summing the electron counts over a small range of energy near the peak maximum. Figure 4.5 contains the kinetic traces for the $n = 0$ and $n = 1$ states taken from the spectra shown in Figure 4.4. While the two traces are similar in shape, there is a slight asymmetry in the $n = 1$ peak and the maximum of the trace occurs at approximately 35 femtoseconds after the maximum of the $n = 0$ trace. Since the $n = 0$ state is due to a non-resonant two photon absorption, the kinetics trace represents the instrument response function. The instrument response function is assumed to be Gaussian in shape. The $n = 1$ state is modeled by convolving the instrument response function with an exponential rise and decay function. The exponential rise and decay function is the solution of the rate equations for a system in which initial excitation from the ground state into the upper state is followed by decay into the lower state which is the state of interest. The fit corresponds to a rise and decay of 20 fs and 26 fs.

The functional form for a single exponential decay is

$$n(t) = Ae^{t/\tau}. \tag{4.9}$$

In some cases, the population in a given state may be due to population transfer or feeding from another state. If the population transfer is governed by rate equations, the kinetics may be described by a single exponential decay with an exponential rise.

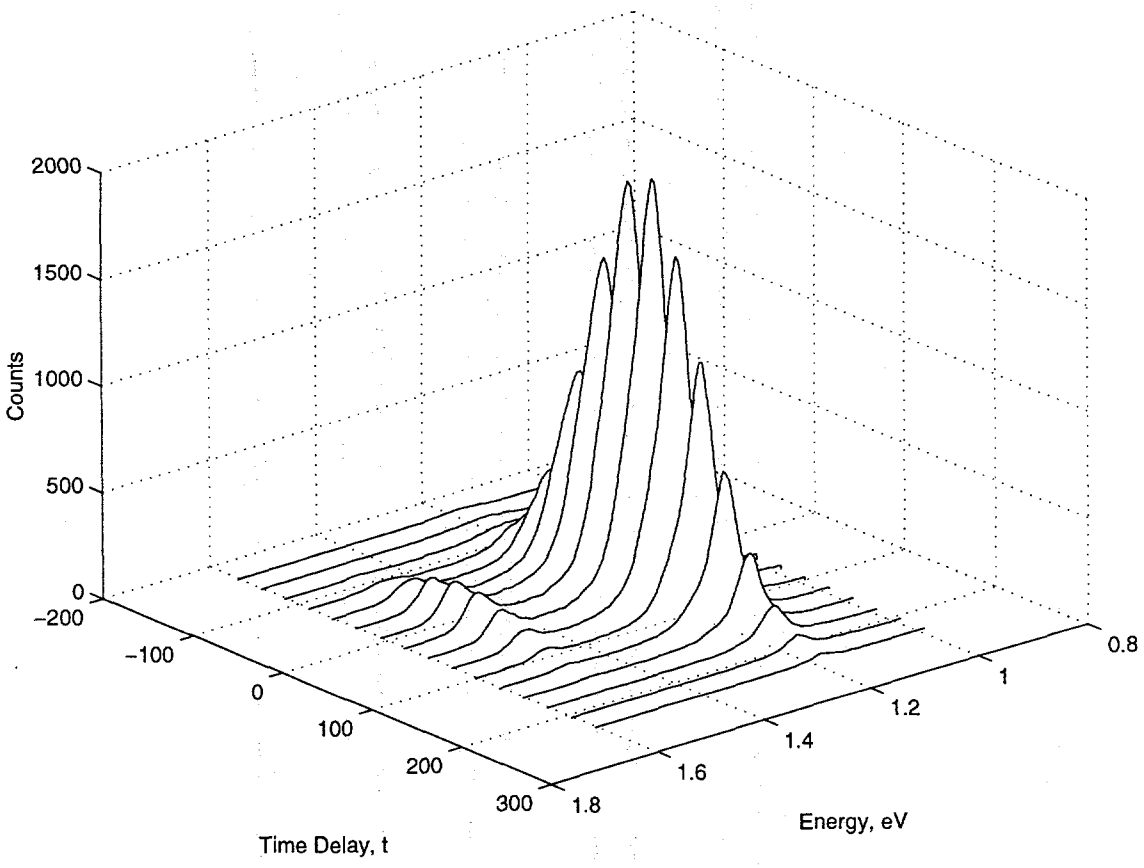

Figure 4.4: The time resolved two photon photoemission spectrum for clean Ag(111) at a probe wavelength of 590 nm. The $n = 0$ surface state and the $n = 1$ image state are visible in the spectrum. The time axis represents the relative delay between pump and probe laser pulses. At $t = 0$, the pulses are coincident in time. The $n = 0$ feature is present at approximately 1.5 eV and the $n = 1$ feature is present at approximately 1.2 eV.

For this case, the functional form is

$$n(t) = A\frac{\tau_1}{\tau_2 - \tau_1}(e^{-t/\tau_1} - e^{-t/\tau_2}). \tag{4.10}$$

Equation 4.10 may be difficult to evaluate numerically near $\tau_2 = \tau_1$, something which must be considered when modeling data using this equation, since many minimization algorithms may become trapped near the discontinuity. It also should be noted that τ_{rise} and τ_{decay} are interchangeable in Equation 4.10. A fit to this equation does not determine which time constant is associated with the rise or decay of population in the state of interest.

When the laser pulse duration and the lifetime of the state of interest are on a similar time scale, the result is a smearing of the kinetics trace. The smearing of the signal is often described as a convolution with an instrument response function. Consider first the case where the pulse duration is short compared to the kinetics being measured. The signal at time t may be represented by the product of the integrated laser intensity I and the population dynamics ($n(t) = Ae^{-t/\tau}$ for $t > 0$ and $n(t) = 0$ for $t < 0$). When the pulse duration and τ are on a similar time scale, the integrated laser intensity I is replaced by a function $I(t)$ which describes its intensity as a function of time. The signal at a given time delay t changes from a simple product of intensity and population to an integral,

$$S(t) \propto \frac{1}{\sqrt{2\pi}}\int_{-\infty}^{\infty} I(t - t')n(t')dt'. \tag{4.11}$$

The above is the definition of the convolution integral [105], hence the signal can be termed a convolution of the probe pulse profile and the function which describes the population. Qualitatively, the non-instantaneous probe pulse with a maximum intensity at time t probes a weighted average of the population in the region near t. The weighted average is represented by the convolution. Similarly, for the case of a non-instantaneous pump pulse, the population as a function of time is smeared compared to the exponential and can be represented as a convolution of the decay function with the time profile of the pump pulse. It can be shown that this pair of convolutions can be represented by a convolution with a single instrument function

R_{inst}. Representing the convolution integral for functions $f(t)$ and $g(t)$ as $f * g$, the signal $S(t)$ is given by

$$S(t) \propto I_2 * (I_1 * n) = R_{inst} * n, \tag{4.12}$$

where $R_{inst}(t)$ is the instrument response function for the pump and probe pulses $I_1(t)$ and $I_2(t)$ given by,

$$R_{inst} = I_1 * I_2. \tag{4.13}$$

The instrument response function given by Equation 4.13 is also known as the cross-correlation of the pump and probe pulses. If the pump and probe pulses are Gaussian in shape, then the cross-correlation is also Gaussian in shape. For the current experiment, the $n = 0$ signal at a given time delay is directly related to the product of the pump and probe intensities integrated over the time axis. The $n = 0$ feature serves as a convenient measure of the time instrument response function for the experiment. A portion of the 35 fs shift from $t = 0$ in the maximum of the $n = 1$ decay trace can be explained in terms of the properties of the convolution. When the symmetric Gaussian instrument response function is convolved with the asymmetric exponential decay, the result is a shift in the maximum. Another portion of the time shift can be attributed to the exponential rise of the $n = 1$ population. An alternative explanation for the exponential rise, one which does not imply initial excitation from the ground level to an upper level and subsequent decay to a lower level, is provided by the optical Bloch equations described later.

4.2.1 Numerical Fitting

As noted in the previous section, it is often necessary to describe the kinetics trace as a convolution of an instrument response function with a function describing the population dynamics (for example, a single exponential function). This complicates the determination of the decay constant τ for a given kinetics trace. In addition, a given data set will contain a certain amount of noise which also complicates the determination of τ. Numerical methods are required both to determine the underlying rate and to generate statistical estimates of the uncertainty of the measured

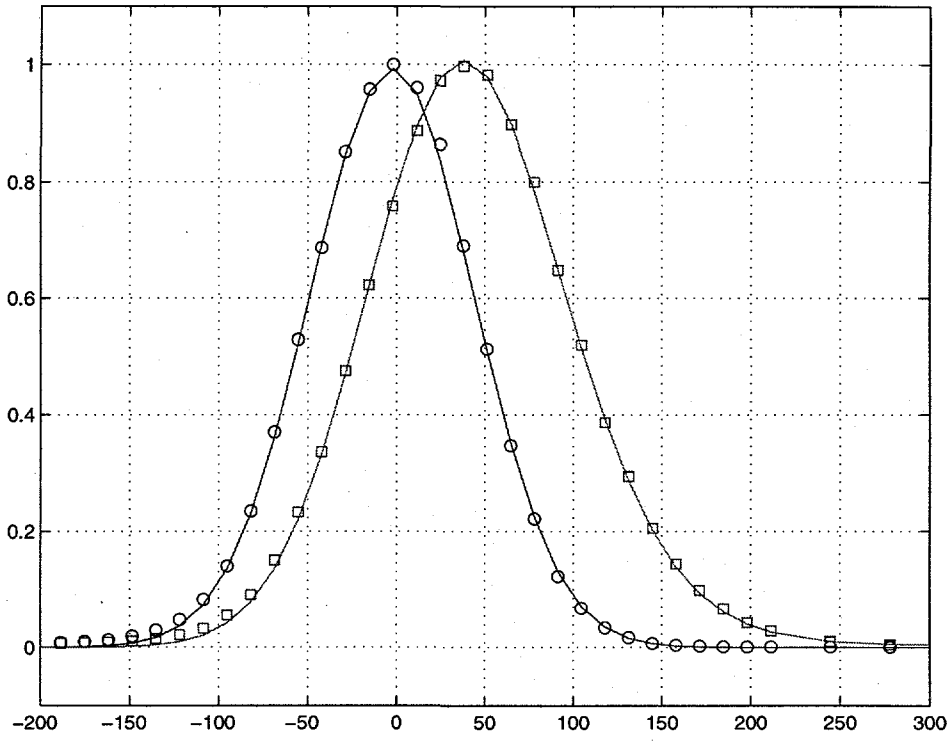

Figure 4.5: The $n = 0$ state (circles) and $n = 1$ state (squares) kinetics traces for clean Ag(111) at 590 nm and a temperature of 50 K. The Gaussian full width half maximum of the $n = 0$ feature is 112 fs and represents the instrument response function.

rate based on the noise or measurement uncertainty associated with the data. In addition to estimates of uncertainties, numerical methods can be used to determine the quality of fit, which is useful in establishing which of two or more candidate models yields a better fit to a given data set.

Numerical evaluation of the convolution may be achieved by using the convolution theorem, which relates the convolution of two functions to their Fourier transforms. The Fourier transform (denoted by $T[]$) of the convolution of two functions is equal to the product of their Fourier transforms,

$$T[S] = T[I_{inst}]T[n] = T[I_{inst} * n]. \tag{4.14}$$

The convolved signal $S(t)$ is obtained by application of the inverse Fourier transform,

$$S = T^{-1}\left[T[S]\right] = T^{-1}\left[T[I_{inst}]T[n]\right]. \tag{4.15}$$

Because the data consist of discrete points, discrete Fourier transforms are employed. The application of discrete Fourier methods to model the effect of an instrument function is covered elsewhere [106]. In principle, it is possible to directly retrieve the population $n(t)$ by direct deconvolution,

$$n(t) = T^{-1}\left[\frac{T[S]}{T[I_{inst}]}\right]. \tag{4.16}$$

The above equation only yields meaningful results when the Fourier transform of I_{inst} is nonzero everywhere. In practice, numerical deconvolution is often not a reliable method for extracting information about $n(t)$. The preferred method for extracting the underlying population $n(t)$ is convolution of a trial function (in this case an exponential decay function) with the instrument response function (a Gaussian instrument function) in conjunction with optimization of the non-linear parameters of the trial function via minimization of the square error $\sum(S_{expt} - S_{model})^2$, a method known as non-linear least squares minimization. There are several methods available for non-linear least squares minimization. The choice of method depends on the kind of data and the functional form of the fitting function. The Levenberg-Marquardt method is a popular and fast gradient search method. Nelder-Mead downhill simplex is slower

but is preferred in some cases. Some implementations of Levenberg-Marquardt minimization behave poorly when degenerate solutions exist, as is often the case when modeling multiple exponential decays. The fit to the data shown in Figure 4.5 was obtained using Nelder-Mead downhill simplex minimization.

It is poor judgment to compare model results and base conclusions on parameters without reliable estimates of the uncertainty in model parameters. Reliable estimates of the uncertainty in the measured time constants may only be determined by careful application of statistical methods to well chosen models. Uncertainty is typically represented by a confidence interval in which it is relatively certain (expressed as a percent probability) that the "true" value resides. Typically a confidence interval of 1σ and 2σ of a Gaussian distribution corresponding to a probability of approximately 67% or 95% is employed. Many implementations of the Levenberg-Marquardt minimization method return uncertainty estimates as part of the calculation. Other methods for determining uncertainty in the model parameters include the constant chi square boundary method and Monte Carlo methods. A common problem in many attempts to estimate experimental uncertainty is the lack of an independent measure of the measurement error σ. In such cases, an estimate of the measurement error is obtained from the residuals of fits to the data. The uncertainties reported here were determined using the constant chi square boundary method.

4.2.2 Coherence Dephasing

The rate equations often used to describe the pump-probe kinetics traces are inadequate for describing systems in which the pump and probe fields interact coherently. In particular, features such as the time shift [40] observed in kinetics traces, narrowing of spectral features with probe delay time (or equivalently, dynamics which are different near the center of the peak than in the wings), quantum beats (oscillations due to interference between two or more states), and the oscillations observed in phase locked spectroscopy are not properly explained in terms of simple rate equations. In such cases, a more complete description which accounts for the interaction of the pump and probe fields is required. An adequate description for many such

cases is provided by the optical Bloch equations.

The following is a description of the optical Bloch equations for a three level system interacting with two laser pulses [107] where the intent is to describe the interactions of ultrafast laser pulses with the surface in a time-resolved two photon photoemission experiment. No detailed description of the optical Bloch equations in this context is available currently in the literature, so an attempt is made here to describe the equations and some of the implications for interpretation of time resolved TPPE. A derivation and discussion of the optical Bloch equations for a two level system is presented in a book by Loudon [41]. For the present system of interest, it is assumed that the two laser frequencies are different, as well as the energy spacings between levels. The initial population is all in the $|0\rangle$ state. The $|0\rangle$ state is assumed to be a continuum or band of states. Additional approximations employed in the standard optical Bloch model for a two level system are also present in the current model, such as the rotating wave approximation. The first field E_a is at or near resonance with the $|0\rangle \rightarrow |1\rangle$ transition and the second field E_b is at or near resonance with the $|1\rangle \rightarrow |2\rangle$ transition. The radiative lifetime T_1 of the intermediate state $|1\rangle$ is finite while the lifetime of final state is assumed to be infinite. There is also a dephasing time T_2 associated with each transition. The dephasing is often explained in terms of small differences in the resonance frequency of a transition which result in broadening of the spectral line. Figure 4.6 indicates the energy levels and fields of the system.

The Hamiltonian $\mathcal{H}$ for the system is given by

$$\mathcal{H} = \mathcal{H}_0 + \mathcal{H}^a_{\mathsf{int}} + \mathcal{H}^b_{\mathsf{int}} + \mathcal{H}_{\mathsf{R}}, \tag{4.17}$$

where $\mathcal{H}^a_{\mathsf{int}}$ is the contribution from the interaction of the electric field E_a, $\mathcal{H}^b_{\mathsf{int}}$ is the contribution from the interaction of the electric field E_b, and $\mathcal{H}_{\mathsf{R}}$ encompasses relaxation effects which result in depopulation and dephasing.

In the dipole approximation, the matrix form of initial and interaction Hamilto-

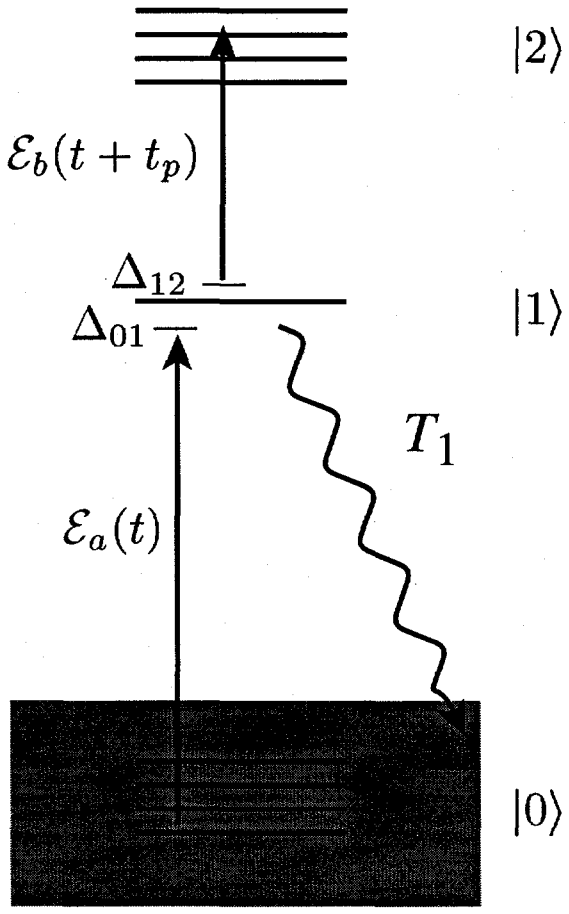

Figure 4.6: Diagram of the energy levels and fields of the optical Bloch equations for the 3 level system representing two photon photoemission. The excitation field is $\mathcal{E}_a(t)$, the probe field is $\mathcal{E}_a(t)$, T_1 is the time constant for state $|1\rangle$, $|0\rangle$ is the initial state, $|1\rangle$ is the intermediate state, $|2\rangle$ is the final state, and Δ_{01}, Δ_{12} are the detunings for the $|0\rangle \rightarrow |1\rangle$ and $|1\rangle \rightarrow |2\rangle$ transitions.

nian can be written

$$\mathcal{H}_0 + \mathcal{H}_{\text{int}} = \begin{pmatrix} \hbar\omega_0 & -\hat{\mu}_a E_a & 0 \\ -\hat{\mu}_a E_a & \hbar\omega_1 & -\hat{\mu}_b E_b \\ 0 & -\hat{\mu}_b E_b & \hbar\omega_2 \end{pmatrix}. \tag{4.18}$$

The field is written as

$$E_a = \mathcal{E}_a(t)\epsilon e^{i\omega_a t} + \text{c.c.}, \tag{4.19}$$

where $\mathcal{E}_a(t)$ is the (Gaussian or sech^2) profile of the laser field (the square root of the intensity $I(t)$).

The system may be described using the density matrix formalism where the density operator is $\rho = |\Psi\rangle\langle\Psi|$ and the density matrix for the three level system is

$$\rho = \begin{pmatrix} \rho_{00} & \rho_{01} & \rho_{02} \\ \rho_{01}^* & \rho_{11} & \rho_{12} \\ \rho_{02}^* & \rho_{11}^* & \rho_{22} \end{pmatrix}. \tag{4.20}$$

The equations of motion of the density matrix are given by

$$\frac{\partial \rho}{\partial t} = \frac{1}{i\hbar}[\mathcal{H}_0 + \mathcal{H}_{\text{int}}, \rho] + \left(\frac{\partial \rho}{\partial t}\right)_R \tag{4.21}$$

and

$$\left(\frac{\partial \rho}{\partial t}\right)_R = \frac{1}{i\hbar}[\mathcal{H}_{\text{R}}, \rho]. \tag{4.22}$$

The matrix elements for relaxation are given by the reciprocal of the dephasing times T_2, T_2', T_2'' and the reciprocal of the population decay time T_1,

$$\left(\frac{\partial \rho_{nn'}}{\partial t}\right)_{\text{R}} = -\rho_{nn'} \begin{bmatrix} 0 & 1/T_2 & 1/T_2'' \\ 1/T_2 & 1/T_1 & 1/T_2' \\ 1/T_2'' & 1/T_2' & 0 \end{bmatrix}. \tag{4.23}$$

This form for the matrix elements $\rho_{nn'}$ is based on the assumption that the diagonal elements decay with a time constant called T_1 which is related to population decay while the off-diagonal elements decay with a time constant called T_2 which is related to dephasing or linewidth.

Explicitly, the equations of motion for each matrix element are given by

$$\frac{\partial}{\partial t}\rho_{00} = -\frac{i\mu_a\mathcal{E}_a(t)}{\hbar}(\tilde{\rho}_{01}-\tilde{\rho}_{10}), \tag{4.24}$$

$$\frac{\partial}{\partial t}\rho_{11} = +\frac{i\mu_a\mathcal{E}_a(t)}{\hbar}(\tilde{\rho}_{01}-\tilde{\rho}_{10}) - \frac{i\mu_b\mathcal{E}_b(t)}{\hbar}(\tilde{\rho}_{12}-\tilde{\rho}_{21}) - \Gamma_1\rho_{11}, \tag{4.25}$$

$$\frac{\partial}{\partial t}\rho_{22} = +\frac{i\mu_b\mathcal{E}_b(t)}{\hbar}(\tilde{\rho}_{12}-\tilde{\rho}_{21}) \tag{4.26}$$

$$\frac{\partial}{\partial t}\tilde{\rho}_{01} = +\frac{i\mu_a\mathcal{E}_a(t)}{2\hbar}(\rho_{11}-\rho_{00}) - \frac{i\mu_b\mathcal{E}_b(t)}{2\hbar}\tilde{\rho}_{02} + (i\Delta_{01}-\Gamma_{01})\tilde{\rho}_{01}, \tag{4.27}$$

$$\frac{\partial}{\partial t}\tilde{\rho}_{12} = +\frac{i\mu_b\mathcal{E}_b(t)}{2\hbar}(\rho_{22}-\rho_{11}) + \frac{i\mu_a\mathcal{E}_a(t)}{2\hbar}\tilde{\rho}_{02} + (i\Delta_{12}-\Gamma_{12})\tilde{\rho}_{12}, \tag{4.28}$$

$$\frac{\partial}{\partial t}\tilde{\rho}_{02} = +\frac{i\mu_a\mathcal{E}_a(t)}{2\hbar}\tilde{\rho}_{12} - \frac{i\mu_b\mathcal{E}_b(t)}{2\hbar}\tilde{\rho}_{01} + (i[\Delta_{12}-\Delta_{01}]-\Gamma_{02})\tilde{\rho}_{02}, \tag{4.29}$$

where $\tilde{\rho}$ is related to ρ by the expression $\tilde{\rho} = e^{i\omega t}\rho$. According to Equation 4.23, the expressions for $\Gamma_1, \Gamma_{01}, \Gamma_{12}, \Gamma_{02}$ are given by

$$\Gamma_1 = \frac{1}{T_1}, \tag{4.30}$$

$$\Gamma_{01} = \Gamma_0^* + \Gamma_1^* + \frac{\Gamma_1}{2}, \tag{4.31}$$

$$\Gamma_{12} = \Gamma_1^* + \Gamma_2^* + \frac{\Gamma_1}{2}, \tag{4.32}$$

$$\Gamma_{02} = \Gamma_0^* + \Gamma_2^*. \tag{4.33}$$

Where T_1 is the lifetime of state $|1\rangle$, Γ_0 is the (dephasing) linewidth of the $|0\rangle$ state, Γ_1^* is the (dephasing) linewidth of state $|1\rangle$ and Γ_2^* is the dephasing linewidth of state $|2\rangle$. The final signal is given by the value of ρ_{22} as $t \to \infty$.

Some of the above parameters are readily obtainable from photoemission and TPPE data, while others may only be obtained through extensive modeling of the data and additional experiments such as phase-locked spectroscopy. The lifetime T_1 of state $|1\rangle$ is readily obtained by fitting the exponential tail of the kinetics trace, provided the lifetime is not too short compared to the pulse width. The linewidth of the initial state $|0\rangle$ may be obtained by measuring its spectral width in an experiment where the wavelength is short enough to excite directly to state $|2\rangle$ (in the case of some TPPE experiments, the initial state is the surface state, the width of which can be determined by UPS). The remaining free parameters are Γ_1^* and Γ_2^*.

The detuning Δ_{01} vanishes for a single initial state when the light frequency is exactly resonant with the $|0\rangle \rightarrow |1\rangle$ transition. When this is not the case (such as for a light source with an appreciable spectral width or when excitation from several initial states is possible), the signal is given by an average over the detunings Δ_{01}. Assuming a continuum of final states, a sum over the detunings Δ_{12} should also be performed. If the energy spectrum is divided into N discrete elements E_k where $k = 1..N$, at a given energy E_k the signal is given by,

$$S_k(t_p) = \sum_{\Delta_{12}} \left[\sum_{\Delta_{01}} \rho_{22}^{t \rightarrow \infty}(t_p) \mathcal{D}_{|1\rangle}(\Delta_{01}) \right] I_k(\Delta_{12}), \tag{4.34}$$

where t_p is the time delay between the pulses and I_k is a function representing the energy resolution of the spectrometer.

Several features of the time-dependent TPPE spectrum are contained in the above set of equations. One feature is the shift of the maximum of the kinetics trace to later times. The "time shift" is due to the fact that the E field does not directly transfer population from $|0\rangle$ to $|1\rangle$, rather it first generates a polarization (represented by the off-diagonal matrix elements) which is transferred to the $|1\rangle$ state by a second interaction with the electric field with a rate of Γ_{01}. The amount of time shift depends on T_2 and the detunings Δ_{01} and Δ_{12}. Also, the exponential tail of the time profile is affected by the detunings. For large detunings, the signal essentially reproduces the instrument response function. In terms of the spectral features, the Bloch equations (Equations 4.24 through 4.29) reproduce the narrowing of peaks at longer probe delay times observed in experimental spectra. Typical variations in line shape as a function of pump-probe delay are shown in Figure 4.7. At early times for the two level picture, the line shape contains contributions from both T_2 and T_1, whereas at later times the peak width is primarily associated with the T_1 population decay. This difference in linewidth has an important impact on the way peak height is determined and its impact on the interpretation of TPPE kinetics traces. If the peak height is determined by integration of the area under the peak, the effect of coherence on the kinetics trace is removed and the results may be interpreted using the rate equations. Also, in cases where the dephasing is fast ($T_2^* << T_1$), the results of the optical Bloch model are the same as those obtained by the rate equations.

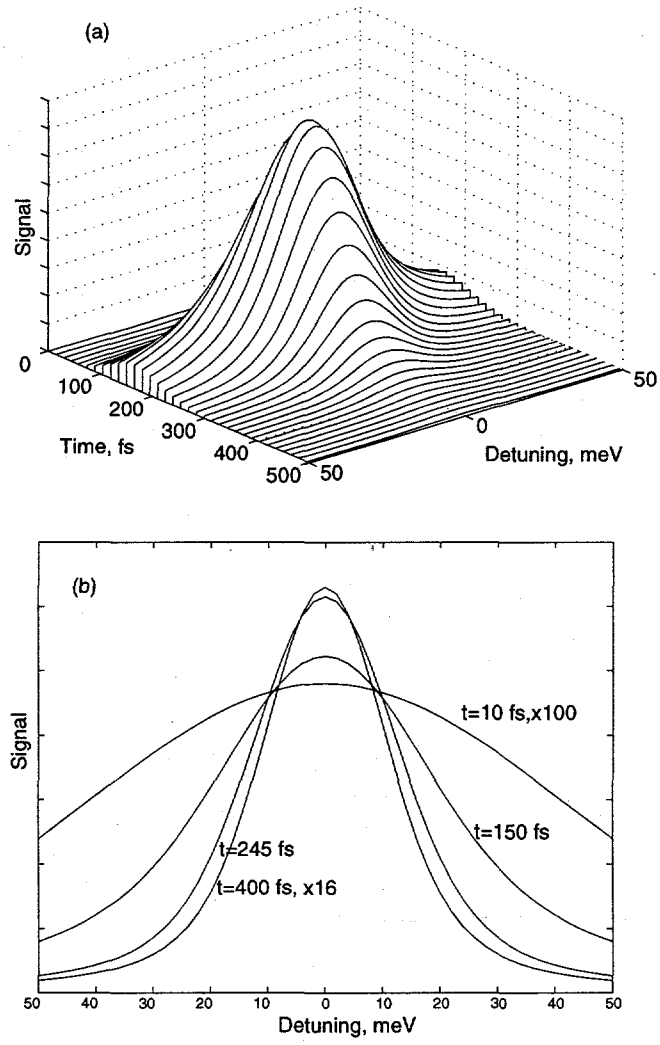

Figure 4.7: The variation in line shape as a function of time as calculated using the optical Bloch equations. A two level system was assumed. The values used in the calculation are $T_1 = 50$ fs, $T_2 = 50$ fs, the coincidence time $t_0 = 150$ fs, the pulse width is 100 fs. Part (a) illustrates the spectrum as a function of time. There is a substantial background near t_0 at all energies which coincides with the time profile of the laser pulse. This feature is also observed in the experiment. Part (b) illustrates the narrowing of the peak as a function of time.

The application of the simpler two state version of the optical Bloch equations to the interpretation of TPPE data [38] has been the subject of some debate in the literature [42]. It can be shown that the assumption of only two states on resonance, together with the assumption of only lifetime dephasing ($T_2^* = \infty$), applied to the $n = 1$ state of Cu(111) yields a result for T_1 which is approximately a factor of two too small. Interestingly, the application of the full three step model to the data yields decay constants closer to those obtained by a fit to the rate equations. This is due to the inclusion of additional dephasing parameters associated with the additional energy level, which has the effect of reducing coherence. The additional parameters introduced by the three step model complicate the fitting procedure. Researchers should apply this powerful methodology with care, as misapplication or incorrect or hidden assumptions may result in large systematic errors in reported results. It is useful to compare the results of the Bloch models to the results of the rate equations for a given set of data. If there is a large discrepancy between rate model and Bloch model results, the Bloch model results should be viewed with skepticism. The optical Bloch equations reduce to the standard rate equations in the incoherent limit ($T_1 >> T_2^*$). It should be noted that coherence dephasing is not the only possible explanation of the time shift evident in kinetics traces. Another possibility is feeding from other states which are higher in energy, in which the time delay can be attributed to the rate at which the higher energy states feed population into the state of interest (this system is described by an exponential rise and decay function, shown in Equation 4.10). A questionable practice is the use of linewidths derived from experimental spectra to reduce the number of free parameters in the Bloch model. That a particular measured linewidth is relevant to the transition in question should be established by additional, independent experiments before such an assumption is used in data analysis. In addition, slight differences in sample preparation or the cleanliness of the surface can cause differing amounts of surface inhomogeneities which may result in substantially different measured linewidths or dephasing (T_2^*) times.

Because of the concerns raised in the previous paragraph, the time-resolved data presented later is interpreted using the standard rate equations. Spectral peak areas

were determined by fitting the peak to a Voight function of fixed width using linear least squares. For most of the data presented here, the inclusion of an exponential rise improved the fit substantially. It is speculated that the exponential rise is due to feeding from states of higher parallel momentum.

4.3 Quantum Well States of Xe: Spectral Features

This section describes two photon photoemission experiments on multiple molecular layers of Xenon on the Ag(111) substrate and the development of a 1-D quantum-mechanical model for the resulting binding energies using multiple reflection theory in conjunction with a continuum dielectric theory. Portions of this section are adapted from a paper by McNeill and coworkers [108]. Solid Xenon serves as a model system for understanding aspects of band structure and transport in both semiconductors [109] and insulators [110] due to its large band gap and high excess electron mobility. Also, the study of quantum well (QW) states associated with such layers should provide important information about the bulk band structure [81]. Recently, ultraviolet photoemission spectroscopy has been used to investigate the occupied valence band quantum well electronic states in metal/metal [84], metal/semiconductor [82, 83], and metal/insulator [85, 86] systems. In this section, angle-resolved two-photon photoemission (ARTPPE) spectra of the excited quantum well and image states in the presence of insulating layers of Xe and Kr on Ag(111) are presented.

Previously, this technique was used to study a monolayer of Xe where the changes in image state binding energy and dispersion were assigned to the work function shift due to adsorption and the polarization of the Xe layer [96]. ARTPPE investigations of layers of alkanes [95,111] revealed a sensitive dependence of the electronic structure on the layer thickness and the presence of localized electronic states. TPPE spectra of layers of metal on metal [24–26,103] have demonstrated the pinning of image states to the local work function, line width broadening due to lateral electron confinement on islands of adsorbate, and quantum well states.

There are several factors that are expected to influence the energies of excited

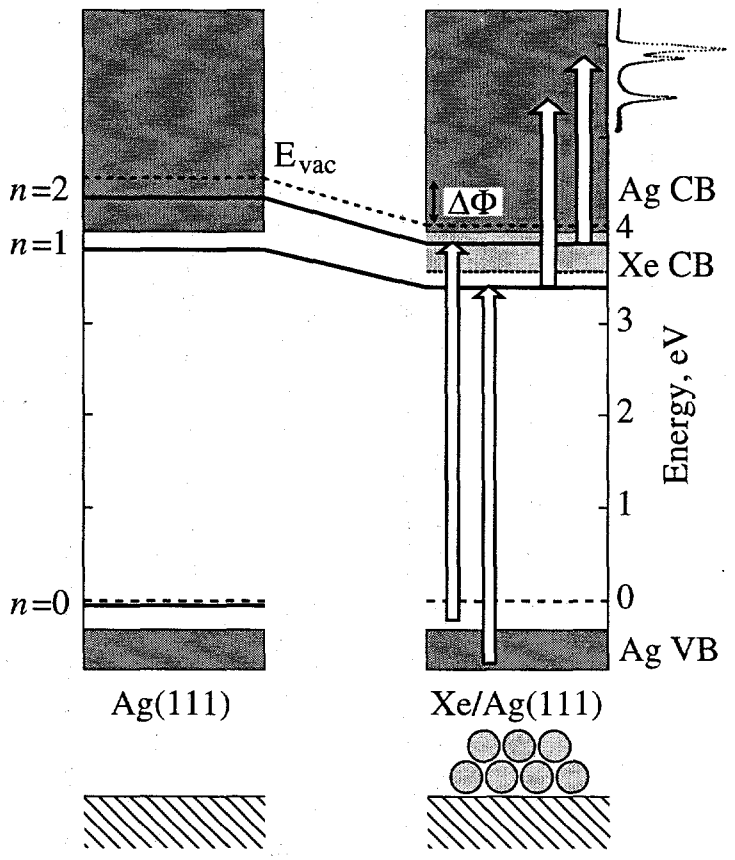

Figure 4.8: The surface-projected band structure for (left) clean Ag(111) and (right) Xe on Ag(111). The zero of energy is set to the Fermi level. The adsorption of a monolayer Xe reduces the work function Φ by 0.5 eV. This lowers the image state energies with respect to the Fermi level since image states are pinned to the vacuum level. Adsorption of additional layers of Xe results in the formation of quantum well states. The Xe and Ag(111) bands are denoted by light and dark shading, respectively. A two-photon photoemission spectrum for a bilayer of Xe on Ag(111) containing the $n = 1, 2$, and 3 peaks is shown on the right hand side.

electronic states at the Xe/Ag(111) interface. A diagram of the relevant energy levels of the Xe layer and the substrate is shown in Figure 4.8. Xe possesses a large energy gap and electrons in solid Xe have a high mobility. Since Xe is relatively inert, no chemical bonding exists between the Xe layer and the Ag substrate. The empty 6S orbital forms a conduction band below the vacuum level. The conduction band, which is located near the vacuum level, should influence the energies of interface electronic bands. Because of the symmetry of the thin layer system and the substrate, the electron is confined by the vacuum potential and the substrate band gap, resulting in discrete states perpendicular to the surface. Along the surface parallel, the states form continuous bands. Quantum confinement of the electron within the layer may affect band energies. The effective mass of the Xe conduction band, which is rather less than that of a free electron, should influence the parallel dispersion of the image bands. Also, the dielectric constant of Xe should affect the shape and depth of the image potential well near the Xe surface. The effect of the conduction band and quantum confinement are addressed by taking photoemission spectra at a range of coverages. The dispersion or effective mass of the interface bands is determined by angle-resolved two photon photoemission.

4.3.1 Experimental

For this set of experiments, a 2 MHz train of 6 ps pulses at wavelengths of 590–620 nm was generated by a synchronously-pumped, cavity-dumped dye laser. Second harmonic generation was achieved by means of a 2 mm BBO crystal. The laser was tuned so that the photon energy of the second harmonic was just below the work function in order to be able to investigate states near the vacuum level while keeping one-photon photoemission down to acceptable levels (below the point where space-charge broadening has a noticeable effect on the spectral features). The second harmonic and the residual fundamental beam were focused collinearly on the sample. The energies of emitted electrons were determined by time-of-flight.

At a given angle θ the wave vector along the surface parallel $k_{\|}$ was determined

from the sample angle and photoelectron kinetic energy E as follows,

$$k_{\|} = \sqrt{2m_e E/\hbar^2}\sin\theta. \tag{4.35}$$

A fit to the parabolic dispersion relation, $E = E_0 + \hbar^2 k_{\|}^2/2m^*$, where E_0 is the kinetic energy for emission normal to the surface, determined the effective mass m^*.

The sample was cooled to 45 K by means of a liquid helium cryostat. The UHV chamber background pressure was $\sim 1 \times 10^{-10}$ torr. Mono- and bilayer Kr and Xe were obtained by cooling the sample and backfilling the chamber with sample gas at pressures and sample temperatures specified by the phase diagrams of Kr and Xe on Ag(111) [112,113]. At a Xe pressure of $\sim 2 \times 10^{-6}$ torr and at temperatures between 82–68 K a monolayer of Xe formed. At a Xe pressure of $\sim 2 \times 10^{-6}$ torr and a temperature of 67–66 K a bilayer formed. Experiments were performed quickly to minimize the effects of contaminants in the chamber or sample gas. Xenon multilayers were formed by carefully metered dosing of the cooled (~45 K) sample. The spectrum for a monolayer Xe grown by backfilling the chamber with Xe at temperatures and pressures specified by the 2-D phase diagram of Xe/Ag(111) was indistinguishable from the spectrum for a monolayer of Xe obtained by metered Langmuir dosing at 45 K. This is consistent with Xe/Ag(111) X-ray structure results [114], which show Xe to form an incommensurate hexagonal layer on the Ag(111) surface for layers grown by both methods. Two photon photoemission spectra were obtained for 1–9 layers of Xe, as shown in Figure 4.9.

The adsorption-induced work function shift changes the contact potential difference between the sample and detector which in turn changes the measured kinetic energy of the photoelectrons. In order to determine binding energies with respect to the vacuum, the work function change must be determined. The adsorbate-induced work function shift $\Delta\Phi$ was determined by TPPE and confirmed via threshold UPS. A fit of the UPS data to the Fowler form [115, 116] was used to extract the work function from the photoemission data. In addition, the work function shift was determined from the TPPE spectrum by analyzing the convergence of the image series to the vacuum level using the quantum defect formula, $E = -.85/(n+a)^2$, and simultaneously solving for the quantum defect a, the binding energy with respect to

the vacuum E, and the position of the vacuum level (the energy to which the series converges), for both the clean and the adsorbate-covered surface. Then the difference between the vacuum level for the clean and adsorbate-covered surface yields the work function change due to adsorption. The quantum defect formula can only be applied to the bare surface and the monolayer, where the states are still approximately hydrogenic. For bilayer, only UPS results were used. The UPS and TPPE results for the work function change due to the monolayer agree to within 10 meV. Our results differed somewhat from other threshold photoemission work [117] in that most of the work function difference was observed in the first layer ($\Delta\Phi = -.500$ eV), with a small shift ($\Delta\Phi = -.036$ eV) for the second layer, and no shift within experimental uncertainty for the third layer. We attribute this discrepancy to uncertainty in the determination of coverage in the previous work. In the present work, the coverage could be determined precisely by monitoring the TPPE spectrum. The work function shift due to the presence of a monolayer of Kr was determined to be approximately $-.30$ eV.

The parallel dispersion was measured by varying the angle of the sample with respect to the detector rotating the goniometer sector on which the sample is mounted. Typical spectra for a range of sample angles are shown in Figure 4.10 along with a dispersion plot.

4.3.2 Coverage Dependence of the Spectral Features

The TPPE spectra of Xe/Ag(111) at various thicknesses of Xe are presented in Figure 4.9, and the binding energies of the $n = 1, 2, 3$ states are plotted in Figure 4.11. The labels $n = 1, 2, 3$ represent the image state levels to which the states correspond in the limit of zero coverage. The binding energies are also shown in Table 4.1. The binding energies of the image states on a monolayer of Kr were determined to be $-.62$ and $-.19$ eV for $n = 1$ and $n = 2$, respectively.

For the first layer, the features are similar to the $n = 1, 2, 3$ image states of clean Ag(111), as shown by Merry *et al.* [96]. The spectral features shift in energy and change in relative amplitude as the Xe coverage is varied from 1 to 9 monolayers.

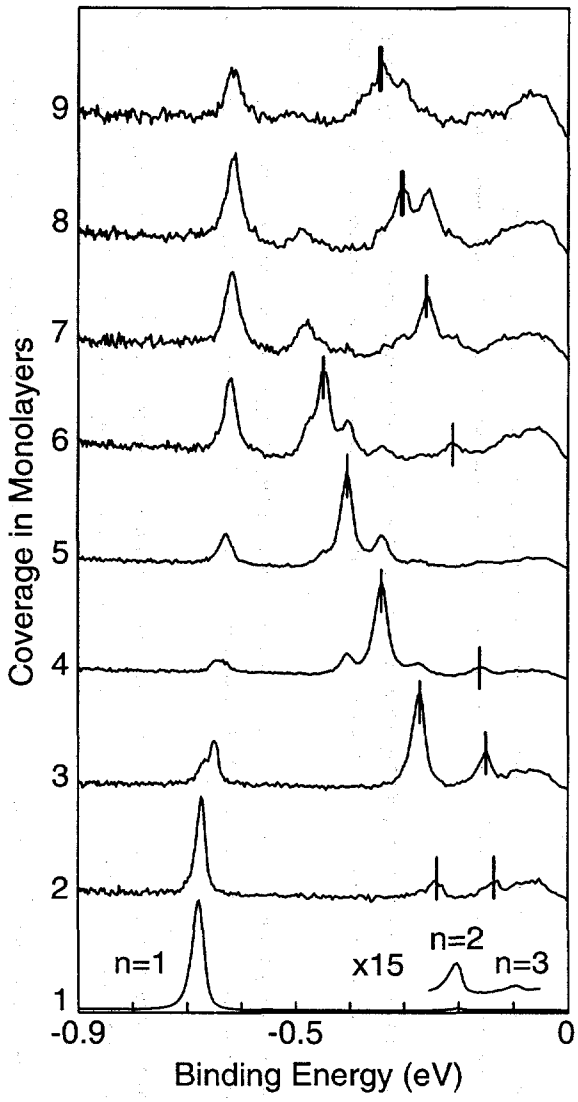

Figure 4.9: Two-photon photoemission spectra of Xe/Ag(111) at a series of coverages (1–9 atomic layers, approximately). After two layers, the Xe coverage is non-uniform, and peaks corresponding to more than one coverage are visible in a given spectrum. The dark line through the peaks indicates which peak is assigned to the coverage (in monolayers) indicated at the left of the figure.

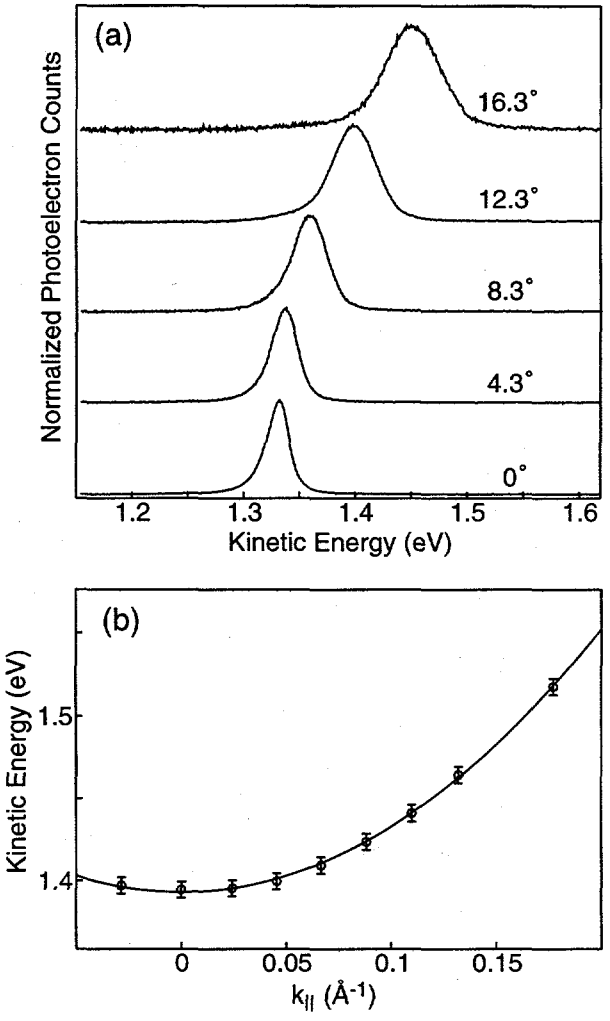

Figure 4.10: In plot (a) spectra of the $n = 1$ state of a monolayer of Xe on Ag(111) at a series of angles are displayed. The peak energy positions are used to determine the dispersion relation. In plot (b) reduced dispersion data for a monolayer of Xe on Ag(111) are shown along with a parabolic fit determining the experimental effective mass, yielding $m^*/m_e = .95 \pm .1$.

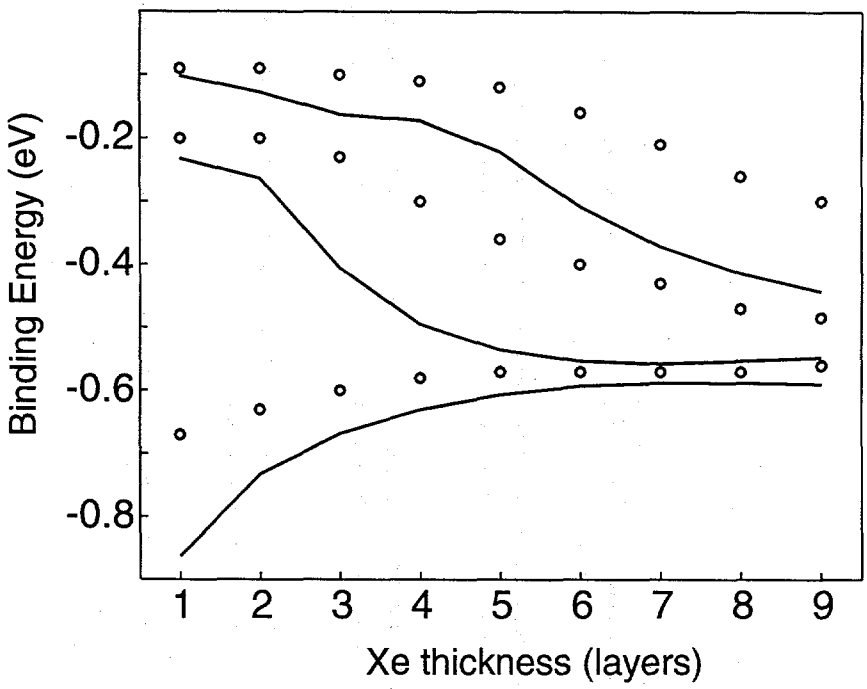

Figure 4.11: Experimental binding energies (symbols) of the $n = 1, 2, 3$ states as a function of Xe coverage, and a comparison to the results of a dielectric model (solid lines). Energies are with respect to the vacuum level.

Layers	$n = 1$	$n = 2$	$n = 3$
1	−.67	−.20	−.09
2	−.63	−.20	−.09
3	−.60	−.23	−.10
4	−.60	−.30	−.11
5	−.58	−.36	−.12
6	−.57	−.40	−.16
7	−.57	−.43	−.21
8	−.57	−.47	−.26

Table 4.1: Binding energies for the $n = 1, 2, 3$ states for one to eight layers of Xe on Ag(111). Energies are reported in eV with respect to the vacuum level.

The $n = 1$ feature on a monolayer of Xe is significantly narrower than that of the clean Ag(111) surface, indicating a longer lifetime of the $n = 1$ state in the presence of a layer of Xe. At the completion of a bilayer, the signal intensity of the $n = 1$ peak is reduced relative to the $n = 2, 3$ features while the peak shifts to lower binding energy. The binding energy of the $n = 1$ state decreases by 16% over the range of 1–9 layers. Most of this shift takes place over the first few layers. A similar decrease in binding energy with layer thickness has been observed for image states on n-alkanes [95], which have a negative (repulsive) electron affinity [118, 119] and where the image state electron density is located in the vacuum. Due to the similarity of the coverage dependence for $n = 1$ on Xe/Ag(111) with the coverage dependence for $n = 1$ observed on alkane layers, the $n = 1$ state is tentatively assigned to be an image state residing primarily at the Xe/vacuum interface. For an electron residing outside the layer, the primary effect of the layer is dielectric screening of the image potential. The effect of the layer on the $n = 1$ energies can therefore be modeled using the dielectric continuum model which treats the adsorbate as a structureless dielectric.

The binding energies of the $n = 2, 3$ states monotonically increase as the number of layers increases. The marked contrast between the coverage dependence of the $n = 1$ peak and the $n = 2, 3$ peaks suggests that the states exist in different locations along the axis perpendicular to the surface. The coverage dependence of the $n = 1$

peak is characteristic of image states outside an insulating layer, whereas the binding energies of the $n = 2, 3$ states at higher coverage are close to the Xe conduction band minimum, an indication of QW states of the Xe layer. At intermediate coverage, the $n = 2, 3$ state energies are between image state $(-.85/n^2)$ energies and the Xe conduction band minimum, indicating mixed behavior. The energies of the $n = 2$ and 3 states at higher coverage are modeled using a quantum well model which represents the Xe band structure and treats the coverage dependence of the energies as a quantum confinement effect which splits the Xe band into a series of discrete states. Dielectric effects are ignored in this model.

These initial observations on the coverage dependence of the binding energies of all the interface states are consistent with a picture in which the attractive electron affinity of the Xe slab provides a shallow quantum well, bounded by the bulk band gap of the substrate on one side and the image potential on the other side. This picture forms the basis of a third model which represents an attempt to bring the two pictures together in a way which more accurately reflects the observed binding energies of both image states and quantum well states at all coverages and which includes the most important features identified in previous models: the band structure of the metal substrate, the band structure of the Xe overlayer, and the screened image potential of the adsorbate/metal system.

The parallel dispersion of the TPPE features was determined for 1–4 layers of Xe and for one and two layers of Kr. The angle-resolved spectra of the $n = 1$ state on a monolayer of Xe at a series of angles between 0° and 16° are shown in Figure 4.10 along with the reduced parallel dispersion data with a parabolic fit. The coverage dependence of the effective mass of the $n = 1, 2$ states of Xe/Ag(111) is shown in Figure 4.12. For both the $n = 1$ and $n = 2$ states, the effective mass goes from that of a free electron ($0.95 \pm 0.1 m_e$ for $n = 1$) at monolayer coverage to significantly less than that of a free electron ($0.6 \pm 0.2 m_e$ for $n = 1$) at 4 layers of coverage. The $n = 1$ effective masses for 1–2 layers of Kr follow the same trend as for Xe ($0.9 \pm 0.1 m_e$ for a monolayer, $0.8 \pm 0.2 m_e$ for a bilayer). The dispersion measurements are complementary to the binding energy measurements in that they yield information about electronic structure and transport properties in the plane of

the interface. These results are later interpreted using a model which includes the 3D band structure of the substrate and overlayer material in calculating the energies of the interfacial electronic states as a function of parallel momentum.

4.3.3 Dielectric Continuum Model

To model image states perturbed by the presence of the dielectric layer, the well-established dielectric continuum model for image states outside an insulator layer on a perfect conductor was employed. The analytical form of the solution to this problem was first presented along with numerical solutions by Cole [120, 121]. An approximate analytic form for the wave function was developed by Trninić-Radja and coworkers [122]. This model represents an attempt to account for the effect of the dielectric nature of the adsorbate (represented by a dielectric constant and an affinity level) on image state binding energies. Binding energies for image states on liquid He [123] and thin layers of alkanes on a metal [118, 119] can be explained by this model. However, this model does not take into account the band structure of the layer and substrate, which should be important for states near in energy to the Xe conduction band. In the next two sections, models which take into account the band structure of Xe are presented.

In the dielectric continuum model, the electrostatic potential on the inside of the dielectric slab as presented by Jackson [124] is given by,

$$\begin{aligned} V_i(z) = \quad & -\frac{e^2}{4\epsilon z} + \frac{e^2(\epsilon-1)}{4\epsilon(\epsilon+1)(t-z)} \\ & -\frac{e^2(\epsilon-1)(t+2z)}{4\epsilon(\epsilon+1)t(t+z)} + \delta V_i(z) - EA, \end{aligned} \tag{4.36}$$

where z is the distance from the metal surface, t is the thickness of the layer, the electron affinity of the layer EA is treated as an additive constant and is set to 0.5 eV [125] (which corresponds to the Xe conduction band minimum), ϵ is the static dielectric constant of Xe, and the correction term is given by the infinite series

$$\delta V_i(z) = -\frac{e^2 z^2}{2\epsilon t^3} \sum_{k=2}^{\infty} \frac{(-1)^k}{k(k^2 - z^2/t^2)} \left(\frac{\epsilon-1}{\epsilon+1}\right)^k. \tag{4.37}$$

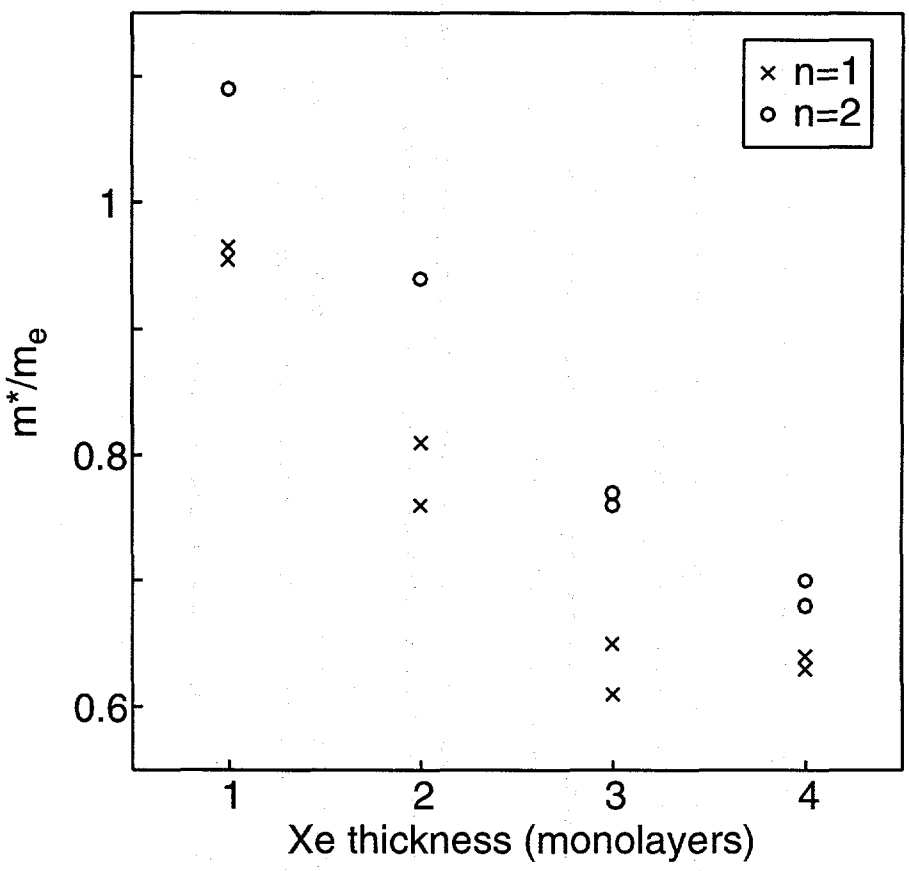

Figure 4.12: Effective masses of $n = 1$ and $n = 2$ states as a function of Xe coverage. Data from two separate experiments are shown.

Numerical computation yields the following explicit approximation for $\delta V_i(z)$,

$$\delta V_i(z) \approx \delta V_i(t) \cdot \frac{z^2}{t^2}\left[1 - .55(1 - z/t) + .30(1 - z/t)^2\right]. \tag{4.38}$$

The series for δV_i can be summed at $z = t$ to give,

$$\delta V_i(t) = \frac{e^2}{4\epsilon t}\left[\frac{(1+\beta)^2}{\beta}\ln(1+\beta) - \frac{3}{2}\beta - 1\right] \text{where} \beta = \frac{\epsilon - 1}{\epsilon + 1}. \tag{4.39}$$

The electrostatic potential in the vacuum, first presented by Cole [121], can be written as,

$$V_o(z) = -\frac{e^2}{2(\epsilon+1)z} - \frac{e^2(\epsilon-1)}{4(\epsilon+1)(z-t)} + \delta V_o(z) \tag{4.40}$$

and the correction term is given by,

$$\delta V_o(z) = -\frac{e^2\epsilon t}{(\epsilon+1)^2 z}\sum_{k=1}^{\infty}\frac{(-1)^{k-1}k}{(kt+z)}\left(\frac{\epsilon-1}{\epsilon+1}\right)^k. \tag{4.41}$$

The correction term can adequately be approximated by,

$$\delta V_o(z) \approx \frac{2t^2}{z(t+z)} \cdot \frac{\delta V_o(t)}{1 + 0.222\left(\frac{\epsilon-1}{\epsilon+1}\right)\cdot\ln(z/t)}, \tag{4.42}$$

where the value of δV_o at $z = t$ is given by,

$$\delta V_o(t) = -\frac{e^2}{t}\left[\frac{\epsilon}{(\epsilon^2-1)}\cdot\ln\left(\frac{2\epsilon}{\epsilon+1}\right) - \frac{1}{2(\epsilon+1)}\right]. \tag{4.43}$$

Two steps were taken to avoid the singularities in the electrostatic solution at the interface boundaries. First, a cutoff was imposed at -4 eV near the metal, resulting in a bare metal binding energy of $-.75$ eV which is close to the experimental value for clean Ag(111) of $-.77$ eV. Second, the potential is linearly interpolated between $V(t-b/2)$ and $V(t+b/2)$ near the dielectric/vacuum interface. Eigenvalues for the model potential were determined using an implementation of the discrete variable representation (DVR) [126]. Subsequent calculations were performed using a Runge-Kutta integrator as described in the next section. It was found that the DVR implementation was inefficient (optimized for harmonic wells) and somewhat inaccurate (the wave function did not completely vanish at the origin as required) for the potential of interest.

The potential given by the dielectric model for $\epsilon = 3.0$, $EA = 0.5$ eV, and $b = 3$ Å for various layer thicknesses is shown in Figure 4.13. The resulting binding energies are shown in Figure 4.11, plotted with the binding energies extracted from the data of Figure 4.9. Although the model overestimates the binding energies for all three states, it is significant that it does reproduce the major trends in the data: the $n = 1$ image potential state energy becomes more positive while the higher quantum state energies become more negative as the adlayer thickness increases.

Analysis of the model results yields the following observations. First, the $n = 1$ electron is partially excluded from the layer by the potential barrier represented by the electron affinity. This can be seen in the the wave functions predicted by the continuum model which show a tendency for the probability associated with the $n = 1$ image potential electron to move out toward the adlayer/vacuum interface as shown in Figure 4.14. Second, the electron affinity presents an attractive potential within the layer for the $n = 2, 3$ states. The $n = 2, 3$ image states transform into quantum well states of the layer as thickness increases. This suggests that the $n = 2, 3$ energies should be analyzed by a model which takes explicit account of their quantum well character, including the effective mass of the Xe conduction band. The proximity of the $n = 2$ and 3 states to the substrate suggests it is appropriate to include the substrate band structure as well.

4.3.4 Discrete Wave Vector Model for QW States

Loly and Pendry [81] proposed using photoemission from thin layers as a method for achieving highly accurate valence band structure measurements. Here this approach is applied for the first time to two photon photoemission, yielding accurate conduction band measurements. According to the theory of Loly and Pendry [81], QW wave functions possess a factor of $\sin k_z z$. For wave functions in a layer N atoms deep the wave function must vanish at $z = 0$ and Nd, where d is the interplanar spacing, leading to the bound state condition $k_z = \pi j/Nd$, where j is the quantum number of the QW state. In the effective mass approximation the energy levels will follow the dispersion relation $E = \hbar^2 k_z^2/2m^*$. Thus the electronic energy levels of a

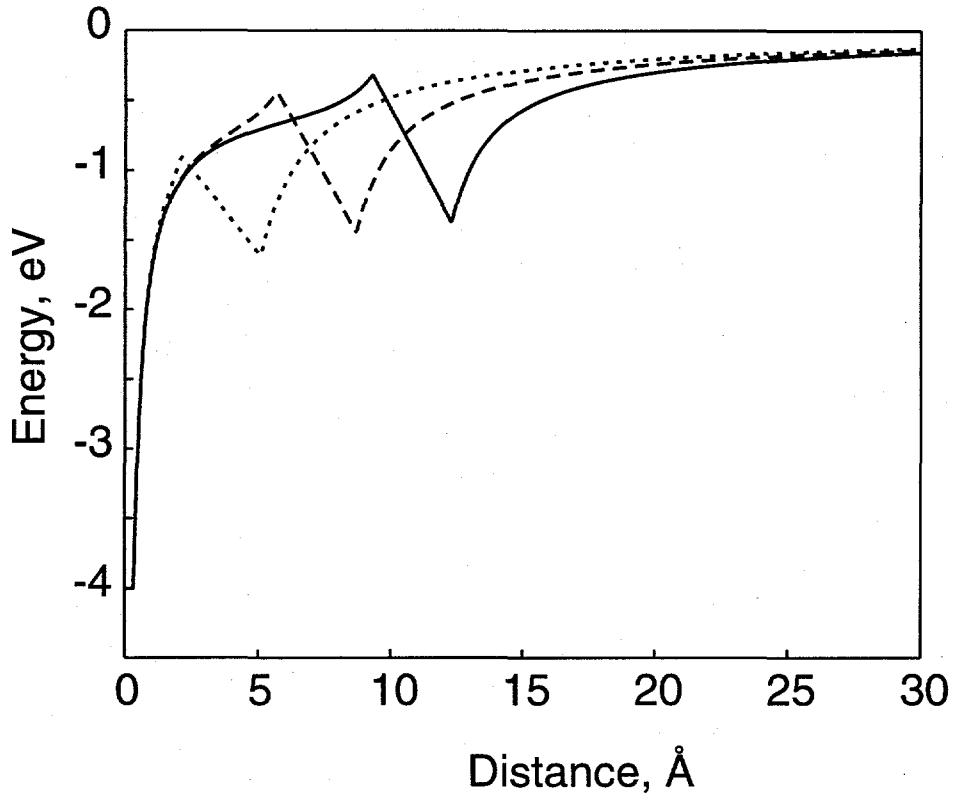

Figure 4.13: The potential used in the dielectric model eigenenergy calculations. The potential is the solution to the electrostatic problem of an electron in or near a dielectric slab on a metal surface. The results for 1–3 layers of Xe (3.6 Å per layer, $\epsilon = 3.0$) are shown. The image potential at the metal is cut off at -4 eV. The potential is linearly interpolated over a region of width $b = 3$ Å at the Xe/vacuum interface.

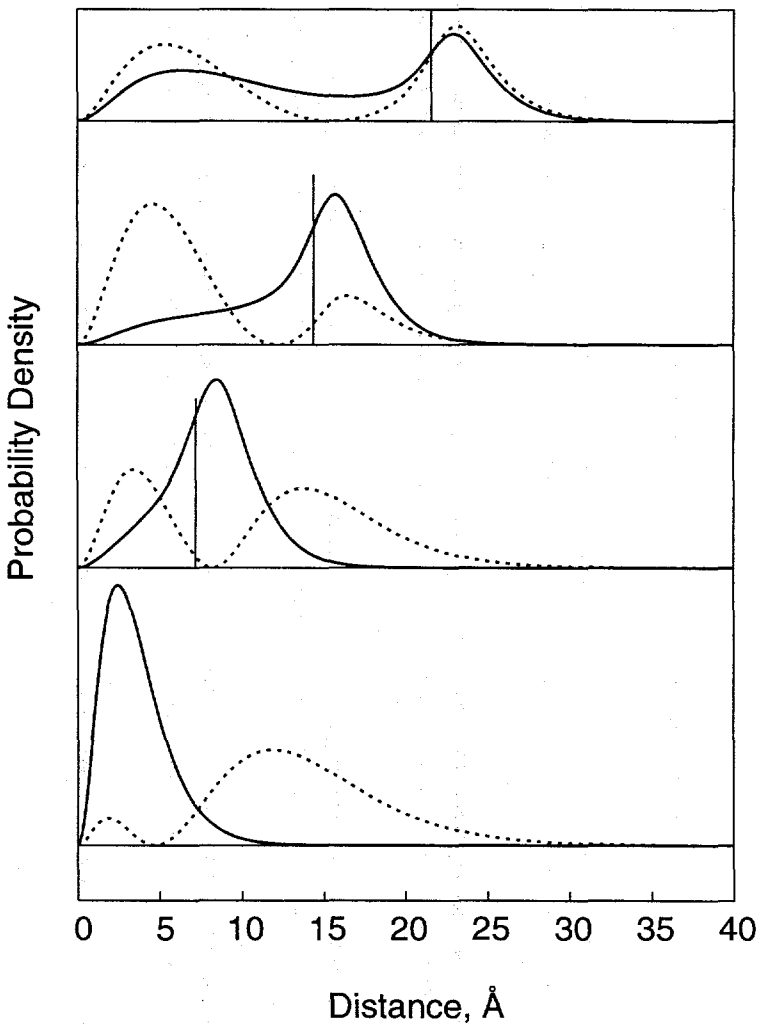

Figure 4.14: The resulting probability densities for the dielectric continuum model for the $n = 1$ (solid lines) and $n = 2$ (dashed lines) states for 0,2,4, and 6 layers of a slab of dielectric constant $\epsilon = 3.0$ and electron affinity $EA = 0.5$ eV. This figure illustrates the tendency of the $n = 1$ state to have significant electron density at the Xe/vacuum interface at these coverages while the $n = 2$ state looks like a hydrogenic $n = 2$ image state for a monolayer but tends to move inside the layer and have a node near the Xe/vacuum interface, which is indicative of a quantum well state, for thicker layers.

quantum well can be thought of as a discretized band structure. If the energies of the states for a range of thickness are plotted against k_z, the perpendicular dispersion can be observed. The band structure information obtained by this analysis is complementary to band structure information obtained by angle resolved measurements of the parallel dispersion: by performing angle resolved measurements and coverage resolved measurements, a large area of the 3-D surface corresponding to the conduction band ($E(k_{||}, k_z)$) can be determined.

In Figure 4.15 the binding energies of the $n = 2, 3$ states are plotted with respect to the perpendicular momentum along with a fit to a parabola determining an experimental value for the Xe conduction band edge of $-.55$ eV and an effective mass of $.57m_e$. Here we have assumed that the $n = 2, 3$ states are the $j = 1, 2$ quantum well states, respectively. The binding energies qualitatively match the expected quantum well behavior for 7–9 Xe layers. In the range of 1–3 layers the dispersion is too flat to correspond to a QW state derived from the Xe conduction band, suggesting that $n = 2, 3$ are modified image states at low coverage. At intermediate coverage the slope of the dispersion curve changes smoothly from flat dispersion to parabolic dispersion, suggesting that the $n = 2, 3$ states in this range are "mixed" states that possess both image state and QW state character, *i.e.*, the states possess significant probability density in the layer and the vacuum.

The crossover between image-like and quantum well-like behavior appears to occur at approximately the thickness corresponding to the expectation value $\langle z \rangle = 6a_0n^2$ for the same state in the hydrogenic image state model [17]– at four layers (14 Å thick) for $n = 2$ and at seven layers (25 Å thick) for $n = 3$. This result can be interpreted in terms of perturbation theory as follows. For the monolayer, the states are only slightly perturbed from those of the clean surface because of the small spatial overlap of the layer potential with the hydrogenic (zero order) wave function. When the layer is thick enough for significant overlap with the zero order wave function ($t \simeq \langle z \rangle$) , the $n = 2, 3$ wave functions are brought down in energy by the attractive Xe layer potential. In contrast, the $n = 1$ state energy is in the Xe gap, therefore the $n = 1$ state is pushed out into the vacuum by the Xe layer.

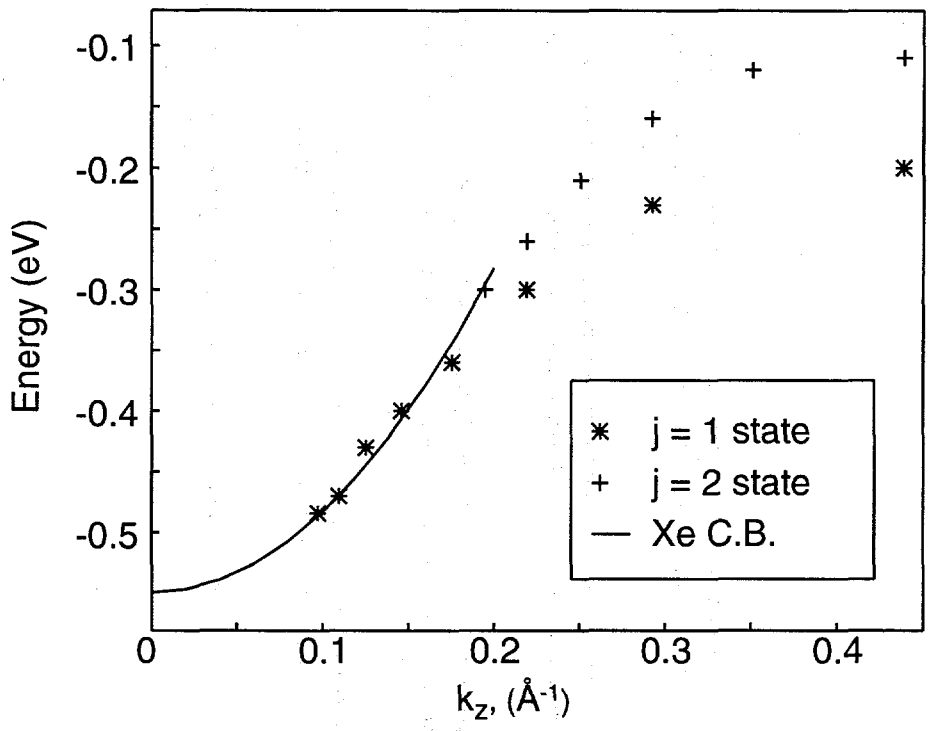

Figure 4.15: Perpendicular dispersion plot of Xe quantum well states. The perpendicular wave vector is determined by the layer thickness and the quantum number of the state. The perpendicular dispersion of the $j = 1, 2$ quantum well states (which correspond to the $n = 2, 3$ image states) is fit to a parabola, yielding a Xe conduction band minimum of $-.55$ eV and an effective mass of $.57m_e$. The higher k_z values correspond to lower coverage. Energies for the $j = 1$ state are plotted versus k_z for 2–9 Xe layers, and energies for the $j = 2$ state are plotted versus k_z for 4–9 layers.

4.3.5 A Quantum Well on an NFE Substrate

The dielectric model with a hard wall at the metal correctly predicts the gross features of the data but fails quantitatively, especially in that the energies of $n = 2, 3$ drop too quickly as a function of layer thickness. The discrete wave vector model ignores the metal substrate and the image potential in the vacuum. Here an attempt is made to develop a simple model which takes into account the important physics of both models and properly treats the electronic structure of the substrate. QW states of a metal layer on a metal substrate have been successfully modeled as a two-band nearly-free-electron (NFE) metal on a two-band NFE substrate with an image potential in the vacuum [87, 127]. However, the wide Xe gap with a flat core-level valence band precludes the use of the two-band NFE model for states near the Xe conduction band. It is more proper to ignore the Xe valence band by setting V_{Xe} to the Xe conduction band minimum and using the effective mass approximation for the conduction band dispersion. Therefore the Ag(111) substrate is treated as an NFE material and a potential is constructed outside the metal using the effective mass approximation to the Xe conduction band and the image potential outside a dielectric slab on a metal substrate from Section 4.3.3.

The details of the model are as follows. In the substrate the two-band NFE approximation is used. This approximation has been successful in describing the substrate for the case of surface states in the band gap of a metal. Such states possess an exponential tail in the metal which can be adequately described in the two-band NFE approximation. The two band NFE model is detailed in Chapter 2.

A value of $-.55$ eV with respect to the vacuum is used for the bulk Xe conduction band minimum and a bulk Xe effective mass of $.57m_e$ taken from the discrete wave vector analysis in the previous section. The Xe interplanar spacing of 3.577 Å was taken from X-ray data [114]. The Ag(111) parameters were taken from calculations of clean surface image and surface state binding energies [19]. In the vacuum the potential was taken to be the image potential outside a dielectric slab given in Equation 4.40 with a cutoff at 1.3 Å from the layer/vacuum boundary. The dielectric constant was fixed at $\epsilon = 2$, which was calculated from the Clausius-Mossotti equa-

tion using the atomic polarizability of Xe and the density of solid Xe. An illustration of the potential is given in Figure 4.16.

The eigenstates of the model potential were determined by numerical integration as follows. The 2-band NFE solution for the substrate corresponding to an evanescent wave decaying into the metal substrate is evaluated at the substrate/overlayer interface. The slope and value are then propagated numerically through the flat overlayer potential (where the kinetic energy is evaluated using an effective mass of $.57m_e$) and out into the vacuum (where the mass is m_e) using a 4th and 5th order Runge-Kutta integrator with adaptive step sizes. The trial solutions are evaluated at large z for a range of energies to find solutions which are 'well-behaved at infinity', i.e., eigenstates. The accuracy of this numerical technique was verified by comparison to the results obtained by multiple reflection theory [19] for clean Ag(111) using the potential for the clean surface (*i.e.*, zero layers of Xe).

The model was implemented as a set of MATLAB scripts using a Runge-Kutta integrator available in the MATLAB function library. One of the advantages of Runge-Kutta integrators is that they readily handle a variety of boundary conditions such as those imposed by the NFE substrate in the present model. Such flexibility is not generally available in techniques (such as DVR or collocation) that involve basis functions, since the choice of basis function imposes boundary conditions. The scripts are included in Appendix B. The time-independent Schrödinger equation is a second order ordinary differential equation (ODE). Runge-Kutta integrators usually only solve first order differential equations. Fortunately, higher order ODEs can always be reduced to the study of sets of coupled first order differential equations. For example, the general second order equation

$$\frac{d^2y}{dx^2} + q(x)\frac{dy}{dx} = r(x), \tag{4.44}$$

can be rewritten as two first order equations,

$$\frac{dy}{dx} = z(x), \tag{4.45}$$

$$\frac{dz}{dx} = r(x) - q(x)z(x), \tag{4.46}$$

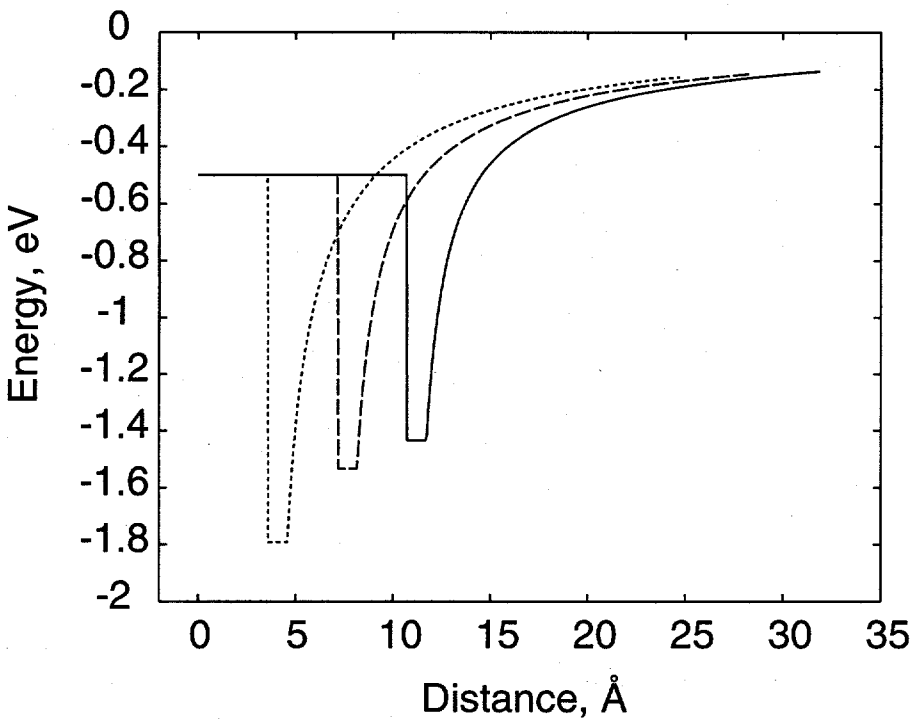

Figure 4.16: Potential used in calculating the quantum well states for 1, 2, and 3 layers of Xe. The potential in the metal is a two-band nearly-free-electron potential. The potential in the layer is set to the Xe conduction band minimum. The potential in the vacuum is the continuum electrostatics solution for an electron outside a dielectric layer on a metal substrate.

where $z(x)$ is an introduced variable. For example, the time-independent Schrödinger equation may be written as a pair of coupled first order differential equations as follows,

$$\frac{dy}{dx} = z(x), \tag{4.47}$$

$$\frac{dz}{dx} = 2m(E - V(x))y(x). \tag{4.48}$$

The determination of eigenvalues can be treated as a two point boundary value problem. In this case, the initial boundary values are the slope $z(x)$ and value $y(x)$ of the wavefunction where the substrate and adlayer meet. The slope and value of the NFE wavefunction are employed. The second boundary condition is that the wavefunction vanish at infinity. This boundary condition can be approximated by requiring that the wavefunction vanish at a large value of x. Solutions to the boundary value problem are typically obtained by employing the numerical method known as the shooting method. The problem was divided into two steps. First, a coarse grid search was used to determine approximate upper and lower bounds on the energy of a bound state. This was performed by numerical solution of the differential equations at several trial energies using a Runge-Kutta integrator. When a sign change in the trial solution at large x was observed between two trial energies, it was assumed that a bound state existed somewhere in the range defined by those two energies. Then a binary search was employed to narrow the range to a set precision.

This model was used to determine binding energies for 1–9 layers of Xe. A cutoff of 1.3 Å in the image potential outside the layer gave the best fit to the data. Binding energies are shown in Figure 4.17 and the corresponding probability densities are shown in Figure 4.18. The binding energies predicted by the model underestimate slightly the $n = 2, 3$ binding energies, but the overall agreement with the data is good. The $n = 2$ probability density possesses a maximum in the Xe layer, whereas the $n = 1$ density exponentially decays within the layer. This is expected since the $n = 2$ state is above the Xe gap and thus the wave function propagates (is plane wave-like) in the layer. However, the $n = 1$ state is in the Xe gap and does not propagate in the layer.

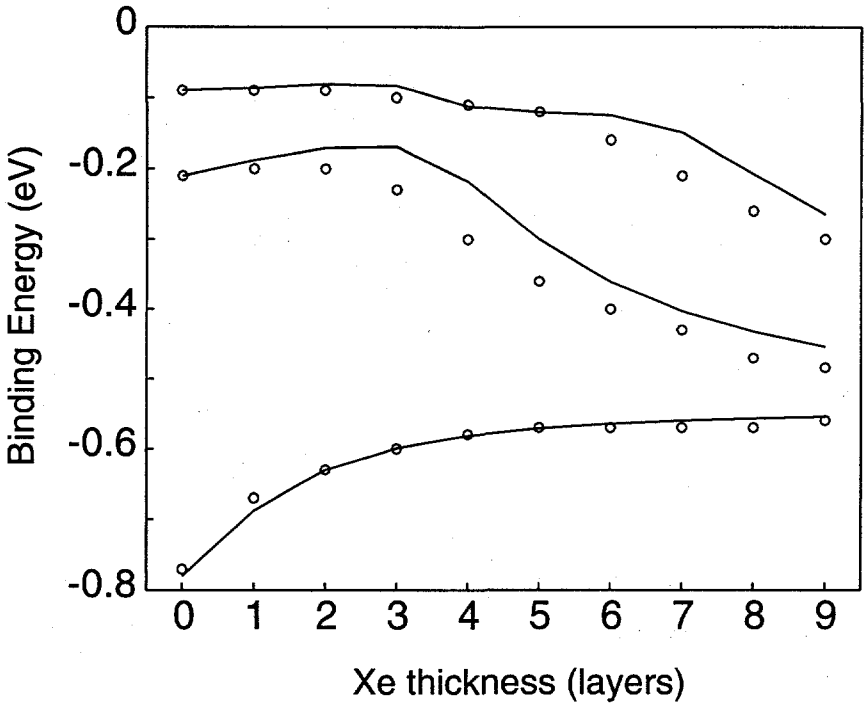

Figure 4.17: Comparison between experimental binding energies for the $n = 1, 2, 3$ states for Xe overlayers (symbols) and the predictions of the quantum well model outlined in this section.

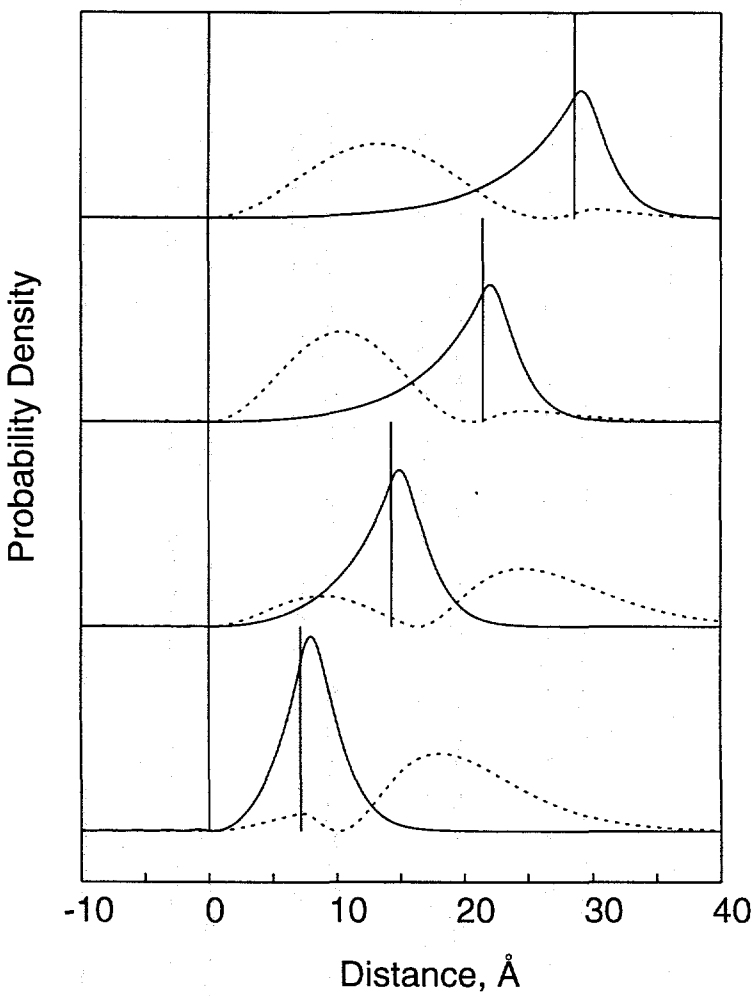

Figure 4.18: Calculated probability densities for the $n = 1, 2$ states for 2,4,6, and 8 layers of Xe/Ag(111) calculated using the model outlined in this section for the case of a Xe layer. The vertical lines indicate the thickness of the Xe layer. The solid line represents the $n = 1$ state and the dashed line represents the $n = 2$ state.

4.3.6 Effective Mass of Quantum Well Electrons

In principle, angle-resolved two photon photoemission measurements of quantum well states yield information about the (bulk) band dispersion of the overlayer material along both the surface parallel and the surface normal. As discussed in the previous section, normal photoemission from quantum well states has been shown to yield precise band structure information along the direction normal to the surface. The coverage dependence of the parallel dispersion (shown in Figures 4.10 and 4.12) along one or more axes of the surface Brillouin zone yields additional information about the full 3D band structure, expanding the amount of information obtainable by photoemission considerably. However, the interpretation of coverage dependent parallel dispersion measurements thin layer quantum well is complex in that the dispersion of quantum well states is determined by several effects including the layer band structure, the substrate band structure and by the probability amplitude of the quantum well state in the substrate, overlayer, and vacuum regions. Here the combined effects of the the band structure of the substrate and overlayer as well as the probability amplitude in the various regions which together determine the quantum well effective mass are explored.

Since the present interest is in describing the electronic states within a substrate gap, the NFE model is a natural starting point. We shall also assume that all the measurements are near zone center of the surface Brillouin zone in which case two-bands are sufficient to describe the dispersion. The geometric theory of Giesen and coworkers [18] (outlined in Section 4.1.2) for the effective mass of image states on the clean surface of noble metals is useful as an example of a successful theory upon which more sophisticated theories for more complex systems may be built. Indeed, the effective mass model for a thin alkali metal layer (Section 4.1) is based largely on the geometric model. The model for the alkali layer replaces the conduction band edge with a $\phi_c = \pi$ curve which contains both substrate and overlayer effects.

The success of the geometric theory owes to the fact that it more or less correctly partitions the effective mass between the substrate, where the effective mass is related to the valence and conduction band dispersions, and the vacuum, where the effective

mass is that of a free electron. It should be noted that the theory is only applicable for surface states which are close in energy to either the conduction or valence band edge. The results are ambiguous in the middle of the gap, where it is not known which band the image state will eventually cross. This ambiguity relates fact that the derivation is geometric instead of algebraic, and relies on the fact that the crystal phase shift ϕ_c is π at the point along $k_{||}$ where the image state crosses the conduction or valence band. Obviously, this ambiguity is not a feature of the underlying physics, but rather a weakness in the model. An additional complication in the case of a dielectric layer is the fact that the potential outside the layer is not the hydrogenic image potential. This makes phase shift analysis impractical. Instead, the approach taken is to include a dependence on $k_{||}$ in the substrate and overlayer band parameters, as was done for the case of alkali metal layers in Section 4.1.2. In addition, the $k_{||}$ dependence of the image potential is included, and eigenstates are determined (as explained in Section 4.3.5) for a range of $k_{||}$ values, thus determining the dispersion. Calculations of phase shifts are not necessary in this approach.

The details of the calculations are as follows. As in Section 4.1.2, the substrate band gap energy E_g and half width V_g are parameterized with respect to $k_{||}$ in order to account for the changes in gap width and energy as a function of $k_{||}$ in the surface projected bulk band structure (for an illustration of the surface projected bulk band structure, see Figure 2.4). The perpendicular component of the kinetic energy in the overlayer and vacuum regions is also parameterized in $k_{||}$. Assuming the Hamiltonian for the system is roughly separable into perpendicular and parallel components, the total kinetic energy can be written as the sum of the perpendicular and parallel components. In the overlayer, the effective mass approximation with effective mass parameter m_L^* is used to account for the band dispersion of the overlayer material, resulting in an expression for perpendicular kinetic energy,

$$E_\perp = E - V = E - V_L - \frac{\hbar^2 k_{||}^2}{2m_L^*}, \tag{4.49}$$

where V_L is the conduction band minimum of the layer. In the vacuum, a similar expression is used for the perpendicular component of the kinetic energy, except the

Layers	Effective Mass			
	$n = 1$		$n = 2$	
	expt.	theo.	expt.	theo.
1	0.96	0.91	1.09	0.98
2	0.78	0.79	0.94	0.96
3	0.63	0.72	0.77	0.93
4	0.63	0.67	0.69	0.80

Table 4.2: Measured effective mass of the $n = 1$ and $n = 2$ image-like states for 1–4 layers of Xe on an Ag(111) substrate and a comparison to calculated results.

mass employed is the free electron mass,

$$E_{\perp}(z) = E - V_{im}(z) - \frac{\hbar^2 k_{||}^2}{2m_e}, \tag{4.50}$$

where $V_{im}(z)$ is the image potential taken from the dielectric continuum model. The effective mass of the thin layer quantum well state is determined by finding binding energies for a few given values of $k_{||}$ and fitting the results to a parabola. The effective masses for 1–4 layers of Xe were calculated using version of the program included in Appendix B which was modified to take into account $k_{||}$ in the manner described above. The results of the calculation are plotted together with the experimental results in Figure 4.19. A table of experimental and calculated values is given in Table 4.2.

The theory follows the overall trends in the data, including the fact that $n = 2$ has a larger effective mass than $n = 1$, but seems to underestimate the effect of the layer in lowering the effective mass. Perhaps this is a result of using an effective mass of $0.57m_e$, taken from a simplistic interpretation of the TPPE data, instead of the literature value of $0.35m_e$. However, even in calculations performed with the lower effective mass, the effective mass is somewhat larger than experiment. Perhaps this indicates that the model does not calculate overlap with the layer as well as would be believed considering the success of the model for binding energies at $k_{||} = 0$. Indeed, this discrepancy indicates that effective mass measurements may be more sensitive to the spatial extent of the electron than binding energy measurements. It should be noted that uncertainty estimates for the effective mass measurements

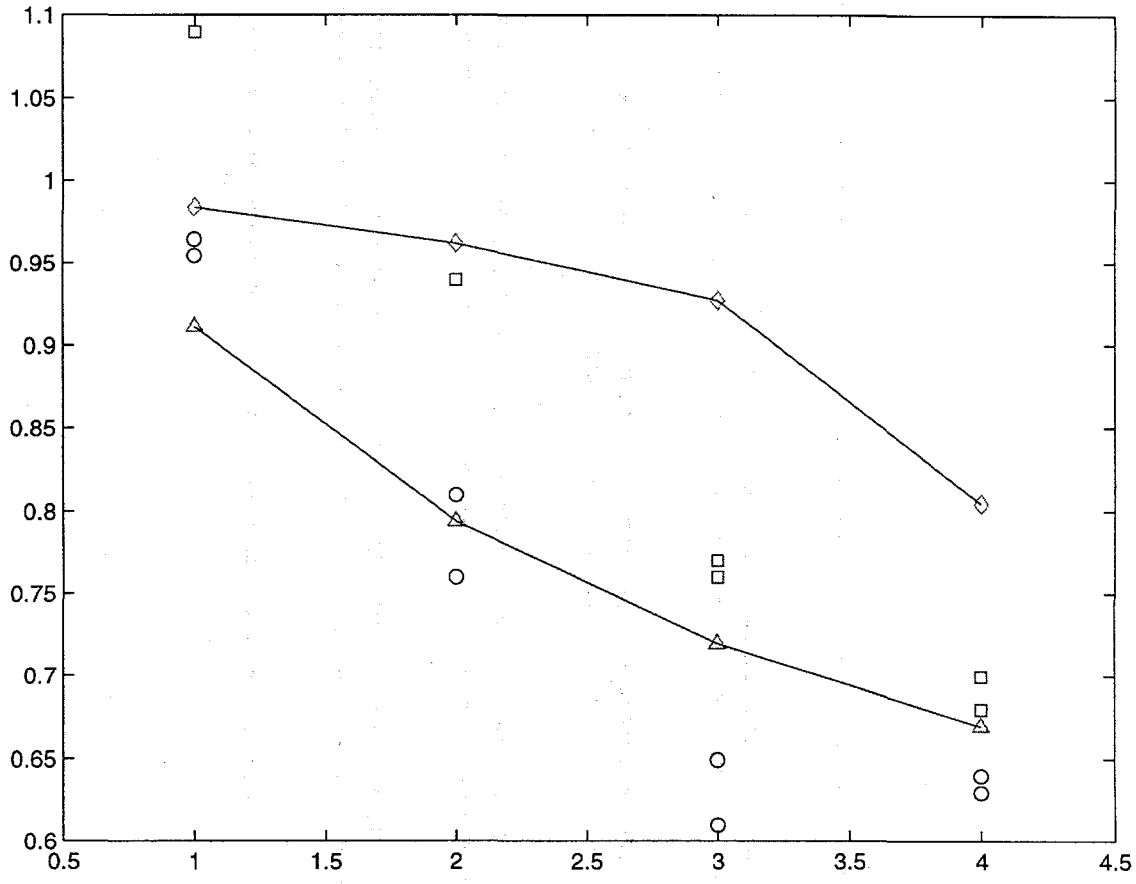

Figure 4.19: The effective mass as a function of Xe coverage. Circles and squares indicate the calculated effective mass of the $n = 1$ and $n = 2$ states, respectively. Triangles and diamonds indicate experimental values of the effective mass of the $n = 1$ and $n = 2$ states.

were not obtained, so a quantitative evaluation of model correctness is not possible. The n=2 dispersion measurements for monolayer and bilayer Xe suffered from low signal levels. In addition, it is possible that the photon energy was not sufficient for accurate measurement of n=2 at 1ML. The success of the effective mass model in reproducing the data indicates that angle-resolved TPPE measurements of thin layers of material together with the model presented here can be a useful method for obtaining momentum-resolved 3D band structure measurements of unoccupied bands.

4.3.7 Discussion

The coverage dependent spectra exhibited several types of behavior which we attribute to image states, quantum well states, and "mixed" states. The $n = 1$ state behaves as a screened image state of the composite metal/dielectric interface at intermediate Xe coverage. On the other hand, the $n = 2, 3$ image states become quantum well states of the overlayer at 7+ layers of Xe and exhibit a coverage dependence between that expected for image and quantum well states for 3–6 layers. An important difference between image states and quantum well states is that image states are energetically within the Xe gap while quantum well states are energetically within the Xe conduction band. Based on this distinction the $n = 1$ state, which is below the Xe conduction band in energy, is an image state while the $n = 2, 3$ states are quantum well states. The image state binding energy depends largely on the electrostatics of the insulator/vacuum interface, while the energy of the quantum well states depends on the perpendicular dispersion and the minimum of the Xe conduction band.

The results of the dielectric continuum model of Section 4.3.3 indicate that the $n = 1$ state moves to more positive binding energy (weaker binding) due to the dielectric polarization of the Xe slab in the presence of the image potential electron. This is a combination of two competing effects. First, the polarizable Xe adlayer, characterized by dielectric constant ϵ, serves to screen the image electric field between the electron and the metal, leading to a more positive binding energy. Screening is

primarily due to the first term in Equation 4.36 and the first term in Equation 4.40. Second, the induced polarization interaction between the electron and the Xe slab, represented by the second term in Equation 4.40, is attractive and favors a more negative binding energy. This model correctly predicts that the net effect for the $n = 1$ state is weaker binding to the interface as each of the first five or six layers is added (Figure 4.11), which results in a shift of electron density toward the Xe/vacuum interface. This reduction in binding energy is manifest in this model for any case where the affinity of the layer is repulsive with respect to the $n = 1$ binding energy. For states above the affinity level in the layer, the state "falls into" the layer at some thickness. The fact that the affinity level (Xe conduction band minimum) falls between the $n = 1$ and $n = 2$ energies distinguishes the coverage dependent behavior of the two states.

The relative intensities (Figure 4.9) of the peaks as a function of Xe coverage give additional evidence as to the nature of the states. The linewidths would also be important but were difficult to determine due to overlapping features. Photoemission from the $n = 1$ state becomes reduced in intensity relative to that from the $n = 2, 3$ states for 3 and 4 layers of Xe, but is similar in intensity for 6–8 layers of Xe. This is consistent with our assignment of the $n = 1$ state to an image state of the Xe layer, primarily located at the vacuum/Xe interface. The intensity of this feature may be determined by two competing effects related to the location of the $n = 1$ state at the layer/vacuum interface. The initial decrease in intensity may be due to the fact that the probability of excitation of a substrate electron into the $n = 1$ state becomes lower as a function of coverage since the state is located relatively far from the initial states in the metal making the spatial overlap with the bulk states small. Similarly, the increase in relative intensity at 6–8 layers is likely due to an increase in the lifetime of the $n = 1$ state. The lifetime increase is due to the fact that the electron must tunnel though a thicker layer in order to decay into the metal.

The $n = 2, 3$ states at higher coverage possess a perpendicular dispersion similar to accepted Xe conduction band values as shown in Figure 4.15. The influence of the Xe conduction band can also be seen in the angle-resolved data (Figure 4.12), where the dispersion is measured along the surface parallel while the perpendicular

momentum is fixed by the layer thickness. The effective masses measured along the surface parallel are higher than accepted bulk Xe conduction band values because for the first few layers a significant fraction of the probability density of the states is in the metal and in the vacuum which results in a larger effective mass. The effective mass for the $n = 1$ image state on a clean Ag(111) surface (corresponding to the limiting case of a state where all the probability density is outside the layer) is $1.3m_e$. The parallel dispersion of the $n = 1$ state corresponds to an effective mass close to that of a free electron for the monolayer ($m^*/m_e = 0.95$) and the effective mass monotonically decreases to $m^*/m_e = .6$ at four layers. Also apparent from Figure 4.12 is that, for a given layer thickness, the $n = 1$ state has a lower effective mass (closer to the bulk Xe value of $.35m_e$) than that of the $n = 2$ state. This may be due to differences in the spatial overlap of the states with the substrate and overlayer. According to the calculations in Section 4.3.5 the $n = 2$ state has a higher probability density in the metal than $n = 1$ which should increase the effective mass with respect to $n = 1$. In looking at the wave functions for two and four layers (Figure 4.18), one can see that for up to four layers the $n = 1$ state has more density in the layer than the $n = 2$ state. Model calculations of the effective mass reproduce the trends seen in the data and demonstrate the usefulness of the combined angle-resolved and coverage-resolved TPPE in determining 3D band structure of the overlayer material. The calculations also suggest that the effective mass is quite sensitive to spatial extent of the electron.

It should be noted that the high energy and momentum resolution afforded by this technique along both the surface parallel and surface normal yield the most precise, detailed spectra to date of the Xe conduction band. Angle-resolved UPS of a bulk single crystal conducted at a variety of wavelengths can also map out the conduction band structure, but UPS resolution is ultimately limited by hole lifetime effects and the fact that k_z is only partially conserved in photoemission from bulk material. The precision of the TPPE measurements of the conduction band is in principle only limited by the lifetime broadening of the conduction band of the overlayer.

The QW treatment of Section 4.3.5 has the appropriate behavior in the limiting cases of zero and infinite Xe layers. The model reduces to the multiple reflection

model for the clean surface in the limit of zero coverage. In the limit of high coverage, the model reduces to the effective mass approximation of the Xe conduction band. It also appears to adequately describe the data in the intermediate case of 1–9 layers. The probability density of the wave functions in Figure 4.18 indicates that for two Xe layers approximately 5% of the $n = 2$ wave function is in the layer whereas for 8 atomic layers of Xe approximately 95% of the wave function is in the layer. This model is perhaps successful because it partitions the wave function more or less correctly between the layer, vacuum, and substrate, allowing the substrate and vacuum parts of the potential to primarily determine the $n = 2, 3$ binding energy for the first few layers but allowing the overlayer potential to dominate for thicker layers.

Merry and coworkers [96] discussed the effect of the work function shift due to adsorption on the image state binding energy. In the application of this model, the work function shift of $-.5$ eV was taken into account. Therefore this effect of the substrate band structure is explicitly accounted for in this model, allowing for a comparison of the relative importance of the work function shift, the dielectric properties of the interface, and the band structure of the layer.

The binding energies and effective masses of the excited states of the Xe/Ag(111) interface within an electron-Volt below the vacuum level have been measured using ARTPPE for one to nine atomic layers. Purely 2-D image potential states (which only propagate freely in the plane of the surface) evolve into quantum well states that converge to the conduction band states of the 3-D bulk xenon solid with increasing layer thickness. This work demonstrates that ARTPPE is a powerful technique for studying the transition from two- to three-dimensional electronic structure at nanometer scale interfaces. The simple QW model outlined in Section 4.3.5 accounts for the energies of the $n = 1, 2, 3$ states over the range of coverages examined in this work. Importantly, the model yields a simple method for determining an accurate conduction band structure from the experimental data. In the following section, the lifetimes of the Xe QW states are investigated.

4.4 Ultrafast Dynamics of Xe QW States

The culmination of the present work is the determination of the ultrafast decay kinetics for electrons in quantum well states of the Xe layer. Portions of this section are adapted from previously published work [128]. The population decay kinetics were determined from one to six layers of Xe. These results represent the first time-resolved measurement of the evolution from image states into quantum well states. These results are important because the transition of the electronic structure from two-dimensional atomically thin layers to the three-dimensional extended electronic structure of the bulk has implications in many fields including surface photochemistry, photoinduced charge transfer, and semiconductor device physics. Both surface effects, including chemisorption, band-bending, surface reconstructions, and image potential states, and quantum confinement, which results in the discretization of momentum along the surface normal, may affect the electronic characteristics (energies, dispersions, and transport properties) of the composite interface. Femtosecond time-resolved two-photon photoemission (TRTPPE) has proved to be a useful technique for the determination of the energies and dynamics of interfacial electronic states for a variety of systems [21,129] including metal surfaces [130], semiconductor surfaces [131,132], and metal-insulator interfaces [40,118]. This approach represents a new and general method for determining the evolution of electronic structure from two-dimensional states of a single atomic layer to three-dimensional quantum well states by analysis of the femtosecond dynamics of excited electronic states for a range of layer thicknesses. Such a study has the potential of providing a measure of the spatial distribution of the electron at the interface and the thickness dependence of the spatial distribution as well as the transport properties across the insulator and the metal/insulator heterojunction.

Physisorbed multilayers of Xe on a noble metal surface [85, 86, 108] have been identified as an important model system for understanding carrier dynamics at interfaces and in quantum wells. Since solid Xe is electronically similar to SiO_2, aspects of this model system are similar to those of a metal-oxide-semiconductor junction. Because the crystal and electronic structures of bulk Xe and Ag are experimen-

tally [133, 134] and theoretically [135] well-characterized, models of the composite interface electronic structure and dynamics can be constructed and tested. Of fundamental importance to understanding electron behavior in quantum wells and at interfaces are the time scales and mechanisms for energy and momentum relaxation of carriers near the junction of two materials. A systematic study over a range of film thicknesses provides a unique probe of the interface since the evolution of the electronic structure can be monitored atomic layer by layer, allowing for the separation of the various factors which determine the electronic structure and dynamics of the composite interface.

The evolution of an $n = 1$ image potential state into a QW state has been observed by Fischer *et al.* [26] for Au/Pd(111). In the previous section it was determined that conduction band QW states can form with increasing layer thickness for an insulating overlayer such as Xe which has a positive (attractive) electron affinity [108]. The energy levels of excess electrons in these states were measured, and it was shown that the binding energies were quantized according to the layer thickness. It was also demonstrated that the quantized energy levels were in good agreement with the Xe conduction band dispersion. Here, these measurements are extended to the time domain, providing the first direct (time domain) measurement of the lifetime of QW states at a metal–insulator interface. It is shown that the lifetime provides a measure of the spatial distribution of the electron at the interface and thickness dependence of the spatial distribution as well as the transport properties across the insulator and the metal/insulator heterojunction.

In general, the electronic states of the interface depend on contributions from the electronic structure of the substrate, the overlayer material, polarization or image effects, and quantum confinement effects. As shown below, all of these effects are important in Xe/Ag(111). QW states occur in a layered sample when the states of one material are confined by band gaps in the neighboring layers. The relevant bulk bands of the materials under study are the surface-projected Ag(111) valence and conduction bands (VB and CB, respectively) and the Xe 6S CB (Figure 4.8). In addition, the polarizability of the metal surface supports a Rydberg series of image potential bound states converging to the vacuum level. The lowest members of that

series are also plotted in Figure 4.8. The work function shifts for monolayer and bilayer were determined from the kinetic energy of the $n = 3$ feature [108]. The work function shift of $\Delta\Phi = -0.5$ eV due to the adsorption of monolayer Xe places the vacuum level at approximately 0.07 eV above the Ag CB minimum. The Xe CB minimum is at approximately -0.5 eV with respect to the vacuum level. Electrons promoted to the CB of a Xe slab on the surface will be subject to confinement by the projected band gap in the metal and the image potential in the vacuum. Previous work has shown that the manner in which an image state evolves with coverage depends on its energy relative to the band structure of the Xe slab. The $n = 2$ and 3 image states, which are above the Xe CB minimum, become QW states of the layer at 7–9 layers of Xe and exhibit a mixed QW–image state behavior at intermediate coverage. These exhibit a discrete perpendicular dispersion corresponding to the Xe CB, whereas $n = 1$ does not [108].

The details of the experimental apparatus are described previously. Only the experimental parameters which are specific to this experiment are described here. A Coherent Ti:sapphire oscillator–regenerative amplifier system in conjunction with the optical parametric amplifier is employed to generate 70 fs visible pulses which are frequency-doubled to yield UV pump pulses. The residual fundamental is used as a probe pulse and is optically delayed with respect to the pump pulse. The two pulses are focussed collinearly on the sample. The energy of the photoemitted electrons is determined by time-of-flight. Using 300 and 600 nm pulses as pump and probe, the measured instrument function is $\sim$ 110 fs FWHM. The wavelength was selected to place the pump photon energy (4.13 eV) close to the vacuum level but to avoid producing excess background counts from one photon photoemission. The sample was cooled to 45 K by means of a liquid helium cryostat in the UHV chamber with background pressure at $\sim 1 \times 10^{-10}$ torr. Xe was adsorbed on the sample by Langmuir dosing using a leak valve. Xe/Ag(111) X-ray structure results [114] show Xe to form an ordered incommensurate hexagonal layer on the Ag(111) surface.

A time-resolved spectrum of the clean Ag(111) surface state was taken before deposition, in order to calibrate time zero on the delay stage, to determine the instrument function width, and to determine the $n = 1$ clean surface lifetime as a

sanity check for the system. Time-resolved TPPE spectra were acquired for each of one to six layers of Xe. The $n = 1$ and $n = 2$ traces correspond to an exponential rise and decay convolved with a Gaussian instrument function, as shown in Figure 4.20. The $n = 1$ lifetime increases monotonically with each additional layer of Xe while the lifetime of the $n = 2$ state initially increases with the addition of a monolayer of Xe, decreases slightly at 3 layers, then increases again at five and six layers (Figure 4.20). The $n = 3$ state lifetime possesses a similar oscillation at three layers and remains approximately constant from five to six layers, suggesting a second oscillation.

4.4.1 Quantum Well Model Estimates of Lifetimes

In order to quantify the possible contributions to the binding energies of the image potential and QW states, a 1D quantum-mechanical model which explicitly includes the polarizability of the metal substrate and adlayer as well as the substrate and adlayer band structure is used [108]. As shown in the previous section, the model results are in good agreement with experimental binding energies. Implicit in this model is the quantum confinement due to the band gap of the substrate and the image potential barrier in the vacuum. As is shown below, a simple extension yields lifetime predictions for Xe QW states based on wavefunction penetration into the substrate. The Ag(111) substrate bands are treated within the two-band nearly free electron (NFE) approximation. The two band NFE approximation was chosen since it had been successfully applied [61] to describe the substrate for the related case of surface states in the band gap of a metal. The two-band parameters were taken from calculations of clean Ag image and surface state binding energies [62]. In the overlayer the potential was set to the Xe CB minimum of -0.5 eV with an effective mass of $0.55m_e$. In the vacuum the potential was taken from the continuum dielectric model [118, 120]. The continuum dielectric model yields the image potential outside a dielectric slab on a metal surface, accounting for the polarizability of the metal and adlayer. The dielectric constant of the layer was set to the literature value [136] of $\epsilon = 2$. The eigenstates of the model potential were determined by numerical integration, and binding energies and wavefunctions were determined for 1–10 layers

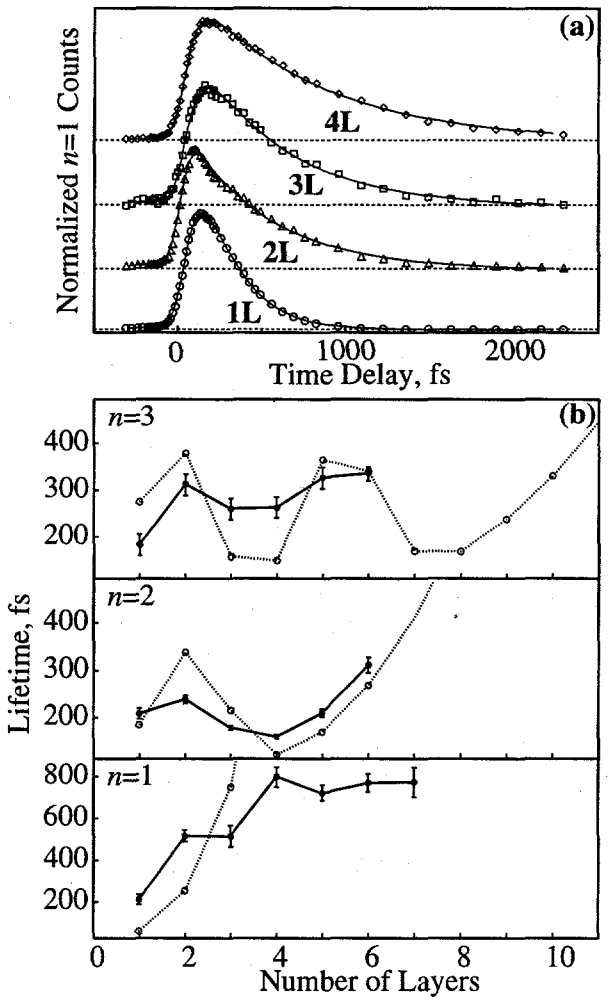

Figure 4.20: Ultrafast time-resolved two-photon photoemission traces (a) for the $n = 1$ state for one to four layers of Xe (symbols) along with a fit obtained by convolving a single exponential with a Gaussian instrument function. Lifetimes (b) of the $n = 1, 2$ and 3 states for 1–6 layers of Xe extracted from the time-resolved data (filled circles). Lifetime predictions taken from the 1-D model (open circles) are in qualitative agreement with the oscillations in lifetime apparent in the data. The experimental error bars are calculated for a 95% confidence limit.

of Xe. The probability densities are shown in Figure 4.21.

Lifetime predictions were obtained from this model as follows. Since Xe has a large gap, it can be assumed that very few decay channels are present within the Xe layer, and therefore the primary decay pathway for excited electrons at the Xe/Ag(111) interface is recombination with a vacancy in the substrate. Based on this assumption, the lifetime should depend on wavefunction overlap with the substrate. A model which has proven successful in obtaining qualitative lifetime predictions from calculated wavefunctions starts by assuming that the coupling to the crystal is related to the penetration p of the image state into the bulk, where p is defined as the probability density in the bulk [69, 72–74],

$$p = \int_{-\infty}^{0} \psi^* \psi dz. \tag{4.51}$$

The lifetime broadening Γ of the image state is related to the linewidth of the bulk crystal conduction band $\Gamma_b(E)$ by $p \cdot \Gamma_b(E)$. Calculated lifetimes using a value of Γ_b based directly on independent photoemission data [75] are shown in Figure 4.20. The value of Γ_b at a given energy is given by an expression obtained by empirically fitting photoemission and inverse photoemission linewidths over a range of 2 to 50 eV,

$$\Gamma_b(E) = 0.13(E - E_f). \tag{4.52}$$

The $n = 1$ state is at -0.77 eV, or 3.79 eV above E_f. This yields a Γ_b of 490 meV.

The trends and overall magnitudes of the $n = 2$ and 3 lifetimes are reproduced by this simple model. These trends can be understood by considering two effects which have an opposite impact on lifetime. First, the semi-classical round trip time in a simple square well varies as the width squared. Assuming the lifetime is inversely proportional to the attempt rate, the lifetime should increase as the square of the number of layers. The second effect is due to the presence of the soft image barrier in the vacuum: For a monolayer, the image potential well in the vacuum is both wider and deeper than that of the layer. As the layer thickness increases, the increased distance from the metal substrate weakens the image potential in the vacuum while the layer potential gets wider. At a certain thickness, approximately when the Xe layer terminates near a node in the zero-order image state wavefunction, it is energetically

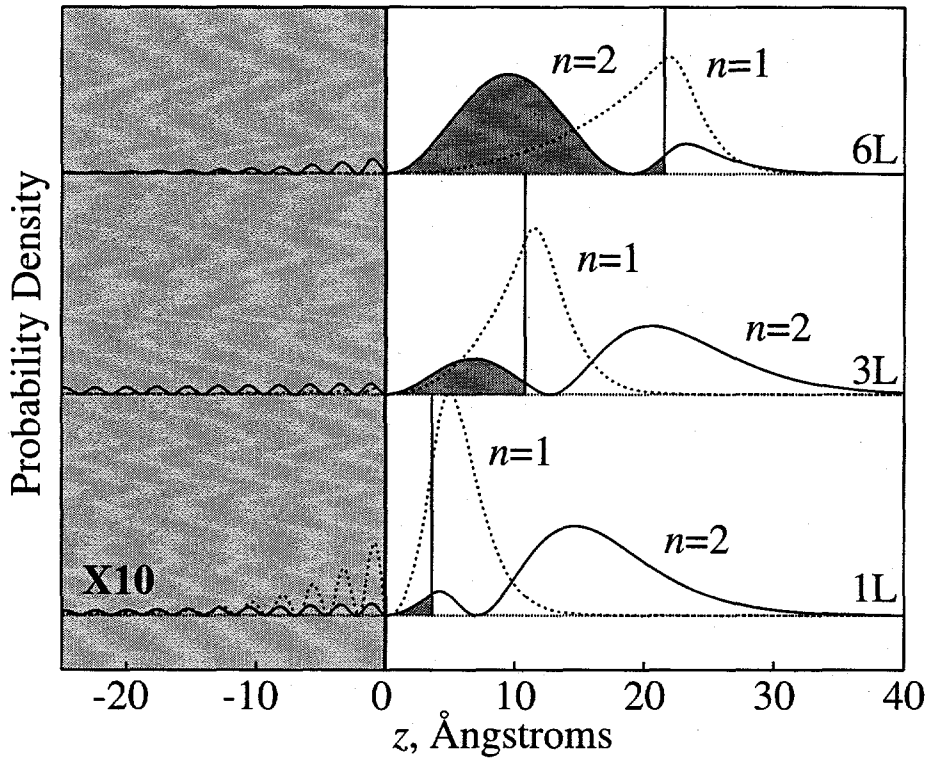

Figure 4.21: The electron probability density $\psi^*\psi$ for the quantum well model for the $n = 1$ and 2 states for 1,3, and 6 layers of Xe. The model predicts that the probability density in the layer increases for the $n = 2$ state as the number of layers increases. The vertical lines represent the layer–vacuum boundary.

favorable for the electron to move inside the layer, resulting in increased probability density in the layer, as can be seen by comparing the $n = 2$ wavefunction for one and three layers (Figure 4.21). The expectation value $\langle z \rangle$ decreases, resulting in an increase in the probability density in the substrate which reduces the lifetime. A given image potential state effectively becomes a QW state in successive steps, the number of which is determined by the number of nodes in the zero-order hydrogenic wavefunction, *i.e.*, the quantum number. For example, the calculations indicate that $n = 3$, having two nodes in the wavefunction, will have two oscillations in lifetime before the simple square well behavior takes over.

Degeneracy of the image state with the substrate conduction band results in a decrease in lifetime relative to image states within the gap [130]. The fact that the lifetime of the $n = 3$ state in the presence of a monolayer of Xe is shorter (the lifetimes for $n = 1, 2$ and 3 are 210, 210, and 180 fs, respectively) than that of $n = 1$ and $n = 2$ could be explained in terms of the degeneracy of the $n = 3$ state with the bulk. However, for the similar case of a monolayer of cyclohexane (C_6H_{12}) on Ag(111), the lifetimes of the $n = 1, 2$ and 3 states are 200, 220, and 660 fs. The work function of Xe/Ag(111) is 30 meV lower than the value of 4.09 eV measured for cyclohexane on the same substrate, placing the $n = 3$ state in the presence of a Xe monolayer within the band gap, according to previous measurements of the Ag(111) band gap [26]. That the $n = 3$ lifetime in the presence of a monolayer of Xe is shorter than that of the $n = 3$ state in the presence of a monolayer of cyclohexane despite the fact that the former is within the band gap of the substrate rules out degeneracy as the cause of the difference in lifetime. Rather, this suggests that the difference in lifetime is due to differences in the potential within the layer. The main difference is that the alkanes possess a negative (repulsive) electron affinity, which prohibits the formation of quantum well states. No oscillations are observed or predicted in the lifetime for n-heptane/Ag(111) as a function of coverage. The lifetimes increase monotonically, consistent with a picture in which the negative electron affinity excludes the electron from the layer. In contrast, appreciable electron density in the layer and the formation of quantum well states related to the band structure are observed for Xe layers [108].

The model results for the $n = 1$ state predict that its lifetime should also increase quadratically with layer thickness. This conflicts with the data, which indicate that the lifetimes for $n = 1$ reach limiting values by five or six layers. A possible interpretation is that the $n = 1$ state ceases to evolve as an image state at the Xe–vacuum interface [108] and becomes a screened image state of the metal inside the Xe slab. The finite lifetime of an electron in bulk Xe, which may have an effect on measured lifetimes, is not taken into account. Also, for thicker layers defects and the presence of islands of adsorbate instead of continuous layer may shorten the lifetime. In order to determine the relative importance of these effects, a more sophisticated, self-consistent approach to the potential in the overlayer is required. Recently, sophisticated self-consistent pseudopotential calculations of image state lifetimes on Li, Cu, and Ag surfaces were reported [53]. The results of those calculations point to the importance of nonlocal effects (correlation) on image state lifetimes. Interestingly, the results of empirical multiple reflection theory calculations compare favorably with the pseudopotential calculations, which mirror recent experimental results. When nonlocal effects are left out of the pseudopotential calculations, the lifetime of the image states is overestimated. The nonlocal effects are important to the lifetime, since they include the interaction of electrons in the vacuum with electrons in the metal. It should be noted that nonlocal effects are implicit (but approximate) in the multiple reflection formalism, which assumes delocalized Bloch waves in the substrate. Multiple reflection theory also approximates the important many body effects by including the image potential. An interesting question is what effect the overlayer has on the importance of nonlocal effects. Unfortunately, the self-consistent pseudopotential model could not be readily adapted for the current system, due to the large number of electrons in the Xe and the difficulty in handling relativistic effects.

Since the calculated wavefunctions successfully account for the lifetimes of the quantum well states, we conclude that the wavefunctions correctly describe the partitioning of conduction electrons between the three spatial regions of this model interface, *i.e.*, between a noble metal, an insulator, and vacuum, as illustrated in Figure 4.21. In addition, we have shown that the electron lifetime as a function of thickness displays a characteristic oscillation marking the onset of QW electronic

behavior. Femtosecond layer-by-layer TPPE constitutes a new approach to understanding the complex dynamics of electrons at interfaces leading to stringent tests for electronic structure theory and dynamics.

Chapter 5

Conclusions

In the present work, the binding energies and dynamics of excited electronic levels in thin layer quantum wells have been determined by the technique of two photon photoemission. The results have been interpreted in terms of the bulk electronic properties of the Xe adsorbate, through the conduction band minimum and effective mass as well as the dielectric constant. The layer-by-layer data show a pronounced effect of coverage on binding energy and lifetimes of excited electronic states. Individual, well-separated peaks in the energy spectrum were associated with each coverage. This indicated complete layers at the monolayer through trilayer coverages and large, ordered islands at higher coverages from 6–9 layers. The individual peaks at each coverage were shown to possess a dispersion which also depended on coverage. The lifetimes of the excited electrons exhibited oscillations as a function of coverage.

These effects were interpreted in terms of fundamental physical properties of the overlayer material and the substrate, and yielded precise information about the electronic structure of the overlayers and the spatial extent of overlayer electronic states. At low coverages, the excited electrons were shown to reside primarily outside the layer and the binding energies of the image states are determined largely by the polarizability of the layer and substrate. The polarizability of the adsorbate and substrate was modeled using a dielectric continuum approximation. At higher coverages, the electrons overlap significantly with the Xe overlayer and the coverage dependence of the binding energies was explained in terms of a quantum size effect

which was shown to yield the perpendicular dispersion of the Xe conduction band, described by a band minimum and effective mass. The dispersion within the plane of the surface was qualitatively explained in terms of the bulk Xe effective mass and the probability density of the excited electron within the layer.

It was shown that the affinity level of the overlayer material is important in determining the coverage-dependent behavior of the states. For electronic states initially energetically below the bulk affinity level of the layer material, the layer acts as a barrier and the electron is pushed further out into the vacuum with each additional layer. For these states, the electron resides primarily in the image well outside the layer. The image well outside the layer has contributions from the polarizability of the layer as well as contributions from the substrate image potential. The layer polarizability term $1/4\epsilon z$ dominates the potential at high coverage. For states initially energetically above the layer affinity level, the layer presents an attractive quantum well. For very thin layers, however, the confinement energy of the layer makes it energetically unfavorable for the electron to reside in the layer. The lifetimes of the excited quantum well states possess a significant oscillation or decrease in lifetime as a function of coverage which was interpreted as marking the onset of quantum well electronic behavior. The results were modeled quantitatively in terms of a penetration model which confirmed the experimentally observed oscillations in lifetime are a result to the onset of quantum well electronic behavior, as the decrease in lifetime was accompanied by a substantial increase in the probability amplitude in the layer. Thus the difference in the coverage dependence of the lifetimes for the $n = 1$ state versus the $n = 2$ and 3 states can be interpreted as a measure of the way the spatial extent changes as the coverage increases.

The models which were developed to interpret these results were based on the multiple reflection theory for image states on metal surfaces. The effect of the overlayer was modeled by modifying the image potential in the vacuum to take into account the presence of the layer. Inside the layer the potential was that of a one dimensional box, with the potential set to the minimum of the bulk conduction band of the overlayer material. On the substrate side, the wavefunction solutions of the box were joined with the nearly-free electron solutions of the bulk. On the vacuum side,

the wavefunctions were joined to solutions for the image potential, which contains contributions from the layer polarizability as well as the substrate image potential. The calculation results underlined the importance of the substrate band structure in the lifetime in some cases. For states near the substrate band edge, small changes in the energy of the state or the position of the vacuum level result in large changes in the penetration into the substrate. Wavefunction penetration into the substrate is directly related to the inverse lifetime.

It was also shown that the TPPE results provide a sensitive measure of the dispersion or effective mass of the relevant electronic bands of the overlayer material. The coverage dependence of the binding energies yields a measure of the overlayer band dispersion along the surface normal while angle-resolved measurements yield information about the dispersion along the surface parallel. The interpretation of the dispersion data is somewhat complicated by the presence of the substrate bands, but this effect can be modeled reasonably well using the quantum well model developed.

An important development in this research was the realization of the significance of coherence and dephasing in the time-resolved spectra. The lineshapes of TPPE features along both the energy axis and the time axis are affected by the coherence dephasing process. Coherence dephasing results in a delayed rise in the population of the excited state, a feature observed in many spectra. The delayed rise time is associated with the coherence dephasing time. The energy peaks in the spectrum are experimentally observed to narrow as a function of pump-probe delay. In the past, it has been difficult to model coherence dephasing in time-resolved TPPE spectroscopy because of the large number of parameters to determine given a single kinetics trace. But since the TOF spectrometer allows us to obtain a complete, high resolution energy spectrum at each time delay, the size of the data set is greatly increased. The determination of the dephasing parameters of the optical Bloch equations for the system by the application of non-linear least squares minimization on the complete three-dimensional data set should yield more information than is currently available about the various decay processes of electrons at surfaces. Ideally, such a determination should yield additional information about the relative contributions from the various processes involved in dephasing: pure dephasing, electron-electron scatter-

ing, defect scattering, and momentum relaxation. Proper analysis of the results can yield information about hole state lifetimes, as well.

The relatively long dephasing times open up the possibility of phase-locked multiple pulse experiments yielding multidimensional data sets roughly analogous to 2D NMR results. This also opens up the possibility of quantum control of electrons and chemical reactions on surfaces. The surface provides a way to align molecules, and provides a straightforward method for cooling them. Cold, well-aligned molecules are important for quantum control, since pure populations are required in order for quantum-mechanical interference effects to be manifest. Also, the enhanced surface sensitivity of techniques such as TPPE allows the measure of subtle effects or processes with low cross-sections.

Another possible area of study for future work is the excitation mechanism for negative ions at surfaces. There has been a lot of work published recently which assumes the importance of a hot electron distribution in the formation of dissociative and non-dissociative negative ion states at surfaces [137,138]. The qualitative picture that has emerged is: absorption of one or more photons in the bulk near the surface excites one or more electrons. The electron or electrons quickly exchange energy with other electrons resulting in a thermalized hot electron distribution. There is then electron transport which carries a number of these hot electrons to the surface where they attach to adsorbate molecules.

There is a different possible scenario: direct excitation from bulk-like or surface electronic states to negative ion states of the adsorbate. The distinction is not merely semantical, as the photon energy and polarization dependence for the two mechanisms should be distinct. In particular, direct excitation is favored for adsorbates with an electron affinity level nearer the vacuum level, since hot electron lifetimes at this energy are very short, making transport from the bulk to the surface quite inefficient.

It should be straightforward, in principle, to study the relative importance of the hot electron-mediated versus direct mechanism. There are several possible experimental approaches to the problem. One is to compare rates of negative ion formation for a range of wavelengths, examining the effect of off resonant versus on resonant

pump wavelengths (in the hot electron-mediated picture, resonance should not be a factor). In the absence of a surface state, the valence band edge could be employed as the initial state. Another approach is to examine the relative rates for negative ion formation for a homologous series of adsorbates with different negative ion energies. Also, the polarization of the incident light can be manipulated to favor one process or the other, since direct surface photoexcitation is favored for p polarized light. In addition, the dependence on crystal material can be examined, since hot electron dynamics in transition metals are highly dependent on the position of the occupied d band.

An interesting but as yet unexplored subject is hot electron dynamics and coherence dephasing in quantum wells. The impact of the quantum size effect on dynamics and transport of hot electrons is as yet unknown. Possible materials which would be amenable to study include semiconductors and metals. Current and future work would also benefit immensely from additional detailed, self-consistent calculations of the excited electronic structure of adsorbate systems. Such calculations coupled with the experimental results presented here would greatly enhance our understanding of the electronic structure of Xe/Ag(111), but require state-of-the-art techniques in order to properly take into account many body effects, nonlocal effects (exchange and correlation), and relativistic effects due to the large Z atoms comprising the interface. Technological improvements on the current state of the two photon photoemission technique may also facilitate studies of systems more important to chemistry and catalysis. The use of vacuum ultraviolet or soft X-ray sources would improve the chemical sensitivity and specificity of the technique. The detection of photodesorbed ions and molecules instead of photoelectrons is another possibility.

In closing, the physics and chemistry of the interaction of light with excited electrons at adsorbate-covered surface is fundamentally complex, involving some of the more difficult aspects of solid state physics: many body effects, coherence, energy transfer, carrier transport, defect scattering, quantum confinement, and tunneling. This complexity also makes the system interesting, since information is yielded about important processes, assuming the data can be decomposed to yield information about the various processes at the surface by the appropriate application of exper-

imental and theoretical technique. Angle-resolved and coverage-resolved techniques were shown to be promising as experimental methods to decompose various processes or effects at the interface.

This work has shown that both the experimental and theoretical problems associated with the study of electron dynamics at interfaces are indeed tractable. It was also shown that the interwoven complexities inherent in this system can in some important cases be separated and adequately explained by the application of simple physical ideas to the results of systematic experimental investigations. The current ability to describe the observed behavior of electrons at surfaces in terms of the subtle interplay of many-body interactions, effective mass, the surface barrier, quantum confinement, and dielectric effects is in part due to the many experimental degrees of freedom and quality of data afforded by the technique of two photon photoemission. The success of this work is also due to the fact that the experiment brings together two mature experimental methodologies, ultrafast pump-probe spectroscopy and angle-resolved photoemission, and its explanatory power is leveraged from the large body of knowledge in these two fields. This technique has continuing promise as an important window into electronic and chemical processes at surfaces.

Bibliography

[1] Einstein, A.; Infeld, L., *The Evolution of Physics*, New York: Simon and Schuster, **1961**.

[2] Lovett-Cline, B., *The Men Who Made a New Physics*, Chicago: University of Chicago Press, **1987**.

[3] Mott, Nevill Francis, S.; Jones, H., *The Theory of the Properties of Metals and Alloys*, New York: Dover, **1936**.

[4] Tamm, I. E., *Phys. Z. Sowjetanion* **1932**, *1*, 733.

[5] Maue, A. W., *Z. Phys.* **1935**, *94*, 717.

[6] Goodwin, E. T., *Proc. Camb. Phil. Soc.* **1939**, *35*, 205–220.

[7] Goodwin, E. T., *Proc. Cambridge Philos. Soc.* **1939**, *35*, 221.

[8] Smythe, W. R., *Static and Dynamic Electricity*, New York: McGraw-Hill, **1950**.

[9] Landau, L. D., *Electrodynamics of Continuous Media*, Oxford: Pergamon, **1984**.

[10] Lang, N. D.; Kohn, W., *Phys. Rev. B* **1970**, *1*, 4555.

[11] Lang, N. D.; Kohn, W., *Phys. Rev. B* **1971**, *3*, 1215–1223.

[12] Grimes, C. C.; Brown, T. R., *Phys. Rev. Lett.* **1974**, *32*, 280–283.

[13] Johnson, P. D.; Smith, N. V., *Phys. Rev. B* **1983**, *27*, 2527–2530.

[14] Dose, V.; Altmann, W.; Goldmann, A.; Kolac, U.; Rogozic, J., *Phys. Rev. Lett.* **1984**, *52*, 1919–1921.

[15] Straub, D.; Himpsel, F., *Phys. Rev. Lett.* **1984**, *52*, 1922–1924.

[16] Giesen, K.; Hage, F.; Himpsel, F.; Riess, H. J.; Steinmann, W., *Phys. Rev. Lett.* **1985**, *55*, 300.

[17] Echenique, P. M.; Pendry, J. B., *J. Phys. C* **1978**, *11*, 2065–2075.

[18] Giesen, K.; Hage, F.; Himpsel, F. J.; Reiss, H. J.; Steinmann, W.; Smith, N. V., *Phys. Rev. B* **1987**, *35*, 975.

[19] Echenique, P. M.; Pendry, J. B., *Prog. Surf. Sci.* **1990**, *32*, 111–172.

[20] Fauster, T., *Prog. Surf. Sci.* **1994**, *46*, 177–86.

[21] Harris, C. B.; Ge, N. H.; Lingle, R. L.; McNeill, J. D.; Wong, C. M., *Ann. Rev. Phys. Chem.* **1997**, *48*, 711–744.

[22] Lang, N. D.; WIlliams, A. R., *Phys. Rev. B* **1978**, *18*, 616–636.

[23] Muscat, J. P.; Newns, D. M., *Prog. Surf. Sci.* **1978**, *9*, 1–43.

[24] Fischer, R.; Schuppler, S.; Fischer, N.; Fauster, T.; Steinmann, W., *Phys. Rev. Lett.* **1993**, *70*, 654–657.

[25] Fischer, R.; Fauster, T.; W., S., *Phys. Rev. B* **1993**, *48*, 15496–99.

[26] Fischer, R.; Fauster, T., *Phys. Rev. B* **1995**, *51*, 7112–15.

[27] Wallauer, W.; Fauster, T., *Surf. Sci.* **1995**, *333*, 731–735.

[28] Kevan, S. D., ed., *Angle-Resolved Photoemission : Theory and Current Applications*, vol. 74 of *Studies in surface science and catalysis*, Amsterdam: Elsevier, **1992**.

[29] Dose, V., *J. Phys. Chem.* **1984**, *88*, 1681.

[30] Dose, V., *Sur. Sci. Rep.* **1985**, *5*, 337.

[31] Smith, N. V., *Rep. Prog. Phys.* **1988**, *51*, 1227–1294.

[32] Giesen, K.; Hage, F.; Reiss, H.; Steinmann, W.; Haight, R.; Beigang, R.; Dreyfuss, R.; Avouris, P.; Himpsel, F., *Phys. Scr.* **1987**, *35*, 578.

[33] Steinmann, W., *Appl. Phys. A* **1989**, *49*, 365.

[34] Kubiak, G., *Surf. Sci.* **1988**, *201*, L475.

[35] Schuppler, S.; Fischer, N.; Fauster, T.; Steinmann, W., *Appl. Phys. A* **1990**, *51*, 322–26.

[36] Knoesel, E.; Hertel, T.; Wolf, M.; Ertl, G., *Chem. Phys. Lett.* **1995**, *240*, 409–416.

[37] Hertel, T.; Knoesel, E.; Hasselbrink, E.; Wolf, M.; Ertl, G., *Surf. Sci.* **1994**, *317*, L1147–L1151.

[38] Hertel, T.; Knoesel, E.; Wolf, M.; Ertl, G., *Phys. Rev. Lett.* **1996**, *76*, 535–538.

[39] Ogawa, S.; Nagano, H.; Petek, H., *Phys. Rev. B* **1997**, *55*, 10869–10877.

[40] Wolf, M.; Knoesel, E.; Hertel, T., *Phys. Rev. B* **1996**, *54*, R5295–R5298.

[41] Loudon, R., *The Quantum Theory of Light*, Oxford, New York: Oxford University Press, **1983**.

[42] Ogawa, S.; Nagano, H.; Petek, H.; Heberle, A. P., *Phys. Rev. Lett.* **1997**, *78*, 1339–1342.

[43] Knoesel, E.; Hotzel, A.; Wolf, M., *Phys. Rev. B* **1998**, *57*, 12812–12824.

[44] Vaterlaus, A.; Guarisco, D.; Lutz, M.; Aeschlimann, M.; Stampanoni, M.; Meier, F., *J. Appl. Phys.* **1990**, *67*, 5661–5663.

[45] Meier, F.; Vaterlaus, A.; Aeschlimann, M.; Lutz, M.; Guarisco, D.; Milani, F.; Siegmann, H. C., *J. Magn. Magn. Mater.* **1991**, *93*, 523–528.

[46] Meier, F.; Vaterlaus, A.; Aeschlimann, M.; Guarisco, D., *J. Appl. Phys.* **1991**, *69*, 5003–5003.

[47] Aeschlimann, M.; Burgermeister, R.; Pawlik, S.; Bauer, M.; Oberli, D.; Weber, W., *J. Electron. Spectrosc. Relat. Ph.* **1998**, *88*, 179–183.

[48] Bauer, M.; Pawlik, S.; Aeschlimann, M., *Phys. Rev. B* **1997**, *55*, 10040–10043.

[49] Bauer, M.; Pawlik, S.; Burgermeister, R.; Aeschlimann, M., *Surf. Sci.* **1998**, *404*, 62–65.

[50] Bauer, M.; Pawlik, S.; Aeschlimann, M., *Surf. Sci.* **1997**, *377*, 350–354.

[51] Petek, H.; Ogawa, S., *Prog. Surf. Sci.* **1997**, *56*, 239–310.

[52] Ogawa, S.; Nagano, H.; Petek, H., *Phys. Rev. Lett.* **1999**, *82*, 1931–1934.

[53] Chulkov, E.; Silkin, V.; Echenique, P., *Surf. Sci.* **1997**, *391*, L1217–23.

[54] Wannier, G. H., *Phys. Rev.* **1943**, *64*, 358–366.

[55] Whittaker, E. T.; Watson, G. N., *A Course of Modern Analysis*, Cambridge: Cambridge University Press, **1952**.

[56] Ashcroft, N. W.; Mermin, N. D., *Solid State Physics*, New York: Holt, Rinehart and Winston, **1976**.

[57] Kittel, C., *Introduction to Solid State Physics*, New York: Wiley, **1996**.

[58] García-Moliner, F.; Flores, F., *Introduction to the Theory of Solid Surfaces*, Cambridge, New York: Cambridge University Press, **1979**.

[59] Zangwill, A., *Physics at Surfaces*, New York: Cambridge University Press, **1988**.

[60] Davison, S. G.; Stęślicka, M., *Basic Theory of Surface States*, Oxford, New York: Oxford University Press, **1992**.

[61] Smith, N. V., *Phys. Rev. B* **1985**, *32*, 3549–3555.

[62] Fauster, T.; Steinmann, W., *Electromagnetic Waves: Recent Developments in Research, Vol. 2: Photonic Probes of Surfaces, P. Halevi, ed.*, Amsterdam: Elsevier, 1995 pp. 347–411.

[63] Merry, W. R., *Image Potential States at Metal-Dielectric Interfaces*, Ph.D. thesis, U. C. Berkeley, **1992**.

[64] Kevan, S. D.; Gaylord, R. H., *Phys. Rev. B* **1987**, *36*, 5809.

[65] García, N.; Reihl, B.; Frank, K.; Williams, A., *Phys. Rev. Lett.* **1985**, *54*, 591.

[66] Echenique, P.; Pendry, J., *Surf. Sci.* **1986**, *166*, 69.

[67] Echenique, P., *J. Phys. C* **1986**, *18*, L1133.

[68] Weinert, M.; Hulbert, S.; Johnson, P., *Phys. Rev. Lett.* **1985**, *55*, 2055.

[69] Echenique, P. M.; Flores, F.; Sols, F., *Phys. Rev. Lett.* **1985**, *55*, 2348–50.

[70] Schoenlein, R. W.; Fujimoto, J. G.; Eesley, G. L.; Capehart, T. W., *Phys. Rev. Lett.* **1988**, *61*, 2596–99.

[71] Schuppler, S.; Fischer, N.; Fauster, T.; Steinmann, W., *Phys. Rev. B* **1992**, *46*, 13539–13547.

[72] Echenique, P. M., *J. Phys. C* **1985**, *18*, L1133–38.

[73] Bausells, J.; Echenique, P. M., *Phys. Rev. B* **1986**, *33*, 1471–73.

[74] de Andrés, P. L.; Echenique, P. M.; Flores, F., *Phys. Rev. B* **1989**, *39*, 10356–58.

[75] Goldmann, A.; Altmann, W.; Dose, V., *Sol. State Comm.* **1991**, *79*, 511–514.

[76] de Andrés, P.; Echenique, P. M.; Flores, F., *Phys. Rev. B* **1989**, *35*, 4529–4532.

[77] Echenique, P., personal communication.

[78] Jaklevic, R. C.; Lambe, J.; Mikkor, M.; Vassell, W. C., *Phys. Rev. Lett.* **1971**, *26*, 88.

[79] Jaklevic, R. C.; Lambe, J.; Mikkor, M.; Vassell, W. C., *Sol. State Comm.* **1972**, *10*, 199.

[80] Jaklevic, R. C.; Lambe, J., *Phys. Rev. B* **1975**, *12*, 4146–4160.

[81] Loly, P. D.; Pendry, J. B., *J. Phys. C* **1983**, *16*, 423–431.

[82] Wachs, A. L.; Shapiro, A. P.; Hsieh, T. C.; Chiang, T.-C., *Phys. Rev. B* **1986**, *33*, 1460–1463.

[83] Jalochowski, M.; Knoppe, H.; Lillenkamp, G.; Bauer, E., *Phys. Rev. B* **1992**, *46*, 4693.

[84] Mueller, M. A.; Miller, T.; Chiang, T.-C., *Phys. Rev. B* **1990**, *41*, 5214–20.

[85] Schmitz-Hübsch, T.; Oster, K.; Radnik, J.; Wandelt, K., *Phys. Rev. Lett.* **1995**, *74*, 2595.

[86] Paniago, R.; Matzdorf, R.; Meister, G.; Goldmann, A., *Surf. Sci.* **1995**, *325*, 336–342.

[87] Smith, N.; Brookes, N. B.; Chang, Y.; Johnson, P. D., *Phys. Rev. B* **1994**, *49*, 332–338.

[88] Inglesfield, J., *Angle-Resolved Photoemission : Theory and Current Applications*, vol. 74 of Kevan [28], 1992 pp. 15–61.

[89] Feder, R., *Polarized Electrons in Surface Physics*, Singapore, Philadelphia: World Scientific, **1985**.

[90] Williams, R.; Srivastava, G.; McGovern, I., *Rep. Prog. Phys.* **1980**, *43*, 1357–414.

[91] Jenkins, F. A.; White, H. E., *Fundamentals of Optics*, New York: McGraw-Hill, **1957**.

[92] McNeill, J. D.; Harris, C. B., *Sol. State Comm.* **1993**, *87*, 1089–1092.

[93] Lindgren, S. Å.; Walldén, L., *Sol. State Comm.* **1980**, *34*, 671.

[94] Donath, M.; Ertl, K., *Surf. Sci.* **1992**, *262*, L49–L54.

[95] Padowitz, D. F.; Merry, W. R.; Jordan, R. E.; Harris, C. B., *Phys. Rev. Lett.* **1992**, *69*, 3583–3586.

[96] Merry, W. R.; Jordan, R. E.; Padowitz, D. F.; Harris, C. B., *Surf. Sci.* **1993**, *295*, 393–401.

[97] Frank, K. H.; Yannoulis, P.; Dudde, R.; Koch, E. E., *J. Chem. Phys.* **1988**, *89*, 7569–7576.

[98] Horn, K.; Hohlfeld, A.; Somers, J.; Lindner, T.; Hollins, P.; Bradshaw, A., *Phys. Rev. Lett.* **1988**, *61*, 2488–2491.

[99] Lindgren, S. Å.; Walldén, L., *Sol. State Comm.* **1978**, *28*, 283.

[100] Heskett, D.; Frank, K.-H.; Koch, E.; Freund, H.-J., *Phys. Rev. B* **1987**, *36*, 1276.

[101] Fischer, N.; Schuppler, S.; Fischer, R.; Fauster, T.; Steinmann, W., *Phys. Rev. B* **1991**, *43*, 14722–14725.

[102] Lindgren, S. Å.; Walldén, L., *Phys. Rev. B* **1988**, *38*, 3060–3067.

[103] Fischer, N.; Schuppler, S.; Fischer, R.; Fauster, T.; Steinmann, W., *Phys. Rev. B* **1993**, *47*, 4705–13.

[104] Wolfram, S., *Mathematica : a system for doing mathematics by computer*, Redwood City, Calif.: Addison-Wesley, **1988**.

[105] Arfken, G. B., *Mathematical Methods for Physicists*, Orlando: Academic Press, **1985**.

[106] Press, W. H., *Numerical Recipes in C : The Art of Scientific Computing*, Cambridge, New York: Cambridge University Press, **1988**.

[107] Höfer, U., personal communication.

[108] McNeill, J. D.; Lingle, R. L.; Jordan, R. E.; Padowitz, D. F.; Harris, C. B., *J. Chem. Phys.* **1996**, *105*, 3883–3891.

[109] Klein, M. L.; Venables, J. A., eds., *Rare Gas Solids*, London ; New York: Academic Press, **1976-1977**.

[110] Harrison, W. A., *Electronic Structure and the Properties of Solids*, New York: Dover, **1989**.

[111] Lingle, R. L.; Padowitz, D. F.; Jordan, R. E.; McNeill, J. D.; Harris, C. B., *Phys. Rev. Lett.* **1994**, *72*, 2243–2246.

[112] Unguris, J.; Bruch, L. W.; Moog, E. R.; Webb, M. B., *Surf. Sci.* **1979**, *87*, 415.

[113] Unguris, J.; Bruch, L. W.; Moog, E. R.; Webb, M. B., *Surf. Sci.* **1981**, *109*, 522.

[114] Dai, P.; Angot, T.; Ehrlich, S. N.; Wang, S. K.; Taub, H., *Phys. Rev. Lett.* **1994**, *72*, 685.

[115] Fowler, R. H., *Phys. Rev.* **1931**, *38*, 45.

[116] Ando T, Fowler AB, S. F., *Rev. Mod. Phys.* **1982**, *54*, 437–672.

[117] Behm, R. J.; Brundle, C. R.; Wandelt, K., *J. Chem. Phys.* **1986**, *85*, 1061.

[118] Lingle, R. L.; Ge, N. H.; Jordan, R. E.; McNeill, J. D.; Harris, C. B., *Chem. Phys.* **1996**, *208*, 297–298.

[119] Lingle, R. L.; Ge, N. H.; Jordan, R. E.; McNeill, J. D.; Harris, C. B., *Chem. Phys.* **1996**, *205*, 191–203.

[120] Cole, M. W.; Cohen, M. H., *Phys. Rev. Lett.* **1969**, *23*, 1238–1241.

[121] Cole, M. W., *Phys. Rev. B* **1971**, *3*, 4418–4422.

[122] Trninić-Radja, B.; Šunjić, M.; Lenac, Z., *Phys. Rev. B* **1989**, *40*, 9600.

[123] Brown, T. R.; Grimes, J. C., *Phys. Rev. Lett.* **1972**, *9*, 1233.

[124] Jackson, J. D., personal communication.

[125] Michaud, M.; Clautier, P.; Sanche, L., *Phys. Rev. B* **1991**, *44*, 10485.

[126] Colbert, D. T.; Miller, W. H., *J. Chem. Phys.* **1992**, *96*, 1982–91.

[127] Ortega, J.; Himpsel, F. J.; Mankey, G. J.; Willis, R. F., *Phys. Rev. B* **1993**, *47*, 1540–1552.

[128] McNeill, J. D.; Lingle, R. L.; Ge, N. H.; Wong, C. M.; Jordan, R. E.; Harris, C. B., *Phys. Rev. Lett.* **1997**, *79*, 4645–4648.

[129] Haight, R., *Surf. Sci. Rep.* **1983**, *21*, 275–325.

[130] Schoenlein, R. W.; Fujimoto, J. G.; Eesley, G. L.; Capehart, T. W., *Phys. Rev. B* **1991**, *43*, 4688–4698.

[131] Williams, R. T.; Royt, T. R.; Long, J. C.; Kabler, M. N., *J. Vac. Sci. Technol.* **1982**, *21*, 509.

[132] Haight, R.; Bokor, J.; Stark, J.; Stork, R. H.; Freeman, R. R.; Bucksbaum, P. H., *Phys. Rev. Lett.* **1985**, *54*, 1302.

[133] Schwentner, N.; Skibowski, M.; Steinmann, W., *Phys. Rev. B* **1973**, *8*, 2965–2968.

[134] Schwentner, N.; Himpsel, F.; Saile, V.; Skibowski, M.; Steinmann, W.; Koch, E. E., *Phys. Rev. Lett.* **1975**, *34*, 528–531.

[135] Bacalis, N. C.; Papaconstantopoulos, D.; Pickett, W. E., *Phys. Rev. B* **1988**, *38*, 6218–6226.

[136] Schwentner, N.; Koch, E. E.; Jortner, J., *Electronic Excitations in Condensed Rare Gases*, Berlin: Springer-Verlag, **1985**.

[137] Bartels, L.; Wolf, M.; Meyer, G.; Rieder, K.-H., *Chem. Phys. Lett.* **1998**, *291*, 573–8.

[138] Springer, C.; Head-Gordon, M., *Chem. Phys.* **1996**, *205*, 73–89.

Appendix A

Data Acquisition Programs

```
/*
 MCBACQ.C  --  MCB (multichannel buffer) DATA ACQUISITION PROGRAM

 Purpose:


   Simple program to collect data for argv[1] seconds of
   LIVE_TIME and exit.  The program communicates with the MCB
   via the mailbox i/o interface of the MCB card.  It sets up
   and starts a scan with argv[1] seconds of LIVE_PRESET.
   Then the program waits for the scan to finish.  LIVE_TIME
   may differ substantially from wall clock time, so the
   program may only terminate when LIVE_TIME==LIVE_PRESET.
   LIVE_TIME is read from the MCB. However, asking the MCB for
   the LIVE_TIME too often does not let the MCB perform its
   data acquisition duties. Therefore, the code tries to guess
   how much longer it should sleep before the scan is
   finished.


 Requires DIALOG.C and DIALOG.H code Copyright EG&G Ortec

*/
#include <stdio.h>
#include <stdlib.h>
#include <string.h>
#include <ctype.h>
```

```
#include <time.h>
#include <dialog.h>
#define CLOCKS_PER_SEC 1000
#define SCAN_TIME 15 /* Scan duration in seconds */

char mcb_env_var[81];  /* MCB environment variable storage */

main(int argc, char *argv[])
{
   char response[129], pctbuf[12];
   char cmd_ptr[129], *lstr="00750";
   int mcb_number = 1, cmd_len = 0,
     max_resp = 128, max_cmd = 128;
   int type = MCB$918 ;
   int i, sum, resp_len, ioerr, errmac, errmic;
   int scan_duration, elap, ltime, rtime;
   clock_t timeo;
   *cmd_ptr=NULL;
/* SHAREPOR is the shared memory port addr (see dialog.c) */
/* the port is used for communication with the MCB */
/* SHAREMEM is the actual RAM address */
/* that's where the actual data is */


/*********************************************************/
/* Check for a time argument (command line)              */
/*********************************************************/

   if(argc > 1) {                        /* 1 or more params */
      scan_duration = atoi(argv[1]);
   } else {
      scan_duration = SCAN_TIME;
   }

/*********************************************
  assume MCB 1, do mcb_dialog() to see if card
    is present and working
*********************************************/
   printf("MCBACQ V1.00\n");

/*************************************************************
  Now use mcb_dialog to send the following sequence of
```

```
   commands to MCB:
 STOP
 CLEAR_ALL
 CLEAR_PRESETS (probably unnecessary, done by CLEAR_ALL)
 SET_LIVE_PRESET 50*scan_duration (20ms ticks)
 START
 ACQUIRE (wait loop for scan_duration secs)
 (check LIVE_TIME to see if equal to 50*scan_duration)
 (if not, estimate how long until scan is finished, goto A)
 STOP
 CLEAR_PRESETS
*****************************************************************/
   ioerr = mcb_read(mcb_number,type,max_resp,
     response,&resp_len);
   if(ioerr > 0) {
     print_resp(response,resp_len);
   }
   if(ioerr < 0) {
     printf("I/O Error number %i\n",ioerr);
   }


/* Send STOP */

   sprintf(cmd_ptr,"STOP");
   cmd_len=strlen(cmd_ptr);
   ioerr = mcb_dialog(mcb_number,type,cmd_ptr,cmd_len,
        max_resp,response,&resp_len,
        &errmac,&errmic);
   print_resp(response,resp_len);
   /* print percent response */
   sprintf(pctbuf,"%%%3.3d%3.3d",errmac,errmic);
   sum = 0;                          /* calculate checksum */
   for(i = 0; i < 7; i++) {
      sum += pctbuf[i];
   }
   sum %= 256;                       /* checksum mod 256 */
   printf("%s%3.3d<CR>\n",pctbuf,sum);


/* Send CLEAR_ALL */
```

```
   sprintf(cmd_ptr,"CLEAR_ALL");
   cmd_len=strlen(cmd_ptr);
   printf("Sending %s to MCB\n",cmd_ptr);
   ioerr = mcb_dialog(mcb_number,type,cmd_ptr,cmd_len,
        max_resp,response,&resp_len,
        &errmac,&errmic);
   print_resp(response,resp_len);
   sprintf(pctbuf,"%%%3.3d%3.3d",errmac,errmic);
   sum = 0;                          /* calculate checksum */
   for(i = 0; i < 7; i++) {
      sum += pctbuf[i];
   }
   sum %= 256;                       /* checksum mod 256 */
   printf("%s%3.3d<CR>\n",pctbuf,sum);


/* Send SET_LIVE_PRESET */

   sprintf(cmd_ptr,"SET_LIVE_PRESET %i",scan_duration * 50);
   cmd_len=strlen(cmd_ptr);
   printf("Sending %s to MCB\n",cmd_ptr);
   ioerr = mcb_dialog(mcb_number,type,cmd_ptr,cmd_len,
        max_resp,response,&resp_len,
        &errmac,&errmic);
   print_resp(response,resp_len);
   sprintf(pctbuf,"%%%3.3d%3.3d",errmac,errmic);
   sum = 0;                          /* calculate checksum */
   for(i = 0; i < 7; i++) {
      sum += pctbuf[i];
   }
   sum %= 256;                       /* checksum mod 256 */
   printf("%s%3.3d<CR>\n",pctbuf,sum);


/* Send START */

   sprintf(cmd_ptr,"START");
   cmd_len=strlen(cmd_ptr);
   printf("Sending %s to MCB\n",cmd_ptr);
   ioerr = mcb_dialog(mcb_number,type,cmd_ptr,cmd_len,
        max_resp,response,&resp_len,
        &errmac,&errmic);
```

```
   print_resp(response,resp_len);
   sprintf(pctbuf,"%%%3.3d%3.3d",errmac,errmic);
   sum = 0;                          /* calculate checksum */
   for(i = 0; i < 7; i++) {
      sum += pctbuf[i];
   }
   sum %= 256;                       /* checksum mod 256 */
   printf("%s%3.3d<CR>\n",pctbuf,sum);


/* start wait loop */

   timeo=clock(); /* DOS has no sleep function, so loop */
   do {
      elap=clock()-timeo;
      /* assume .5 secs of deadtime */
   } while( elap < CLOCKS_PER_SEC * scan_duration );


   /* check the livetime */

   resp_len=0;
   do {
     sprintf(cmd_ptr,"SHOW_LIVE");
     cmd_len=strlen(cmd_ptr);
     printf("Sending %s to MCB\n",cmd_ptr);
     ioerr = mcb_dialog(mcb_number,type,cmd_ptr,cmd_len,
          max_resp,response,&resp_len,
          &errmac,&errmic);
   } while( resp_len < 5 );  /* loop until we get a response */
   print_resp(response,resp_len);
   sprintf(pctbuf,"%%%3.3d%3.3d",errmac,errmic);
   sum = 0;                          /* calculate checksum */
   for(i = 0; i < 7; i++) {
      sum += pctbuf[i];
   }
   sum %= 256;                       /* checksum mod 256 */
   printf("%s%3.3d<CR>\n",pctbuf,sum);

   /* BUSY-WAIT loop to keep the program from terminating
      before the scan is finished */
   do {
```

```
      strncpy(lstr,response+7,4);
      printf("livetime ticks so far: %s\n",lstr);
      ltime=atoi(lstr);
      if ( 50*scan_duration-ltime < 10 ) {
        rtime=10;
      } else {
        rtime=50*scan_duration-ltime;
      }
      timeo=clock();
      do {
         elap=clock()-timeo;
      /* wait until rtime*20 clock ticks have passed */
      } while (elap < rtime*20) ;

      do {
        sprintf(cmd_ptr,"SHOW_LIVE");
        cmd_len=strlen(cmd_ptr);
        printf("Sending Command: %s",cmd_ptr);
        ioerr = mcb_dialog(mcb_number,type,cmd_ptr,cmd_len,
          max_resp,response,&resp_len,
          &errmac,&errmic);
      } while( resp_len < 5 );
      print_resp(response,resp_len);
    } while (ltime < scan_duration*50);

/* Send CLEAR_PRESETS */

    sprintf(cmd_ptr,"CLEAR_PRESETS");
    cmd_len=strlen(cmd_ptr);
    printf("Sending %s to MCB\n",cmd_ptr);
    ioerr = mcb_dialog(mcb_number,type,cmd_ptr,cmd_len,
         max_resp,response,&resp_len,
         &errmac,&errmic);
    sprintf(pctbuf,"%%%3.3d%3.3d",errmac,errmic);
    sum = 0;                          /* calculate checksum */
    for(i = 0; i < 7; i++) {
       sum += pctbuf[i];
    }
    sum %= 256;                       /* checksum mod 256 */
    printf("%s%3.3d<CR>\n",pctbuf,sum);
```

```
}

/*
*
* C Call:
*       print_resp(response,resp_len);
*
*/
void print_resp(char *response, int resp_len)
{
   int outchars = 0, i;
   char buffer[129], *ptr;

   for(i = 0, ptr = buffer; i < resp_len; i++) {
      if(isprint(response[i])) {      /* printable char */
        *ptr++ = response[i];
        outchars++;
      } else if(response[i] == '\r') { /* carriage return */
        strcpy(ptr,"<CR>");
        ptr += 4;
        outchars += 4;
      } else if(response[i] == '\n') { /* linefeed */
        strcpy(ptr,"<LF>");
        ptr += 4;
        outchars += 4;
      } else {                        /* otherwise = <^?> */
        sprintf(ptr,"<^%c>",response[i]+64);
        ptr += 4;
        outchars += 4;
      }

      if(outchars > 72) {        /* if line gets too long */
        sprintf(ptr,"...\n          <Extra Characters Deleted>");
        ptr += strlen(ptr);
        break;
      }
   }

   if(outchars > 0) {            /* if any chars printed */
      *ptr++ = '\n';
   }
```

```
   *ptr++ = '\0';
   printf("%s",buffer);
}
```

```
/*
        MCBMAT3.C       Program to read dual port memory
                        and write it to a mat-file.  The
                        name of the matfile is argv[1].
                        The dual-port memory contains 8000
                        long int (32 bit) values representing a
                        histogram of electron energies.

                        April '95 JDM

                        modified to automatically select the
                        appropriate data type to save space
                        (long int, int, char) Sept '97 JDM

                        Also, fixed base address alignment error
                        (manual was incorrect)

                        Note: this is a 16-bit DOS program.
                        Type "int" is 16 bits.

*/

#include <stdio.h>
#include <string.h>
#include <malloc.h>

#define BASEADD 0xD0000250L /* Segment:Offset D000:0250 */
#define MASK 0x7FFFFFFFL    /* Keep all but ROI bit */
#define MAXCHAN 0x4000      /* Set for maximum # of channels */

main(int argc, char *argv[])
```

```
{
  unsigned long   data_val;  /* storage for channel data value */
  unsigned long   *data_buf,
    chan_data,
    mattype, /* type of MATfile to write */
    mcbmax;          /* max value in MCB */
  unsigned long  far *chan_ptr; /* pointer to data memory
                                   (far only works in DOS) */

  unsigned char mcb; /* MCB number */

  int start_chan,     /* starting channel to display */
    end_chan,       /* ending channel to display */
    loop;

  char filename[20],
    *varname; /* file format is 8+3 chars long: month,
                 day, "scan number" and spec number */

  FILE    *fp_mat;

  /* We only use MCB number 1 */

  mcb = 1;
  strcpy(varname,"mmddn000");

  /* We use channels 1 thru 8000 */

  start_chan = 1;
  end_chan = 8000;
  data_buf=(unsigned long *)malloc(8000*sizeof(unsigned long));

  /* Point to dual-port memory
     (this is the unportable DOS way) */

  chan_ptr = (unsigned long far *)BASEADD;


  /* sanity check command line */

  if (argc != 2)
    {
```

```
    printf("USAGE:mcbmat filename\n");
    exit(1);
  }

/* read data into buffer array */
mcbmax=0;
for (loop = start_chan; loop <= end_chan; loop++)
  {
    /* read data from pointed to channel and
       mask off ROI bit */
    chan_data = MASK & *(chan_ptr + loop);
    if (chan_data > mcbmax) mcbmax=chan_data;
    data_buf[loop]=chan_data;
  }

      /* determine the type (to save disk space) */
if (mcbmax<257) mattype=50; /* unsigned char */
else if (mcbmax<32769) mattype=40 ; /* 16 bit uint */
else mattype=20; /* 32-bit uint */

/* open output file */
varname = argv[1];
sprintf(filename,"%s.mat",varname);
printf("saving MCB data to %s\n",filename);
fp_mat = fopen(filename,"wb");

/* first save MATLAB header info */
headmat(fp_mat,mattype,varname,1,8000,0);

/* save channel data */
if (mattype==50) {
  for (loop = start_chan; loop <= end_chan; loop++)
    {
      chan_data=(unsigned char)data_buf[loop];
      fwrite(&chan_data,sizeof(unsigned char),1,fp_mat);
    }
} else if (mattype==40) {
  for (loop = start_chan; loop <= end_chan; loop++)
    {
      chan_data=(unsigned int)data_buf[loop];
      fwrite(&chan_data,sizeof(unsigned int),1,fp_mat);
    }
```

```
  } else { /* mattype = 20 */
    for (loop = start_chan; loop <= end_chan; loop++)
      {
        chan_data=(unsigned long)data_buf[loop];
        fwrite(&chan_data,sizeof(unsigned long),1,fp_mat);
      }
  }
  fclose(fp_mat);
}

/*
 * headmat -- write a header in version 1.0 MATfile format.
 * See "The Matlab External Interface Guide" for details.
 */
typedef struct {
     long type;   /* type */
     long mrows;  /* row dimension */
     long ncols;  /* column dimension */
     long imagf;  /* flag indicating imag part */
     long namlen; /* name length (including NULL) */
} Fmatrix;

headmat(fp, type, pname, mrows, ncols, imagf)
     FILE *fp;    /* File pointer */
     int type;    /* Type flag: 20 unsigned long int (32 bit),
                     40 unsigned int16, 50 unsigned char */
     /* See LOAD in reference section of guide for more info. */
     int mrows;       /* row dimension */
     int ncols;       /* column dimension */
     int imagf;       /* imaginary flag */
     char *pname;     /* pointer to matrix name */
{
  Fmatrix x;
  int mn;

  x.type = type;
  x.mrows = mrows;
  x.ncols = ncols;
  x.imagf = imagf;
  x.namlen = strlen(pname) + 1;
  mn = x.mrows * x.ncols;
  fwrite(&x, sizeof(Fmatrix), 1, fp);
```

```
  fwrite(pname, sizeof(char), (int)x.namlen, fp);
}
```

```
/* STAGE.C:

      move the translation stage, version 2, for Klinger CC1.1,
      moving it in 1 micron steps.  Stage is controlled by the
      National Instruments GPIB card.

      See CC1.1 manual for command syntax

      Jason McNeill, April 1995

 Be sure to include mibm.obj in cl line and
 /AM for Medium Memory Model

 Usage format:

     stage type y

     where type is: o (set origin)
                    a (absolute position)
                    + (relative position, positive)
                    - (relative position, negative)

     and y is either 0 for origin search
     or (any number) for stage movement
*/

#include <stdio.h>
#include <string.h>
#include "ibdecl.h"  /* GPIB declarations */


extern int ibfind(), /* gpib functions */
           ibclr(),
           ibwrt(),
```

```
            ibrd(),
            ibonl(),
            ibloc();

int stage; /* stage device number in gpib calls */

main (int argc, char *argv[])
{
  void
    error(),
    finderr(),
    set_origin(),
    move_relativeneg(),
    move_absolute(),
    move_relativepos();
  char
    movtyps[2],
    movdists[20];
  const char
    *originstr = "o",
    *absolutestr = "a",
    *relativepos = "+",
    *relativeneg = "-";

  /* parse argc, argv */

  if ( argc > 1)  {
    strcpy(movtyps, argv[1]);
    strcpy(movdists, argv[2]);
  }
  else  {
    printf("usage: stage <movtype> y\n");
    exit(1);
  }


  /* open GPIB device number 7 */

  if ( (stage = ibfind ("DEV7")) < 0) finderr();
  if( ibclr(stage) & ERR) error();
```

```
  /* depending on the value of *movtyps[0], choose a function,
     either set_origin, move_absolute, move_relativepos, or
     move_relativeneg */

  if ( *movtyps == *originstr )
    set_origin(movdists);

  if ( *movtyps == *absolutestr )
    move_absolute(movdists);

  if ( *movtyps == *relativepos )
    move_relativepos(movdists);

  if ( *movtyps == *relativeneg )
    move_relativeneg(movdists);

}



void finderr() { /* Error: can't find device */
  printf("Ibfind error; possibly device does not match\n");
  printf("configuration name DEV7\n");
}

void error() { /* general GPIB error handler
                  "ibsta" and "iberr" declared in
                  header ibdecl.h */
  printf("GPIB function call error\n");
  printf("ibsta=0x%x, iberr=0x%x,",ibsta,iberr);
  printf(" ibcnt=0x%x\n",ibcnt);
}

void set_origin(char *stageto) { /* sets origin of stage */
  char *outstr = "A\015";

  printf("setting origin\n") ;
  ibwrt(stage, outstr, 2);
  if (ibsta & ERR) error();
if ( ibclr(stage) & ERR) error();
```

```
                        /* move to an absolute position */
  char outstr[10];
  int lng;

  printf("moving to absolute position %s microns\n",stageto) ;
  sprintf(outstr,"P %s\015", stageto);
  lng = strlen(outstr);
  ibwrt (stage, outstr, lng);
  if (ibsta & ERR) error();
  /* ask stage for status, this instruction effectively
     pauses the computer until the stage finishes stepping.
     Without this instruction, we would start taking data
     before the stage was finished */
  sprintf(outstr,"B\015");
  lng=strlen(outstr);
  ibwrt (stage, outstr, lng);
}

void move_relativepos(char *stageto) {
                      /* move to a relative (+) position */
  char outstr[10];
  int lng;

  printf("moving stage forwards %s microns\n",stageto) ;
  sprintf(outstr,"N %s\015", stageto);
  lng = strlen(outstr);
  ibwrt (stage, outstr, lng);
  if (ibsta & ERR) error();
  sprintf(outstr,"+\015");
  lng = strlen(outstr);
  ibwrt (stage, outstr, lng);
  if (ibsta & ERR) error();
  sprintf(outstr,"G\015");
  lng = strlen(outstr);
  ibwrt (stage, outstr, lng);
  if (ibsta & ERR) error();
  sprintf(outstr,"B\015");
  lng = strlen(outstr);
  ibwrt (stage, outstr, lng);
  if (ibsta & ERR) error();
}
```

```
void move_relativeneg(char *stageto) {
                        /*move to a (-) relative position */
  char outstr[10];
  int lng;

  printf("moving stage backwards %s microns\n",stageto) ;
  sprintf(outstr,"N %s\015", stageto);
  lng = strlen(outstr);
  ibwrt (stage, outstr, lng);
  if (ibsta & ERR) error();
  sprintf(outstr,"-\015");
  lng = strlen(outstr);
  ibwrt (stage, outstr, lng);
  if (ibsta & ERR) error();
  sprintf(outstr,"G\015");
  lng = strlen(outstr);
  ibwrt (stage, outstr, lng);
  if (ibsta & ERR) error();
  sprintf(outstr,"B\015");
  lng = strlen(outstr);
  ibwrt (stage, outstr, lng);
  if (ibsta & ERR) error();
}
```

```
/*
   SCOPE.C

     using National Instruments GPIB card, grab a waveform from a
     LeCroy 9300 digital oscilloscope.  Takes 2500 points from
     math trace A.

     This program is useful as a general way to download a
     waveform from the digital oscilloscope in order to
     analyze it on a computer.  Its primary use was to acquire
     waveforms from a Varian Auger spectrometer and to acquire
     autocorrelation traces from the INRAD autocorrelator.
```

```
     -Jason McNeill (Oct 1993) */

/* Be sure to include mib*.obj in cl line,
   /AM for medium memory model */

/* compile with "-DNO_SCOPE" to test without digital scope */

#include <stdio.h>
#include <string.h>
#include "decl.h"

/*  from decl.h

extern int      ibsta,
                iberr,
                ibcnt;
*/

char  file_name[32];
void  save_data(), get_new_filename();
int  data[2500];
#ifndef NO_SCOPE
int  ibfind(),
  ibclr(),
  ibwrt(),
  ibrd(),
  ibonl(),
  ibloc(); /* from mcib*.obj */
#endif

main (int argc, char *argv[])
{

  void  error(), finderr();
  int  scope, cnt, ndat;

  /* assume argv[1] is the output file name */
  if ( argc > 1)
    strcpy(file_name, argv[1]);
  else
    strcpy(file_name, "auger.tmp");
```

```
  /* open GPIB device 4 */
#ifndef NO_SCOPE
  if ( (scope = ibfind ("DEV4")) < 0) finderr();


  /* clear device */

  if( ibclr(scope) & ERR) error();

  /* set scope output format to two-byte word, binary */

  ibwrt (scope, "CFMT OFF, WORD, BIN",19);
  /* check gpib status */
  if (ibsta & ERR) error();

  /* set scope output format to "header off"
     (header contains information on scope dwell time,
     voltage scale) */
  ibwrt (scope, "CHDR OFF", 8);
  if (ibsta & ERR) error();

  /* set scope output to little-endian (PC byte order) */
  ibwrt (scope, "CORD LO", 7);
  if (ibsta & ERR) error();

  /* tell scope to send 2500 points */
  ibwrt (scope, "WFSU NP, 2500", 13);
  if (ibsta & ERR) error();

  /* ask to send DAT1, data block, of TA, trace A */
  ibwrt (scope, "TA:WF? DAT1", 11);
  if (ibsta & ERR) error();

  /* now read 2500 points (5000 bytes) into <data> */
  cnt = 5000;
  ibrd (scope, data, cnt);
#else
  cnt=5000;
#endif
  /* tell how many bytes received */
  printf("%d bytes received\n", cnt);
```

```
#ifndef NO_SCOPE
  /* Now send a clear to the scope */
  ibclr (scope);
  ibloc (scope);
  ibonl (scope,0);
#endif
  ndat = cnt/2;

  save_data(ndat);
  return(0);

}

void finderr() {

/* Error: can't find device */

  printf("Ibfind error; possibly device does not match\n");
  printf("configuration name DEV4\n");
}

void error() {

  printf("GPIB function call error\n");

#ifndef NO_SCOPE
  printf("ibsta=0x%x, iberr=0x%x,",ibsta,iberr);
  printf(" ibcnt=0x%x\n",ibcnt);
#endif
}

void save_data(int num)
{
  int i;
  char input[20];
  FILE *stream;

  if ((stream = fopen(file_name, "rb")) != NULL){
    fclose(stream);
    printf("%s\n",file_name);
    printf("File Already Exists!!!\n");
    printf("Do you want to OVERWRITE?\n");
```

```
    printf("Answer Y or N\n");
    gets(input);
    if (input[0] != 'y' && input[0] != 'Y')
      get_new_filename();
  }
  if ((stream = fopen(file_name, "wb")) == NULL){
    printf("Unable to open file for writing, exiting...\n");
    exit(1);
  }

  for (i=0; i != num; i++) /* write out the 2500 data
                              points to file */
    fprintf(stream, "%i\n", data[i]);
  fclose(stream);
}

void get_new_filename()
{
  char input[20];
  FILE *stream;
  stream=NULL;
  do{
    printf("The last file was %s\n", file_name);
    printf("Input new data file name.\n");
    gets(file_name);
    if ((stream = fopen(file_name, "rb")) != NULL){
      fclose(stream);
      printf("File Already Exists!!!\n");
      printf("Do you want to OVERWRITE?\n");
      printf("Answer Y or N\n");
      gets(input); /* security hole */
      if (input[0] == 'y' || input[0] == 'Y')
        unlink(file_name);
    }
  } while ( input[0] != 'y'
            && input[0] != 'Y'
            && stream != NULL );
}
```

```
% TRTPPE.M
%       A data acquisition script written in the MATLAB scripting
%       language for the purpose of acquiring two-photon
%       photoemission time-of-flight spectra at a series of
%       optical time delays determined by setting the position of
%       a mechanical translation stage.  This version allows
%       three different step sizes.  The three step sizes are
%       useful when the kinetics trace has fast and slow
%       components which need to be resolved.  The instrument
%       control aspects are contained in three DOS executable
%       programs: stage.exe, mcbacq.exe, and mcbmat.exe.  These
%       programs were written in C by Jason McNeill.
%
%       Original version DYNA.M written in 1995 by Jason McNeill.
%       Nien-Hui Ge contributed code for variable step sizes.
%       Modified to work with MCBACQ.EXE in 1997 by Jason McNeill.
%
%       Some scan parameters are specified in the following section.
%       Scan parameters are saved in a file named MMDDX000.mat,
%       where MM, DD, and X are the month, day, and scan number,
%       respectively.  A complete histogram of electron counts as
%       a function of energy is saved at each stage position, in
%       files named MMDDXYYY.mat.

% uses \dyna\stage.exe to move stage.  See source code for command
%       format.

% uses \dyna\mcbacq.exe to start acquisition and acquire for
%      argv[1] seconds.

% uses \dyna\mcbmat.exe to write data to a .MAT file.
%      File name specified by argv[1].


% User configurable section:
b4orig=70; % number of microns before t0 (length of baseline)
           % this is maximum positive number on stage controller
aftorig=70;% number of microns after t0
           % this is the most negative number on the controller
           % total stage range = b4orig+aftorig
```

```
endshort=40;    % total number of microns acquired in stepshort
stepshort=5;    % short stepsize in microns
endmid=60;      % total number of microns acquired in stepmid
stepmid=2;      % medium stepsize in microns
steplong=5;     % long stepsize in microns
acqtime=15;     % data acquisition time per step

%Do Not edit after this line unless you know what you are doing.

% debug flag, set to "1" if you want debugging messages

debug=0;


% Create vector <strang> describing stage positions

ststart = aftorig;  %start stage 50 microns after t0.
tot=b4orig+aftorig; %total stage range

% These three lines contributed by N.-H. Ge.
stlong=0:steplong:(tot-endshort-endmid);
stmid=(tot-endshort-endmid+stepmid):stepmid:(tot-endshort);
stshort=(tot-endshort+stepshort):stepshort:tot;

%set stage at these points, used for the stage driving program
strang = [stlong,stmid,stshort];

% the stage is mounted "backwards", so strangfwd represents the
     % stage delay for <+> corresponding to longer delay
     % between visible and UV pulses.
strangfwd=(tot-strang(length(strang):-1:1));
     %real stage positions, starting from 0 toward positive delay
time=strangfwd*200/30;
     %time array used for the time-dependence analysis


% Advise user of current settings for time steps

tmpstr = ['stage will scan from ',num2str(-b4orig),' um (',...
     num2str(-b4orig*6.66),'fs) to '];
disp(tmpstr);
tmpstr = [num2str(endshort-b4orig),' um (',...
```

```
     num2str((endshort-b4orig)*6.66),...
     'fs) in steps of ',num2str(stepshort),' um (',...
     num2str(stepshort*6.66),' fs) to '];
disp(tmpstr);
tmpstr = [num2str(endmid+endshort-b4orig),' um (',...
     num2str((endmid+endshort-b4orig)*6.66),...
     'fs) in steps of ',num2str(stepmid),' um (',...
     num2str(stepmid*6.66),' fs) to '];
disp(tmpstr);
tmpstr = [num2str(aftorig),' um (',num2str((aftorig)*6.66),...
     'fs) in steps of ',num2str(steplong),' um (',...
      num2str(steplong*6.66),' fs).'];
disp(tmpstr);
tmpstr = ['total number of steps: ',num2str(length(strang))];
disp(tmpstr);
disp('');


% Query user for output file name, number of scans

prefs=''; % prefixes
direcn=''; % directions (forwards or backwards)
nscan=input('enter number of scans ');
disp('')
disp('')
for count = 1:nscan
  disp(['scan number ',num2str(count)]);
  prefs(count,:)=...
    input('Enter 5-letter scan name prefix (ex: ap27g) ','s');
  direcn(count)=input('(f) forwards or (b) backwards? ','s');
  disp('');
  disp('');
end
disp(['enter comment line']);
comment=input('? ','s');


% Information about scan is stored in mmddx000.mat

eval(['save ',prefs(1,:),'000 comment strang ststart',...
     ' prefs b4orig aftorig nscan direcn',...
     ' stepshort stepmid steplong stshort',...
```

```
     ' stmid stlong strangfwd time']);
dummy=input('press return to start ');


% Main Loop

strangf=strang(length(strang):-1:1);
strangb=strang;
for j = 1:nscan
  tmpstr=num2str(length(strang));
  if (length(tmpstr) == 2),
        tmpstr = ['0',tmpstr];
  end
  if (length(tmpstr) == 1),
        tmpstr = ['00',tmpstr];
  end
  disp('');
  pref=prefs(j,:);

  if debug,
    disp(['Scans will be saved in files ',...
        pref,'001.mat through ',pref,tmpstr,'.mat']);
    disp('');
    disp('Moving stage to origin of time delay scan');
  end

  % I assume that when the program is started, the stage is
  % near "t0", when the pump and probe pulses are overlapped.
  % We need a baseline measurement before t0.  The amount of
  % baseline before t0 is specified by "ststart".

  eval(['!\dyna\stage - ',num2str(ststart)]);

  if debug,
    disp('Setting stage software origin');
  end

  % set stage software origin to current position
  !\dyna\stage o 0

  if debug,
    if direcn(j)=='f',
```

```
    disp('scanning in forwards mode');
  else
    disp('scanning in backwards mode');
  end
end

% loop over stage positions <strang>
for count = 1:length(strang),

  % set stage position, (depends on scan direction)
  if direcn(j)=='f',
    % if it is a "forward" scan, move stage to "strangf"
    eval(['!\dyna\stage a ',num2str(strangf(count))]);
  else
    % else it is a backward scan, move stage to "strangb"
    eval(['!\dyna\stage a ',num2str(strangb(count))]);
  end

  % acquire spectrum
  eval(['!\mcbacq\mcbacq'+num2str(acqtime)]);

  % set tmpstr to the stage position index
  if direcn(j)=='f',
    tmpstr=num2str(count);
  else
    tmpstr=num2str(length(strang)-count+1);
  end

  % pad stage position index with leading zeroes
  if (length(tmpstr) == 2),
    tmpstr = ['0',tmpstr];
  end
  if (length(tmpstr) == 1),
    tmpstr = ['00',tmpstr];
  end

  % store spectrum
  eval(['!\dyna\mcbmat ',pref,tmpstr]);

end  %end stage loop

if debug,
```

```
    disp('');
    disp('Setting stage back to zero');
  end

  % move stage back to software origin
  !\dyna\stage a 0
  eval(['!\dyna\stage + ',num2str(ststart)]);
  disp(['finished acquiring prefix ',pref])
end % end scan loop

disp('finished with set of scans');
% end script
```

Appendix B

Software for Multiple Reflection Theory

```
% SCHROD.M

% A Program for finding image state wavefunctions and binding
% energies using the approximations of Multiple Reflection Theory.

% Multiple Reflection Theory uses confluent hypergeometric functions
% to describe the wavefunctions of the image potential.  However, it
% is numerically more convenient to use Runge-Kutta to solve the
% Schrodinger equation, rewritten as a pair of coupled ordinary
% differential equations:


%       y1'=y2
%       y2'=2m(e-v)y1


% This is a two-point boundary value problem.  The wavefunction must
% match the metal at z=0, and must "vanish" at "infinity".  This code
% looks for energies where the wavefunction is small at large z (say,
% 120A).  Strictly speaking, the exact point along the z axis where
% the wavefunction is evaluated should have an influence on the
% calculated binding energy.  The program makes no guarantees and it
% is up to the user to verify that the "zfinal" parameter is
```

```
% sufficiently large so as to have a negligible impact on the
% resulting wavefunctions and binding energies.

% Relies on INITVS.M for initialization of the substrate band
% parameters.

% Relies on PSIS.M for the NFE wavefunction of the substrate.

% the ydot function name (containing the differential equations) is
% HAMILAG.M

% the following are used by the hamiltonian (ydot file)
% and so must be declared global (ODE doesn't pass parameters).

global ee xcutau hartree

% atomic units conversion
hartree = 27.2114; % eV
bohr = .529177; % Angstroms

disp('SCHROD.M:')
disp('Clean Ag(111) Binding Energy and wavefunctions')

outs=input('enter the output filename ','s');
xcutoff=input('enter the xcutoff parameter ');
t0=0; % the point from which we are integrating
zfinal=input('enter zfinal parameter ');
% zfinal should be at least twice the classical turning point

global kpar
kpar=input('enter k parallel in A^-1 ');
tfinal=zfinal/bohr;
xcutau=xcutoff/bohr;

% Precision of calculated binding energies, in meV.  Must be small
% to ensure accurate wavefunctions.  Calculated wavefunctions are
% very sensitive to the precision of the binding energies.
EPRECISION = 1e-6;

initvs  % initialize the substrate band parameters

counter=0;
```

```
yfinal=0;
ypfinal=0;


% for clean Ag, an example range is [-1:.1:-.5 -.45:.05:.1]

range=input('enter range ');

% Now some setup options for the Matlab 5 ODE solver.
% See ODE45 and ODESET documentation for details

options=odeset('AbsTol',1e-10,'RelTol',1e-8,'MaxStep',.5);

% The above options are reasonable guesses that seem to work well for
% the clean surface.  If necessary, you should change them to see if
% you can increase speed affecting accuracy.  Check to make sure
% integrator takes several steps in any region where is a change in
% the slope of the potential.

tic; % start timer

disp('Finding approximate eigenenergies...');

% first loop through a range to find approx eigenenergies

for bind=range,
  counter=counter+1;
  ee=bind/hartree;
  % initial wavefunction value and initial wavefunction slope are
  % the initial y values supplied to  ydot file.  The slope must be
  % multiplied by <bohr>.
  [xpsix, xpsipx] = psis(bind,0);
  y0=[xpsix xpsipx*bohr]';


  % set the slope and value to NFE values at origin, integrate the
  % 1-D Schrodinger Equation.
  [t,y] = ode45('hamilag',[t0 tfinal],y0,options);
  yfinal(counter)=y(length(y),1);
end

% look for a sign change
```

```
bounds=[];
ptr2=0;
ptr=1;

% Find the number of eigensolutions by counting the
% number of times the wavefunction solution (as a
% function of energy) crosses zero (the sign changes)
% at large z.  Record the energy region in which
% the solution is thought to reside in the <bounds>
% variable.

osgn=sign(yfinal(1));
while ptr < length(range)
  ptr=ptr+1;
  if sign(yfinal(ptr)) ~= osgn,
    ptr2=ptr2+1;
    bounds(ptr2,:)=[range(ptr-1),range(ptr)];
  end
  osgn=sign(yfinal(ptr));
end

disp(['Number of eigenvalues is ' int2str(ptr2)])
eeig=0;
sstr='';
disp('Refining eigenenergies...')

% perform a binary search for each eigenenergy
for eign=1:ptr2,
  range=bounds(eign,:); % binary search is slow, but always works
  elower=min(range);    % (provided there is only one root in range)
  eupper=max(range);

  % starting values for the binary search
  bind=elower;  % find yfinal at lower bound
  ee=bind/hartree;
  [xpsix xpsipx] = psis(bind,0);  % initial wavefunction value
                                  % and initial slope
  y0=[xpsix, xpsipx*bohr]';       % are the initial y values
                                  % supplied to ydot file

  % integrate the 1-D Schrodinger Equation.
  [t,y] = ode45('hamilag',[t0 tfinal],y0,options);
```

```
yflower=y(length(y),1); % yfinal at lower bound
bind=eupper;  % find yfinal at upper bound
ee=bind/hartree;
[xpsix, xpsipx] = psis(bind,0); % initial wavefunction value
                                % and initial slope
y0=[xpsix, xpsipx*bohr]';       % are the initial y values
                                % supplied to  ydot file

% integrate the 1-D Schrodinger Equation.
[t,y] = ode45('hamilag',[t0 tfinal],y0,options);
yfupper=y(length(y),1); % yfinal at upper bound
if sign(yfupper) ==sign(yflower),
   disp('No sign change over interval, search not possible')
   disp('Perhaps the <range> variable is improperly defined')
   error('CALCULATION HALTED')
   stop  % This shouldn't happen.
end

% iterate until EPRECISION is reached.
while abs(eupper-elower) > EPRECISION,
  bind=(elower+eupper)/2; % find yfinal in the middle
  ee=bind/hartree;
  [xpsix, xpsipx] = psis(bind,0); % initial wavefunction value
                                  % and initial slope
  y0=[xpsix, xpsipx*bohr]';       % are the initial y values
                                  % supplied to  ydot file

  % set the slope and value to NFE values at origin
  [t,y] = ode45('hamilag',[t0 tfinal],y0,options);
  yfmid=y(length(y),1); % yfinal in the middle
  if sign(yfmid) ~= sign(yflower),
    eupper=bind;   % if there is a sign change between lower
    yfupper=yfmid; % bound and middle, then the new upper bound is
                   % the middle
  else
    elower=bind;
    yflower=yfmid; % new lower bound is the middle
  end
end
eval(['y',int2str(eign),'=y(:,1);']); % y(:,1) is the wavefunction
                                      % y(:,2) is the slope
eval(['x',int2str(eign),'=t;']);
```

```
  sstr=[sstr,' y',int2str(eign),' x',int2str(eign)];
  eeig(eign)=elower;
end

xpot=t0:.1:40;
ypot=xpot;

for ctr=1:length(xpot),
 [blah,ypot(ctr)]=hamilag(xpot(ctr),[1 1]);
end  % the potential is in xpot,ypot, units are bohr, hartree

% Zero out the divergent part and normalize wavefunction

cut=zfinal-1;
ctr=0;
xl=-101:.1:-.1;
yl=xl;
if length(eeig) > 2,
  nn=3;
else
  nn=length(eeig);
end

yall=[];

for bind = eeig(1:nn),
  ctr = ctr + 1;

  for ctr2=1:length(xl), % inefficient for loop
    yl(ctr2) = psis( bind, xl(ctr2) ); % substrate part of
                                       % wavefunction
  end

  eval(['xm=[xl x',int2str(ctr),'(:)''*bohr];']);
  eval(['ym=[yl y',int2str(ctr),'(:)''];']);
  xall=-100:.1:cut;
  ya=interp1(xm,ym,xall,'cubic');

  % The numerical wavefunction solution always starts increasing
  % exponentially at some large value of <z>.  The following section
  % attempts to truncate the divergent part. This doesn't always
  % work.  This approach assumes the divergent part is exponential.
```

```
  % Using the slope of log(psi=ya) at large <z>, we can extrapolate
  % linearly to where <ya> last crosses zero.

  dy=log(abs(ya(length(ya))))-log(abs(ya(length(ya)-10)));
  dx=xall(length(ya))-xall(length(ya)-10);
  expslope=dy/dx;
  expintercept=log(abs(ya(length(ya))))-expslope*xall(length(ya));
  % first guess zero when y=exp(-5), this works well
  % for clean Ag(111)
  guesszero=(-5-expintercept)/expslope;
  zidx=min(find(xall>guesszero)); % index corresponding to ya ~= 0.
  % try to find minimum within 200 points of guess
  [minval,dzero]=min(abs(ya((zidx-200):(zidx+200))));
  zidx=zidx+dzero-200;
  idx=zidx:length(xall); % return array of indices corresponding
                         % to x > guesszero
  ya(idx)=zeros(size(idx)); % zero out indices where ya starts to
                            % diverge exponentially
  % normalize
  yarea = sqrt( sum(ya.^2 * ( xall(2) - xall(1) ) ) );
  ya=ya/yarea;
  yall(ctr,:)=ya(:)';
end
toc %display time required to calculate

% wavefunctions are in xall, yall.  Length unit is Angstroms.
% Eigenenergies are in <eeig>.  Always examine the wavefunctions
% as a sanity check to make sure the binding energies are
% meaningful.

% xpot, ypot is the potential in hartree and bohr radii.

% save to the initially specified MAT file.
eval(['save ', outs, ' range xcutoff zfinal bohr hartree'...
      ,' eeig xpot ypot xall yall cfe hbar']);

% end SCHROD.M



% INITV.M
```

```
% This script initializes many constants used to
% find solutions to the problem of a Coulomb
% potential on a NFE metal (2-band).

% First, some fundamental constants

global ryd me qe cfe hbar kpar

ryd=13.6056981; % Rydberg, in eV

hbar=1.0546e-34; % J * S

me=9.1096e-31; %Kg, mass electron

qe=1.602e-19; %Coulombs, fundamental charge

cfe=sqrt(hbar^2/(2*qe*me)*1e20); %energy-wavevector relation,
                                 %eV & Angstroms

% Now NFE metal parameters

% This is for Ag(111)
global cs egs vgs as wfns efermis ps emaxqs

global MU ML kpar
MU=1.6; %effective mass of the upper band edge

ML=.6;  %effective mass of the lower band edge


as=2.36; %lattice spacing,
         %we will assume is independent of k parallel
ps=pi/as; %wavevector p, valid only in gap,
          %will assume is independent of kpar

Mave=(MU+ML)/2; %average effective mass for CB and VB, use
                %to calculate Eg

egs=9.64+cfe^2*kpar^2/Mave; %energy at g/2, NOT independent of kpar

Dwidth=cfe^2*kpar^2/MU-cfe^2*kpar^2/ML; %change in gap full width
```

```
% most calcs were done using 2.075
vgs=2.075+Dwidth/2; %gap half-width, NOT independent of kpar

cs=sqrt(egs)/ps; %Along gamma-L, E-k relation

%helps in determining the proper branch of q
emaxqs=(4*egs^2-vgs^2)/(4*egs);

%work function, subtract .45 for Xe/Ag(111), independent of kpar
wfns= 4.56;

efermis=7.865; %fermi level wrt gamma, independent of kpar


function [tpsi, tpsip]=psis(e,z)

  % This function returns the crystal wavefunction,
  % for half-layer termination

  global ps cs as

  % wavefunction

  tpsi = exp( -qs(e) * ( z + as/2 ) ) * cos( ps * ...
      ( z + as/2 ) + deltas(e));

  % wavefunction slope

  tpsip= -qs(e) * exp( -qs(e) * ( z + as/2 ) ) * ...
      cos( ps * ( z + as/2 ) + deltas(e) ) - ...
      ps * exp( -qs(e) * ( z+as/2 ) ) * ...
      sin( ps * ( z + as/2 ) + deltas(e) );

function en=enets(e1)

  % ENETS -- substrate
  % finds the net energy wrt the gamma point of the substrate
  % uses efermi wfns

  global efermis wfns
  en=e1+efermis+wfns;
```

```
function d=deltas(e1)
  %
  %DELTA-  finds delta given eg vg emaxq p c
  %
  global egs vgs emaxqs ps cs

  % if-then else to pick correct branch of the arctangent

  if enets(e1) > (egs+vgs) % above upper band edge
    d=0;
  else
    if enets(e1) < (egs - vgs) % below lower band edge
      d=-pi/2;
    else
      if enets(e1) > emaxqs % upper half of band
        d=real(asin(2*qs(e1)*cs^2*ps/vgs)/2);
      else % lower half of band
        d=real(-pi/2-asin(2*qs(e1)*cs^2*ps/vgs)/2);
      end
    end
  end

function q=qs(e1)

  % function QS.M
  % calculates the imaginary part of the electron wavevector
  % in the gap

  global egs vgs cs

  % if in the gap, compute <q>, else q=0
  if (enets(e1) > (egs-vgs)) & (enets(e1) < (egs+vgs)),
    q = sqrt( sqrt( 4 * enets(e1) * egs + vgs^2) - ...
        enets(e1) - egs) / (-cs);
  else
    q=0;
  end

function [yp,v] = hamilag(x,y)

  % function HAMILAG.M
```

```
% Time-independent Schrodinger equation for an Image potential,
% written as a pair of coupled ordinary differential equations.

global ee xcutau kpar cfe hartree
if x < xcutau,
  v= -1/4/xcutau + cfe^2 * kpar^2 / hartree;
  %the kpar part takes into account parallel energy
  ke= -2*(ee-v);
else
  v=-1/4/x+cfe^2*kpar^2/hartree;
  %the kpar part takes into account parallel energy
  ke= -2*(ee-v);
end
yp=[y(2), ke*y(1)]';
```